

# Towards non-volatility in quantum-dot-based memories

vorgelegt von

M. Sc. Physik

**Leo Bonato**

aus Pordenone (Italien)

von der Fakultät II - Mathematik und Naturwissenschaften  
der Technischen Universität Berlin  
zur Erlangung des akademischen Grades  
Doktor der Naturwissenschaften  
Dr. rer. nat.

genehmigte Dissertation

Promotionsausschuss:

Vorsitzende: Prof. Dr. rer. nat. Sabine Klapp

Berichter/Gutachter: Prof. Dr. rer. nat. Dieter Bimberg

Berichter/Gutachter: Prof. Dr.-Ing. Thomas Mikolajick

Tag der wissenschaftlichen Aussprache: 30. Juni 2017

Berlin 2017



# Abstract

The aim of this work is the extension of the hole storage time at room temperature in self-organised semiconductor quantum dots (QDs), with the long-term goal of achieving non-volatility in said QDs in order to develop a novel charge-storage memory architecture. Static capacitance spectroscopy (C–V profiling) and time-resolved capacitance spectroscopy (deep level transient spectroscopy, DLTS) are used to determine the localisation energy and the apparent capture cross-section for holes. The two quantities are in turn used to extrapolate the hole storage time at room temperature.

Two systems were characterised for the first time in this work:  $\text{In}_{0.5}\text{Ga}_{0.5}\text{As}$  QDs on a GaAs interlayer embedded in GaP with an additional AlP barrier, and GaSb QDs embedded in GaP.

The localisation energy measured for the  $\text{In}_{0.5}\text{Ga}_{0.5}\text{As}/\text{GaAs}/\text{AlP}/\text{GaP}$  QDs system is  $E_{\text{loc}} = 1.15(\pm 0.03)$  eV, with an associated capture cross-section  $\sigma_{\infty} = 8 \times 10^{-10}$  cm<sup>2</sup> (with an uncertainty of 0.4 orders of magnitude). The height of the AlP barrier is estimated as  $0.52(\pm 0.01)$  eV, which results in a localisation energy of  $0.63(\pm 0.03)$  eV for the sole QDs without barrier. An extrapolated hole storage time at room temperature for the “QDs + barrier” system of 260 s (with an uncertainty of 0.1 orders of magnitude) was achieved, representing an improvement of 2 orders of magnitude compared to previous studies.

For the GaSb/GaP QDs system, several samples were grown under different conditions in order to investigate their effect on the localisation energy and the capture cross-section. The sample grown under optimal conditions demonstrated a localisation energy  $E_{\text{loc}} = 1.18(\pm 0.09)$  eV and an apparent capture cross-section  $\sigma_{\infty} = 1 \times 10^{-12}$  cm<sup>2</sup> (with an uncertainty of 0.1 orders of magnitude). The corresponding hole storage time at room temperature is 3.9 days (with an uncertainty of 0.04 orders of magnitude), marking an improvement of further 3 orders of magnitude and an absolute record for hole storage time at room temperature in self-organised quantum dots. Measurements on the other samples indicate that the capture cross-section can indeed be manipulated by adjusting the growth parameters. A precise protocol for capture cross-section engineering could however not be developed within the scope of this thesis.

Based on the results of this work, recommendations are given for further extending the hole storage time at room temperature in self-organised quantum dots. Firstly, non-volatility can be achieved in the GaSb/GaP QDs system either by increasing the Sb content in the QDs or by adding an AlP barrier below the QD layer. Secondly, other novel heterostructures with very large projected localisation energies are proposed: GaSb/ $\text{Al}_{0.51}\text{In}_{0.49}\text{P}$  QDs ( $E_{\text{loc}} = 1.25$  eV), which presents the additional advantage of being lattice-matched to GaAs, and InGaSb/GaP QDs ( $E_{\text{loc}} = 1.5$  eV). Thirdly, the storage time can be increased by reducing the capture cross-section. The latter suggestion requires the development of a reliable technique for cross-section engineering.



# Zusammenfassung

Ziel dieser Arbeit ist die Verlängerung der Lochspeicherzeit selbstorganisierter Halbleiter-Quantenpunkte (QPe) bei Raumtemperatur. Das angestrebte langfristige Endziel ist die Erreichung der Nichtflüchtigkeit in den oben genannten QPen, um eine darauf basierte Speicherarchitektur zu entwickeln. Statische Kapazitätsspektroskopie (C–V-Charakterisierung) und zeitaufgelöste Kapazitätsspektroskopie (deep level transient spectroscopy, DLTS) wurden zur Bestimmung der Loch-Lokalisierungsenergie und -Einfangquerschnittes angewendet. Aus jenen Größen wird die Lochspeicherzeit bei Raumtemperatur extrapoliert.

Zwei neuartige Materialsysteme wurden zum ersten Mal in dieser Arbeit charakterisiert. Das erste Materialsystem besteht aus in GaP eingebetteten  $\text{In}_{0.5}\text{Ga}_{0.5}\text{As}$ -QPen, die auf einer GaAs-Zwischenschicht gewachsen wurden. Eine zusätzliche ALP-Barriere dient zur Verlängerung der Speicherzeit. Das zweite Materialsystem besteht aus in GaP eingebetteten GaSb-QPen.

Die gemessene Lokalisierungsenergie der  $\text{In}_{0.5}\text{Ga}_{0.5}\text{As}/\text{GaAs}/\text{ALP}/\text{GaP}$ -QPe-Materialsystem ist  $E_{\text{lok}} = 1.15(\pm 0.03)$  eV, mit Einfangquerschnitt  $\sigma_{\infty} = 8 \times 10^{-10}$  cm<sup>2</sup> (Messabweichung: 0.4 Größenordnungen). Die Höhe der ALP-Barriere beträgt  $0.52(\pm 0.01)$  eV, was eine Lokalisierungsenergie  $0.63(\pm 0.03)$  eV für die alleinigen QPe (ohne Barriere) entspricht. Die extrapolierte Speicherzeit bei Raumtemperatur des "QPe + Barriere"-Systems kommt auf 260 s (Messabweichung: 0.1 Größenordnungen). Die erzielte Speicherzeit stellt ein Fortschritt von 2 Größenordnungen im Vergleich mit vorigen Ergebnissen dar.

Für das GaSb/GaP-QPe-System wurden unter unterschiedlichen Bedingungen verschiedenen Proben gewachsen, um den Effekt der Wachstumsbedingungen auf die Lokalisierungsenergie und den Einfangquerschnitt festzustellen. Die maximale erreichte Lokalisierungsenergie ist  $E_{\text{lok}} = 1.18(\pm 0.09)$  eV, mit Einfangquerschnitt  $\sigma_{\infty} = 1 \times 10^{-12}$  cm<sup>2</sup> (Messabweichung: 0.1 Größenordnungen). Die entsprechende Speicherzeit beträgt 3.9 Tage (Messabweichung: 0.04 Größenordnungen). Dies macht einen weiteren Fortschritt von 3 Größenordnungen aus und stellt einen absoluten Rekordwert für die Lochspeicherzeit bei Raumtemperatur in selbstorganisierten QPen dar. Die auf den anderen Proben ausgeführten Messungen bestätigen, dass der Einfangquerschnitt über die Wachstumsbedingungen manipuliert werden kann. Die Entwicklung eines vollständigen Verfahrens zur Steuerung des Einfangquerschnittes liegt aber außerhalb des Umfangs dieser Dissertation.

Basierend auf den Ergebnissen dieser Arbeit werden Vorschläge für die weitere Verlängerung der Speicherzeit gemacht. Erstens, Nichtflüchtigkeit lässt sich in GaSb/GaP-QPen durch Erhöhung des Sb-Inhaltes oder durch Einsatz einer ALP-Barriere erreichen. Zweitens, weitere neuartige Heterostrukturen mit sehr hoher simulierter Lokalisierungsenergie werden vorgeschlagen: GaSb/ $\text{Al}_{0.51}\text{In}_{0.49}\text{P}$ -QPe ( $E_{\text{lok}} = 1.25$  eV), die gitterangepasst auf GaAs gewachsen werden können, und InGaSb/GaP-QPe ( $E_{\text{lok}} = 1.5$  eV). Drittens, die Speicherzeit lässt sich durch Verringerung des Einfangquerschnittes verlängern. Zu diesem Ziel muss jedoch zuerst ein zuverlässiges Verfahren zur Steuerung des Einfangquerschnittes entwickelt werden.



# Publications

Parts of this work have been published in:

- G. Stracke, A. Glacki, T. Nowozin, L. Bonato, S. Rodt, C. Prohl, A. Lenz, H. Eisele, A. Schliwa, A. Strittmatter, U. W. Pohl, and D. Bimberg  
“Growth of  $\text{In}_{0.25}\text{Ga}_{0.75}\text{As}$  quantum dots on GaP utilizing a GaAs interlayer”  
*Applied Physics Letters* 101 (2012), p. 223110.
- L. Bonato, E. M. Sala, G. Stracke, T. Nowozin, A. Strittmatter, M. N. Ajour, K. Daqrouq, and D. Bimberg  
“230 s room-temperature storage time and 1.14 eV hole localization energy in  $\text{In}_{0.5}\text{Ga}_{0.5}\text{As}$  quantum dots on a GaAs interlayer in GaP with an AlP barrier”  
*Applied Physics Letters* 106.4 (2015), p. 042102.
- L. Bonato, I. F. Arikian, L. Desplanque, C. Coinon, X. Wallart, Y. Wang, P. Ruterana, and D. Bimberg  
“Hole localization energy of 1.18 eV in GaSb quantum dots embedded in GaP”  
*physica status solidi (b)* 10 (2016), pp. 1877–1881.
- L. Desplanque, C. Coinon, D. Troadec, P. Ruterana, G. Patriarche, L. Bonato, D. Bimberg and X. Wallart  
“Morphology and valence band offset of GaSb quantum dots grown on GaP(001) and their evolution upon capping”  
*Nanotechnology* 28.22 (2017), p. 225601.



*To my siblings —*



# Contents

<b>Abstract</b>	<b>i</b>
<b>Zusammenfassung</b>	<b>iii</b>
<b>Publications</b>	<b>v</b>
<b>Introduction</b>	<b>xiii</b>
<b>1. Solid-State Memories</b>	<b>1</b>
1.1. Charge-storage memories . . . . .	1
1.2. DRAM . . . . .	4
1.3. Flash . . . . .	5
1.4. Alternative memory architectures . . . . .	7
1.4.1. FeRAM . . . . .	7
1.4.2. MRAM . . . . .	8
1.4.3. PCRAM . . . . .	8
1.4.4. Resistive switching memories . . . . .	8
1.5. Motivation of this work . . . . .	9
<b>2. Heterostructures and Nanostructures</b>	<b>13</b>
2.1. Semiconductor heterostructures . . . . .	13
2.1.1. III–V semiconductors . . . . .	14
2.1.2. Band alignment . . . . .	15
2.2. Nanostructures . . . . .	16
2.3. Two-dimensional carrier gases . . . . .	17
2.3.1. Modulation-doped field-effect transistor . . . . .	19
2.4. Self-organised quantum dots . . . . .	20
2.4.1. Fabrication . . . . .	21
2.4.2. Modelling and electronic structure . . . . .	23
2.4.3. Ensemble broadening . . . . .	26

<b>3. Charge-carrier dynamics in quantum dots</b>	<b>29</b>
3.1. Emission processes . . . . .	29
3.2. Rate equation . . . . .	31
3.3. Capture processes . . . . .	32
3.3.1. Many-particle effects . . . . .	33
3.3.2. Poole-Frenkel effect . . . . .	34
3.4. Emission rates . . . . .	35
3.4.1. Thermal emission rate . . . . .	35
3.4.2. Tunnel emission rate . . . . .	36
3.4.3. Thermally-assisted tunnelling rate . . . . .	37
3.4.4. Total emission rate . . . . .	38
<b>4. QD-Flash</b>	<b>41</b>
4.1. Storage . . . . .	43
4.2. Write operation . . . . .	44
4.3. Erase operation . . . . .	45
4.4. Read-out . . . . .	46
<b>5. Experimental Techniques</b>	<b>49</b>
5.1. The p–n junction . . . . .	49
5.1.1. Depletion layer . . . . .	49
5.1.2. Capacitance of a p–n junction . . . . .	51
5.2. Static capacitance spectroscopy . . . . .	52
5.2.1. Effect of quantum dots . . . . .	53
5.3. Time-resolved capacitance spectroscopy . . . . .	57
5.3.1. The DLTS sample . . . . .	57
5.3.2. Measurement protocol . . . . .	58
5.3.3. Rate window and double-boxcar method . . . . .	60
5.3.4. Charge selective DLTS . . . . .	62
<b>6. InGaAs QDs in GaP</b>	<b>65</b>
6.1. $\text{In}_{0.25}\text{Ga}_{0.75}\text{As}$ QDs in GaP . . . . .	65
6.2. Growth of $\text{In}_{0.5}\text{Ga}_{0.5}\text{As}$ QDs in GaP . . . . .	68
6.3. C–V characterisation . . . . .	70
6.4. Conventional DLTS . . . . .	71
6.5. Charge-selective DLTS . . . . .	73
6.6. Storage time at room temperature . . . . .	76

<b>7. GaSb QDs in GaP</b>	<b>79</b>
7.1. Growth of GaSb QDs in GaP . . . . .	79
7.2. C–V characterisation . . . . .	82
7.3. Conventional DLTS . . . . .	83
7.4. Charge-selective DLTS . . . . .	84
7.4.1. Sample 2-Ref . . . . .	85
7.4.2. Sample 2-QD-A . . . . .	85
7.4.3. Sample 2-QD-B . . . . .	86
7.4.4. Sample 2-QD-C . . . . .	87
7.4.5. Sample 2-QD-D . . . . .	89
7.4.6. Sample 2-QD-AIP . . . . .	90
7.5. Discussion . . . . .	91
<b>8. Conclusions and Outlook</b>	<b>97</b>
<b>A. Error analysis of DLTS measurements</b>	<b>103</b>
A.1. $\text{In}_{0.5}\text{Ga}_{0.5}\text{As}/\text{AIP}/\text{GaAs}/\text{GaSb}$ QDs . . . . .	103
A.1.1. Sample 1-QD: Charge-selective DLTS — Ground state . . . . .	103
A.1.2. Sample 1-QD: Charge-selective DLTS — Shallowest state . . . . .	106
A.1.3. Sample 1-QD: Conventional DLTS . . . . .	107
A.1.4. Sample 1-Barr: Charge-selective DLTS . . . . .	107
A.2. GaSb/GaP QDs . . . . .	109
A.2.1. Sample 2-Ref . . . . .	109
A.2.2. Sample 2-QD-A . . . . .	109
A.2.3. Sample 2-QD-B . . . . .	110
A.2.4. Sample 2-QD-C . . . . .	111
A.2.5. Sample 2-QD-D . . . . .	112
A.2.6. Sample 2-QD-AIP . . . . .	114
<b>B. Samples</b>	<b>117</b>
B.1. $\text{In}_{0.5}\text{Ga}_{0.5}\text{As}/\text{GaAs}/\text{AIP}/\text{GaP}$ QDs . . . . .	117
B.2. GaSb/GaP QDs . . . . .	117
<b>C. Experimental details</b>	<b>119</b>
C.1. C–V profiling setup . . . . .	119
C.2. DLTS setup . . . . .	119

*Contents*

C.3. Processing . . . . .	120
C.3.1. Lithography and metallisation of the Ohmic top contact . . . . .	121
C.3.2. Lithography and dry-etching of mesas . . . . .	122
C.3.3. Lithography and metallisation of the Ohmic back contact . . . . .	125
<b>Bibliography</b>	<b>127</b>
<b>Acknowledgements</b>	<b>143</b>

# Introduction

La vida no es la que uno vivió, sino la que uno recuerda, y cómo la recuerda para contarla.

---

*(Gabriel García Márquez)*

The fast-paced development that characterises present-day information technology imposes increasingly high demands on the underlying technological and electronic infrastructure. One of the most challenging aspects of this growth concerns the amount of data constantly being retrieved, processed, transmitted, and stored all around the globe: The total estimated size of the “digital universe” lay below 1 exabyte<sup>1</sup> [1] in 2005, passed the zettabyte<sup>2</sup> mark in 2010, and is expected to reach 35 zettabytes by 2020 [2].

Up until now the exponentially growing storage needs have been met thanks to the evolution of storage technology according to *Moore’s law*: “The number of components per unit area on a chip doubles about every 12 months”<sup>3</sup> [3]. This empirical law is based on constantly decreasing the size of the devices and resultantly increasing the number of devices per unit area. The miniaturisation approach, however, presents two major limitations.

On the one hand, industry-standard miniaturisation techniques entail exponentially increasing fabrication costs because they are based on the *top-down approach*: Fabrication proceeds from the wafer level, using lithography and etching to define the desired features, down to the nanometre scale. The increasing degree of accuracy required by the process steadily pushes the costs up.

On the other hand, miniaturisation cannot progress indefinitely because eventually quantum effects become so important that they compromise the functionality of the device. In particular, for sufficiently small feature sizes the statistical fluctuations of the interface roughness will lead to uncontrollable tunnelling leakage. In fact, the Interna-

---

<sup>1</sup>1 exabyte =  $10^{18}$  bytes = 1 million terabytes.

<sup>2</sup>1 zettabyte =  $10^{21}$  bytes = 1 billion terabytes.

<sup>3</sup>Later corrected to 18 to 24 months.

tional Technology Roadmap for Semiconductors 2.0 predicts that downscaling will only be feasible until 2021, after which the feature size will not decrease below 10 nm [4].

In order to overcome the limitations of downscaling, the ITRS calls for implementing new functionalities onto devices of the same size [5]. For instance, one of the shortcomings of today's solid-state storage technology is the divide between volatile and non-volatile memory. Volatile memory is characterised by its high speed, but it is unable to retain data for longer periods of time without external energy supply. It is therefore used as working memory, storing the comparatively small amounts of data needed for processing. The most common example of solid-state volatile memory is DRAM [6]. Non-volatile memory, on the other hand, provides long storage time, but data access is slow. It is therefore used as mass storage. The most common example of solid-state non-volatile memory is Flash. Current memory architectures present in other words a *trade-off* between storage time and data access speed. Solving this trade-off would "initiate a revolution in computer architecture" [5].

Self-organised quantum dots [7] are promising candidates for the development of a storage architecture able to solve the trade-off. The term "self-organised" refers to the fact that their formation occurs spontaneously during epitaxial growth, a prime example of the so-called "bottom-up" approach. Densities of up to  $1 \times 10^{11} \text{ cm}^{-2}$  (i.e. up to 1 Tbit/inch<sup>2</sup>, assuming that each quantum dot stores 1 bit of information) can be achieved without lithographic patterning. Charge carriers are captured thermally into quantum dots, determining write times of a few picoseconds [8, 9]. Meanwhile, the electronic structure of the quantum dots allows them to localise charge carriers for extended periods of time without the need for an additional barrier, which would slow down the erase operation.

QD-Flash [10–12] is a novel memory architecture, based on III–V self-organised quantum dots embedded in a modulation-doped field-effect transistor (MODFET). QD-Flash relies on self-organised quantum dots as the storage element, while the channel of the MODFET serves as read-out for the occupation of the quantum dots. The feasibility of QD-Flash has been proven by manufacturing a fully-functional<sup>4</sup> demonstrator [12, 13]. Moreover, self-organised quantum dots demonstrated storage times at room temperature up to 1.6 s [14], with write and read times in the range of those of DRAM (6 ns [15] and 3 ns [16], respectively). Two issues remain to address in QD-Flash: the extension of the storage time above the non-volatility limit (10 years) and the shortening of the erase time below that of DRAM ( $\sim 10$  ns).

This work sets off to increase the storage time at room temperature of quantum-dot-

---

<sup>4</sup>At low temperatures (< 200 K).

based memory structures by means of material and band-structure engineering. The structure of the work is summarised below.

- **Chapter 1** describes the fundamental concepts of storage technology and the working principles of state-of-the-art memory architectures, with special emphasis on DRAM and Flash. This provides the framework for the rest of the dissertation.
- **Chapters 2 and 3** represent the theoretical background for this work. While the former focuses on growth and properties of semiconductor heterostructures, the latter concentrates on the analytical description of capture and emission processes in quantum dots, leading to the central relation of this thesis: the emission rate as a function of the localisation energy.
- **Chapter 4** describes in detail the structure and working principle of QD-Flash.
- **Chapter 5** contains details on the experimental techniques used in this work: static capacitance spectroscopy (i.e. C–V profiling) and time-resolved capacitance spectroscopy (i.e. DLTS). The chapter is prefaced by a short derivation of the formulas relevant to the capacitance of a p–n junction.
- **Chapter 6 and 7** are the core of this work, detailing the experiments carried out to determine the localisation energy of InGaAs and GaSb quantum dots embedded in GaP and discussing their results.
- **Chapter 8** summarises the results achieved and suggests possible ways of continuing the development of QD-Flash.
- **Appendix A** details the data analysis method adopted in this work.
- **Appendix B** reports the real names of the samples characterised in this work.
- **Appendix C** illustrates the experimental setups used for characterisation and the recipes used for clean-room processing.



# 1. Solid-State Memories

Memory is the thing you forget with.

---

*(Alexander Chase)*

Since the main goal of this work is the improvement of solid-state memory technology, this chapter begins with an introduction to the fundamental principles of data storage in information technology. The introduction is followed by a brief overview of available solid state memory architectures, with emphasis on the most widespread ones: DRAM and Flash. Finally, the motivation of this work is stated explicitly, based on the shortcomings of present-day technology.

## 1.1. Charge-storage memories

Modern information technology is based on the binary system: All information is encoded and represented by a sequence of 0's and 1's [17], each one of which is called a *bit* (binary digit). Naturally, the information is also stored in the form of bits, so any storage device must be able to switch between two different states representing 0 and 1 (for example on/off, open/close, spin up/spin down...). In the specific case of a storage device based on charge carriers ("charge-storage memory"), the two states are normally represented by some kind of potential well being occupied or not occupied by said charge carriers.

The functioning principle of any such device can in general be represented by a diagram similar to the one in Fig. 1.1a: Charge carriers can be stored in a state of metastable equilibrium (represented by the dip on the left-hand side of Fig. 1.1a) and thereby be kept separate from the free charge carriers in the reservoir, placed at a lower energy (right-hand side of Fig. 1.1a). The logic state "1" is realised when charge carriers are present inside the dip, whereas the logic state "0" is represented by the empty dip. The shape of the potential ensures that the logic state is preserved over the desired amount of time because it prevents localised charge carriers from escaping from the dip and free charge carriers from entering the dip. It is therefore the shape of the potential that

## 1. Solid-State Memories

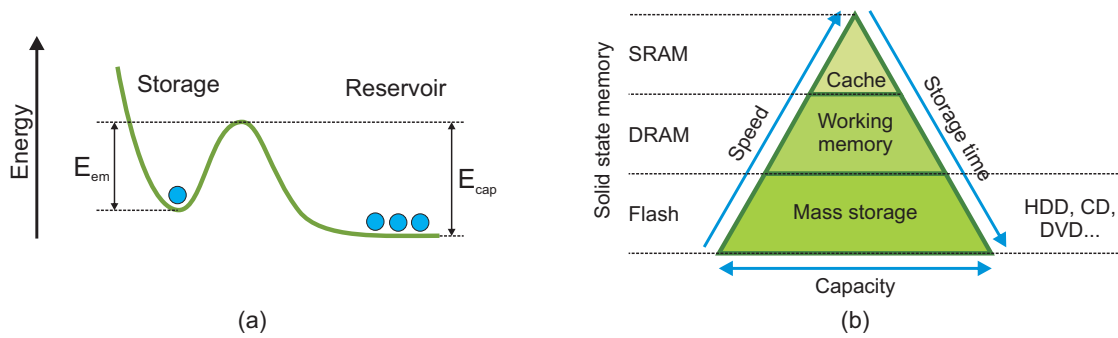


**Figure 1.1.:** (a) Schematic representation of a general potential defining a memory cell based on charge carriers. On the left-hand side, the potential dip forms a metastable state where charge carriers can be stored. The logic state “1” is realised when the dip is occupied by charge carriers, the logic state “0” when it is empty. Charge carriers are localised inside the dip by the emission barrier  $E_{em}$  and free charge carriers are hindered from being captured into the dip by the capture barrier  $E_{cap}$ . (b) Graphical representation of the memory hierarchy: Data access time and storage time decrease towards the top; width represents capacity. Some common memory architectures are reported on either side of the layer to which they belong (left-hand side: solid state memories; right-hand side: magnetic or optical memories).

defines and limits the performance of the device.

More in detail, let us imagine that the logic state “1” is realised by localising one charge carrier inside the dip. The storage time of the “1” is limited by the event of the charge carrier being emitted from the dip, either via tunnelling through the barrier  $E_{em}$  or by thermal emission above it (if additional energy is supplied to the system).  $E_{em}$  is therefore known as *emission barrier*.

Conversely, the storage time of the logic state “0” is limited by the event of free charge carriers being captured from the reservoir into the dip after overcoming the barrier  $E_{cap}$ . The capture can occur if the charge carriers are thermally excited over the barrier, or at least to an energy at which they can tunnel through the barrier.  $E_{cap}$  is known as *capture barrier*.

Taller and thicker barriers lead, in both cases, to longer storage times, which is in principle desirable. Unfortunately, the opposite is true for the write and erase operations: When writing a “1” or writing a “0” (i.e. erasing), the probability of capturing a free charge carrier or emitting a localised charge carrier (respectively) should be as high as possible in order to minimise the duration of the operation. This constitutes the so-called “*trade-off*” problem of solid state memory: Larger storage times also imply longer write and erase times. Two processes can be implemented in order to speed up the writing operation without compromising the storage time: hot-electron injection [18]

and Fowler-Nordheim tunneling [19].

Hot-electron injection consists in providing sufficient kinetic energy for the electrons to overcome the potential barrier. The main drawback of this method is that the injection efficiency remains very low even for electric fields stronger than 100 kV/cm.

Fowler-Nordheim tunnelling uses extremely high electric fields (8–10 MV/cm) to increase the tunnelling probability during the write and erase operations. The main drawback of this method is that the intense electric fields damage the barrier, creating leakage currents through the barrier, which in turn render the memory cell unusable.

Both of these methods do not completely solve the trade-off problem. As a consequence, memory in information technology is organised hierarchically according to its intended application: Faster, more volatile memories are directly connected to the CPU (central processing unit) to be used as cache during computation; slower, non-volatile memories serve as permanent storage when the data is not being actively used. The difference between the typical clock frequency of the CPU and the data access time of mass memory is commonly referred to as the *processor-memory bottleneck*.

Fig. 1.1b represents visually the memory hierarchy. As highlighted by the arrows, memory architectures at the top of the pyramid are very fast but also very volatile, so they are used mostly as CPU cache. The most common example is SRAM (static random-access memory [20]). SRAM uses one flip-flop [21] to store each bit and it is called “static” because the stored information does not need to be refreshed periodically. On the other hand, the data is lost if the cell is not powered. SRAM is hence a volatile memory.<sup>1</sup>

The layer immediately below the CPU level in Fig. 1.1b is the working memory, which contains running programs and data in use. The working memory does not need to be as fast as the CPU cache. Modern computers typically use DRAM (dynamic random access memory [23]) as working memory. DRAM is called “dynamic” because data needs to be refreshed constantly, which makes it a volatile memory.

Finally, the bottom layer of the memory hierarchy is occupied by mass storage, which does not have to be especially fast but must be non-volatile, i.e. able to retain data for longer than 10 years after power supply is interrupted. Nowadays, a wide variety of options is available for mass storage, ranging from magnetic (hard disk drives, floppy disks, tape...), to optical (CDs, DVDs...), to semiconductor-based (solid-state drives, memory cards, USB sticks...). The market for solid-state, non-volatile memory is dominated by Flash memory [24], which is much slower than DRAM but able to retain data for at least

---

<sup>1</sup>SRAM does exhibit data remanence, but the “storage time” is not well-defined and often varies greatly even among different devices from the same batch [22]. Therefore SRAM is not a non-volatile memory in the conventional sense.

## 1. Solid-State Memories

10 years without any external power supply.

The following two sections will shed some light on the working principles of the two memory architectures most relevant to this work: DRAM and Flash.

### 1.2. DRAM

A single DRAM cell consists of one transistor and one capacitor [17]. The transistor acts as a switch used to address the cell, while the charge state of the capacitor represents the stored bit of information. As depicted in Fig. 1.2a, a DRAM cell is placed at the crossing of a word-line and a bit-line. When a word-line is switched to “high”, the transistors of all the cells in that word-line are switched on, connecting the capacitors to their respective bit-lines. The bit-line of the desired cell can now be used to read out the charge state of the capacitor or to charge it, thereby performing the “read” or the “write” operation. If the capacitor is charged before the “read” operation, its charge will flow out through the bit-line during the operation, which is therefore destructive: Data must be rewritten after each reading. DRAM is a *random access* memory because the word-line and bit-line system allows to address any given cell regardless of its physical location on the chip.<sup>2</sup>

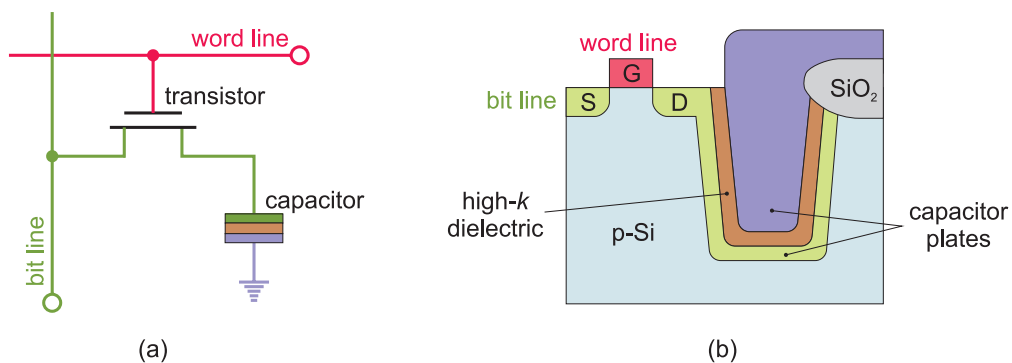


**Figure 1.2.:** Schematic representation of a DRAM cell in its most elementary form, the 1T-1C design (1 transistor, 1 capacitor). (a) Circuit representation of a DRAM cell. The word line (red) controls the transistor, which in turn controls whether the bit line (green) is connected to the capacitor. (b) Cross section of a DRAM cell in the trench geometry (other geometries are possible, but generally less efficient). The left-hand side represents the transistor, where the source, gate and drain have been marked S, G and D, respectively. The right-hand side represents the capacitor. The capacitor is realised as a deep trench in order to maximize the surface area of the plates. (After [17]).

<sup>2</sup>The opposite of a random access memory is a *sequential access* memory, where data must be accessed in the same order in which it has been written. Tape is an example of sequential access memory.

The cross-section of a typical DRAM cell is sketched in Fig. 1.2b. The capacitance of the capacitor cannot be too small, otherwise reading errors might occur because of the smallness of the charge involved. Therefore the capacitors are implemented as deep trenches, so that the lateral dimension of the cell remains small and the density of the memory can be maximised.

The main advantages of DRAM are its *fast data access time* (of the order of tens of nanoseconds) and its *durability* (a DRAM cell can be rewritten over  $10^{16}$  times before becoming unusable).

On the other hand, DRAM has several limitations, first and foremost its volatility. Once power supply is removed, leakage currents through the dielectric release the charge stored in the capacitor, so that DRAM is able to retain data for only 64 ms. Moreover, DRAM is not very energy-efficient for three reasons:

1. Since the storage time is so short, the data stored in a DRAM cell must be rewritten often, a process called "*refresh*". Each refresh cycle consumes energy.
2. Since the read-out operation erases the data, DRAM cells must also be *rewritten after each reading*.
3. DRAM requires over 10000 electrons per bit of stored data [17], thus rendering the aforementioned refresh and rewrite operations relatively *energy-intensive*.

### 1.3. Flash

Flash memory (full name: Flash-EEPROM, electrically erasable and programmable read-only memory [24–26]) is by far the most widespread non-volatile solid state memory [4]. Its success depends on its compactness, speed (compared to hard disk drives), and energy-efficiency. Its invention ushered in a revolution in information technology, enabling previously unthinkable applications like MP3 players, digital cameras, smartphones and tablets. Moreover, after coming to the consumer market about 10 years ago, Flash-based solid-state drives are now in the process of replacing magnetic hard-disk drives.

The energetic structure and cross-section of a Flash cell are sketched in Fig. 1.3. In particular, Fig. 1.3b shows how a Flash cell is basically a field-effect transistor (FET) where a layer of dielectric ( $\text{SiO}_2$ ) is embedded between the gate (called *control gate*) and the channel (the 2-dimensional electron gas, 2DEG). The dielectric contains an inclusion of Si, called the *floating gate*, where the electrons are stored. The voltage applied to the control gate determines the electric field across the floating gate and the 2DEG, which can in turn

## 1. Solid-State Memories

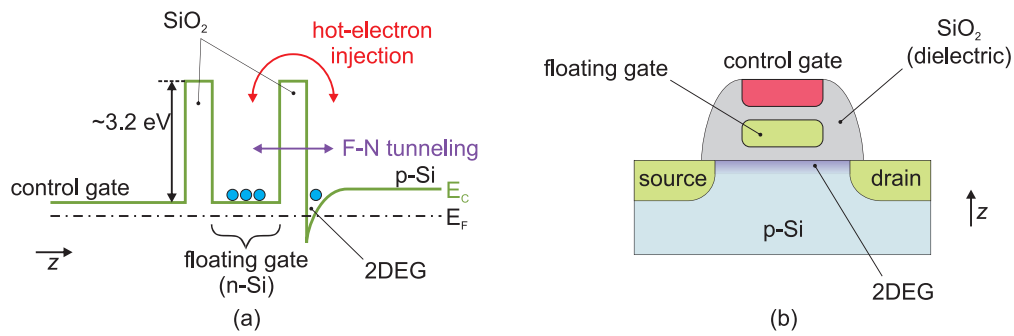


**Figure 1.3.:** Schematic representation of a Flash cell. (a) Structure of the conduction band along the  $z$  axis. Electrons are trapped inside the floating gate by the tall  $\text{SiO}_2$  barriers (middle), while more electrons accumulate in the 2DEG (right-hand side). The Fermi level lies below the conduction band. The transport mechanisms through the  $\text{SiO}_2$  barriers (hot-electron injection and Fowler-Nordheim tunneling) are marked in red and purple, respectively. (b) Cross section of a Flash cell (after [17]).

control the charge state of the floating gate via hot-electron injection or Fowler-Nordheim tunnelling. When electrons are localised in the floating gate, they generate an electric field which depletes the 2DEG [27]. Therefore, a simple conductance measurement on the 2DEG reveals the charge state of the cell.

Fig. 1.3a highlights the distinctive feature of a Flash memory, namely the 3.2-eV-tall barrier created by  $\text{SiO}_2$  around the floating gate. The considerable height of the barrier accounts for the main strength of Flash, namely its *non-volatility*: Since electrons are confined in such a deep potential well, information can be retained in a Flash cell for over 10 years without external energy supply. Moreover, the use of the 2DEG for the read-out operation is at the root of the relatively *low energy consumption* of Flash. On the one hand, the high sensitivity of the 2DEG implies that a single Flash cell needs only about 1000 electrons to store a bit; on the other hand, the read operation does not disturb the confined electrons, which remain inside the floating gate throughout the process. The read operation is, in other words, non-destructive.

The disadvantages of Flash are due to the fact that the barrier surrounding the floating gate is not tunable. If its height or thickness could be simply reduced during the write and erase operations, Flash could retain its non-volatility during normal storage and at the same time present write and erase times of the order of DRAM. However, since the energy mismatch between Si and  $\text{SiO}_2$  is fixed at 3.2 eV, other processes must be used to make the electrons cross the barrier during the write and erase operations, i.e. hot-electron injection and Fowler-Nordheim tunnelling. As mentioned above, these methods have the

major drawbacks of having a low injection efficiency and of damaging the barrier to the point that the whole cell becomes unusable. The disadvantages of Flash are hence *long write and erase times* (of the order of milliseconds) and *reduced durability* (the cell becomes unusable after about  $10^5$  write/erase cycles).

### 1.4. Alternative memory architectures

Since the limitations of Flash memory became apparent, and especially since the end of the development dominated by Moore's law came into sight, considerable effort has been invested in the development of alternative memory architectures for *storage-class memory*, most of them based on physical principles other than charge trapping. Storage-class memory (SCM) is a novel class of memories characterised by fast data access and non-volatility. Its place in the memory hierarchy (Fig. 1.1b) is between working memory and mass storage, ideally overtaking the role of both.

Burr et al. [28] offer an overview of alternative memory architectures, ranging from commercially available ones to ones still in early-development stage. The properties of the most promising alternative memory architectures are summarised below.

#### 1.4.1. FeRAM

Ferroelectric RAM (FeRAM) stores information inside a ferroelectric capacitor, i.e. a capacitor where the dielectric is a ferroelectric material, like lead zirconate titanate ( $\text{Pb}(\text{Zr}_x\text{Ti}_{1-x})\text{O}$ , PZT) or strontium bismuth tantalite ( $\text{SrBi}_2\text{Ta}_2\text{O}_9$ , SBT). The ferroelectric material causes the hysteresis loop of charge as a function of voltage to present two stable states at zero applied voltages, representing the two possible polarizations obtained by switching the spontaneous polarizations of the material [29, 30]. Each ferroelectric capacitor needs to be equipped with a selection device, such as a transistor, in order to avoid perturbing data stored in neighbouring cells. Read-out is performed by applying a voltage pulse that takes the device to one of the extremes of the hysteresis loop, thereby revealing the initial state. Unfortunately this reading process is destructive, so the information has to be rewritten after each reading. In spite of this, FeRAM used to be one of the strongest candidates for storage-class memory, especially thanks to its fast data access time, as low as 20 ns. However, FeRAM was largely ruled out because of its limited scalability. FeRAM remains nonetheless one of the most commercially successful alternative non-volatile memories, having being used for example in the popular Sony Playstation™ 2 system.

## 1. Solid-State Memories

### 1.4.2. MRAM

Magnetic RAM (MRAM) is based on *tunnelling magnetoresistance*: When two magnetic layers are separated by a dielectric, the amount of spin-polarized tunnelling current passing through the dielectric depends on the relative magnetization of the layers [31, 32]. In a typical MRAM cell, one of the layers has its magnetization pinned, while the magnetization of the other one can be flipped with the write operation. Every MRAM cell also needs to be equipped with a selection device because of small leak currents through unselected cells. MRAM is intrinsically very fast, easily integrated on silicon CMOS, and very durable (there is no known wear-out mechanism for magnetic switching). The main drawback for MRAM is the fact that the write currents remain very high ( $> 1$  mA) in spite of downscaling, which leads to wire damage in the long term. Several variants of MRAM have been proposed to obviate this problem and allow for downscaling to ultrasmall dimensions, the most fascinating of which is probably magnetic racetrack memory [33]. In racetrack MRAM the data is stored in magnetic domain walls on a magnetic racetrack extending in the third dimension. The read and write operations occur at a fixed sensor, while the domain walls can be moved along the racetrack using electrical currents. Even though very promising, this concept is still at an early development stage.

### 1.4.3. PCRAM

Phase-change RAM (PCRAM) takes advantage of the fact that the amorphous phase in phase-change materials often presents higher electrical resistivity than the crystalline phase [34]. The resistance contrast between the two phases is often as large as several orders of magnitude, making the read operation especially simple to implement. The write and erase operations are performed by heating the cell through an electrical current. The phase-change material crystallises when heated above its crystallisation temperature, and becomes amorphous again when heated to even higher temperatures and subsequently quenched by abruptly cutting off the heating current. PCRAM is very durable, fast, and intrinsically scalable. However, its main drawback is that increasing the density of cells might cause the memory access device to become too small to provide enough current for the erase operation.

### 1.4.4. Resistive switching memories

Other alternative memory architectures include resistive RAM (RRAM), solid-electrolyte (SE) memory, and organic and polymeric memory. RRAM is based on a special class of

materials which can be switched between two different resistance states by means of external voltages, like  $\text{Cu}_x\text{O}$ ,  $\text{NiO}$ ,  $\text{TiO}_x$ ,  $\text{ZrO}_x$ , and  $\text{HfO}_x$ . The specific mechanisms of resistive switching vary greatly from one material to the other and are often not well understood. SE memory consists of a solid-electrolyte material sandwiched between an inert electrode (cathode) and an oxidizable electrode (anode). Applying a positive voltage to the anode causes ion injection into the electrolyte, which starts depositing at the cathode, forming a filament that ends up connecting the electrodes. Once the electrodes are in contact the voltage drops abruptly. This process is reversible by applying an opposite voltage. Similarly, organic and polymeric memories are based on creating or interrupting contact between two electrodes by means of electrically-induced polymerization. Even though all these types of memories basically use resistive switching, their specific advantages and disadvantages vary greatly depending on the specific material used. All of them are at an early development stage [28].

## 1.5. Motivation of this work

As detailed in this chapter, the limitations of DRAM and Flash have been known for several years and a sizeable amount of energy and effort have been devoted to developing a novel memory architecture able to overcome them. As a matter of fact, already in 2005 the International Technology Roadmap for Semiconductors [35] stressed the importance of this endeavour by stating:

[The] development of *electrically accessible non-volatile memory with high speed and high density* would initiate a revolution in computer architecture.

Unfortunately, this “ultimate memory” has yet to be developed: In 2013, the last edition of the International Technology Roadmap for Semiconductors [5] still contained the very same sentence.<sup>3</sup> However, the brief overview given here is sufficient to define the features of such a memory:

**Storage time:** longer than 10 years, the definition of non-volatility.

**Data access time:** read, write and erase times should all lie below 10 ns; preferably 1 ns in order to completely eliminate the processor-memory bottleneck.

**Durability:** over  $10^{16}$  write/erase cycles.

---

<sup>3</sup>The chapter containing the quote was removed in 2014 with the introduction of ITRS 2.0, when the format of the report was completely restructured. The need for the ultimate memory, however, did not disappear with the chapter.

## 1. Solid-State Memories

**Charge consumption:** less than 1000 charge carriers per bit (in the case of charge storage memory). Ideally, the memory architecture should — at least in principle — be able to store information using as little as 1 charge carrier per bit in order to maximise its scalability.

**Voltages:** read, write and erase voltages should lie below 2.5 V for minimum power consumption and easier integration with surrounding electronic components. Ideally, the voltages should be matched to the CPU core voltage, which normally lies in the 1.0–1.5 V range [36].

These conditions are summarised in Tab. 1.1, alongside the corresponding values for industry-standard technology (SRAM, DRAM and Flash). As we will see in Ch. 4, QD-Flash [10–12] is a quantum-dot-based memory architecture able to meet all the requirements of the so-called “ultimate memory”. A QD-Flash demonstrator exhibited full functionality for temperatures up to 200 K [12, 13], and read and write times shorter than 10 ns were shown [15, 16], alongside erase times as low as 44 ns [37]. The longest storage time at room temperature measured in QD-Flash before the beginning of this work is 1.6 s [14].

	SRAM	DRAM	Flash	“Ultimate memory”
Storage time	n/a	64 ms	10 y	10 y
Read time	0.2 ns	< 10 ns	0.1 ms	10 ns
Write time	0.2 ns	< 10 ns	1 ms	10 ns
Erase time	0.2 ns	< 10 ns	0.1 ms	10 ns
Write cycles	$> 10^{16}$	$> 10^{16}$	$10^5$	$> 10^{16}$
Write voltage	1 V	2.5 V	15-20 V	< 1.5 V
Read voltage	1 V	1.8 V	4.5 V	< 1.5 V

**Table 1.1.:** Comparison of the performance of SRAM, DRAM, and Flash with the ideal “ultimate memory”. Values in green comply with the requirements for the ultimate memory; values in red do not; values in black are acceptable but not optimal (after the International Technology Roadmap for Semiconductors 2013 [5]).

The storage time at room temperature is the property of QD-Flash which needs to be improved the most, being still 8 orders of magnitude short of the required 10 years.<sup>4</sup> This work focuses precisely on this challenge, paving the way to the achievement of non-volatility in QD-Flash.

<sup>4</sup>10 years equal  $3 \times 10^8$  seconds.

## Summary

- Charge-storage memories are memory architectures that use charge carriers to represent the logic states “1” and “0”. The states are distinguished by the occupancy number of a metastable state defined by a dip in the potential energy.
- At present, memory architectures are organised in a hierarchy: Cache memory is typically very fast, volatile, and has low capacity (e.g. SRAM); working memory is fast, volatile, and has moderate capacity (e.g. DRAM); mass memory is slow, non-volatile, and has large capacity (e.g. Flash).
- Information technology would benefit immensely from a novel type of memory able to bridge the gap between working memory and mass storage. This type of memory is known as *storage class memory*. Storage class memory must be able to pair fast write, erase and read times (of the order of DRAM:  $\sim 10$  ns) with non-volatility (storage time  $> 10$  years, like Flash).
- Possible candidates for a storage class memory include FeRAM, MRAM, PCRAM, and resistive switching memories. Each of them has specific strengths and weakness, but until now none of them complies with all the requirements of the sought-for “ultimate memory”.
- QD-Flash memory, a novel memory architecture based on quantum dots, is a very promising candidate for the “ultimate memory”. The main goal of this work is to increase the room-temperature storage time in QD-Flash in order to bring it closer to the 10 years required for non-volatility.



## 2. Heterostructures and Nanostructures

La bellezza del cosmo è data non solo dalla unità nella varietà, ma anche dalla varietà nell'unità.

---

*(Umberto Eco)*

This chapter focuses on the building blocks of QD-Flash: semiconductor heterostructures and nanostructures. We will start with a brief overview of heterostructures and their fabrication, with a special emphasis on low-dimensional nanostructures. We will then move on to the two types of nanostructures that are most relevant to the present work: two-dimensional carrier gases and quantum dots (QDs). Since they lie at the core of QD-Flash, self-organised quantum dots will be discussed in particular detail, especially regarding fabrication, electronic structure, and modelling.

### 2.1. Semiconductor heterostructures

Semiconductor heterostructures are complex semiconductor structures formed by alternating layers of different semiconductors. In their present form they represent a relatively recent development in solid state physics, considering that their fabrication with modern quality standards requires the growth of almost atomically-abrupt epitaxial layers, which was enabled by the development of metalorganic chemical vapor deposition (MOCVD; also MVOPE: metalorganic vapour phase epitaxy) [38, 39] and molecular beam epitaxy (MBE) [39, 40].

MOCVD uses metalorganic precursors containing the chemical elements required for the formation of the desired semiconductors. The precursors are injected in gaseous form into the reactor, where they deposit onto the substrate. The substrate is kept at a high temperature in order to induce pyrolysis of the precursors. After pyrolysis the reaction by-products leave the reactor, whereas the required atoms remain on the substrate, where they form the epitaxial layer.

MBE is a more flexible technique which yields crystals of higher purity and quality,

## 2. Heterostructures and Nanostructures

but it is also much slower. In MBE elemental sources of the constituents of the desired semiconductor are directly evaporated into an ultrahigh vacuum (UHV) chamber containing the substrate. The molecular beams are directed towards the substrate surface, where they are deposited as an epitaxial layer.

Semiconductor heterostructures have found a plethora of applications, ranging from high-electron-mobility transistors (HEMT) [41, 42] to lasers [43, 44], amplifiers [45–47], and LEDs [48]. One very prominent application is the double heterostructure laser [49, 50], the invention of which won Zhores I. Alferov and Herbert Kroemer the Nobel prize in Physics in 2000 [51, 52]. Another important application of semiconductor heterostructures is the vertical-cavity surface-emitting laser (VCSEL [53]), where an array of alternating layers of different semiconductors form the Bragg reflectors used to enable lasing. VCSELs are at the core of the modern optical mouse [54] and show great promise for the development of optical interconnects for computers [55].

### 2.1.1. III–V semiconductors

A wide array of materials show semiconducting properties. The most important ones for technological applications are the *elemental semiconductors* from group 14 of the periodic table (group IV in the old classification): Si and Ge. *Compound semiconductors* can also be formed by combining elements of group 13 (III) with elements of group 15 (V) (*III–V compound semiconductors*), or elements of group 12 (II) and 16 (VI) (*II–VI compound semiconductors*). The elements commonly used for these types of compound semiconductors are: Zn, Cd, Hg (group 12); Al, Ga, In (group 13); P, As, Sb (group 15); and Se, Te (group 16). These materials can also be combined in variable stoichiometric proportions into ternary, quaternary, and even quinquenary alloys (e.g.  $\text{Al}_{0.3}\text{Ga}_{0.7}\text{As}$ ,  $\text{Al}_{0.1}\text{In}_{0.9}\text{P}_{0.5}\text{As}_{0.5}$ , ...), providing several degrees of freedom for tuning the properties of the resulting semiconductor (a technique called *band structure engineering*).

In this work we will concern ourselves exclusively with III–V semiconductors. In particular, this work focuses on GaSb and InGaAs QDs embedded in GaP. AlP is sometimes used because it forms an energy barrier in the valence band of GaP. The most important binary III–V semiconductors are represented by dots in Fig. 2.1, with their tertiary alloys represented by lines connecting them. A useful rule of thumb emerges from Fig. 2.1: the larger the lattice constant the smaller the band gap [56].

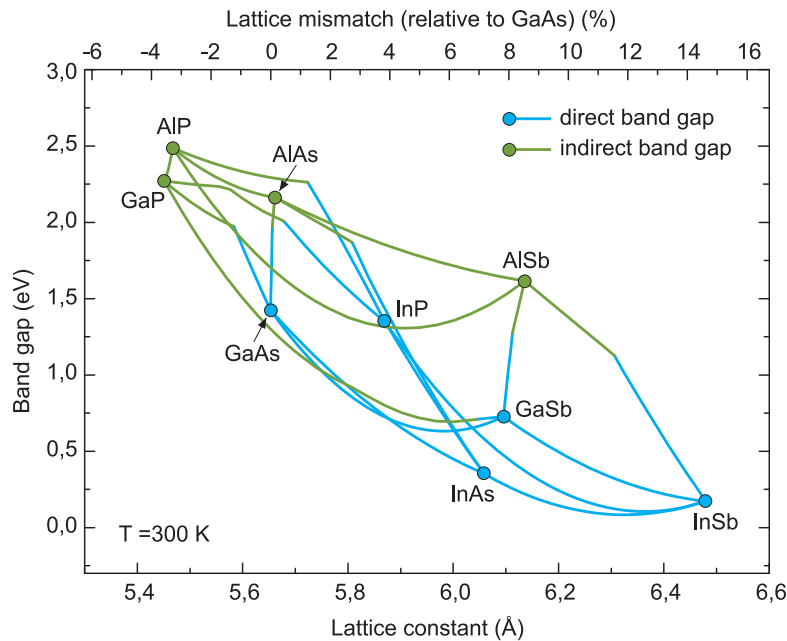


**Figure 2.1.:** Plot of band gap as a function of lattice constant at a temperature of 300 K for the most common III–V semiconductors, i.e. those with a zincblende crystal structure. The lines connecting the binary compounds represent their tertiary alloys. Materials in blue present a direct band gap, whereas materials in green present an indirect one. (After [56]).

### 2.1.2. Band alignment

The properties of a heterojunction depend decisively on how the band gaps of the different materials align. When two different semiconductors are brought into contact, charge carriers flow from one side to the other in order to bring the Fermi levels of the two materials to the same energy and achieve thermal equilibrium [57]. Since in general two different semiconductors will have different electron affinities and work functions, a band discontinuity will arise at thermal equilibrium. Three configurations are possible [6, 58]:

**Type-I** (Fig. 2.2a) The band gap of one semiconductor ( $E_g^2$ ) is completely contained inside the band gap of the other ( $E_g^1$ ). Confinement of both electrons and holes is possible. AlGaAs/GaAs and InAs/GaP are type-I heterojunctions.

**Type-II staggered** (Fig. 2.2b) Either the valence band edge or the conduction band edge of one semiconductors lies inside the gap of the other, but the other edge lies outside of it. Depending on the case confinement of either electrons or holes is possible, but not of both. InAs/GaSb and AlP/GaP are examples of staggered heterojunctions.

## 2. Heterostructures and Nanostructures

**Type-II broken gap or Type-III** (Fig. 2.2c) The band gap of one of the semiconductors lies completely above the band gap of the other. InAs/GaSb gives rise to a broken-gap heterojunction. This type of junction does not provide any confinement and is seldom seen in practical applications (except recently for solar cells [59, 60]).

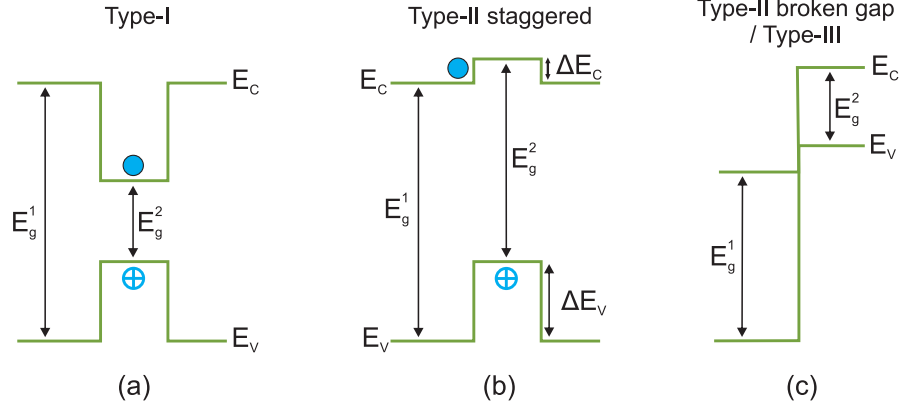


**Figure 2.2.:** Schematic representation of the three possible band alignments in semiconductor heterojunctions. Charge carrier localization is represented as a filled circle for electrons and a hollow circle with a “+” for holes. (a) Type-I. (b) Type-II staggered. In this example the discontinuity in the valence band  $\Delta E_V$  enables hole localization, but the discontinuity in the conduction band  $\Delta E_C$  does not enable electron localization, forming instead a barrier to the flow of electrons. The opposite case is also possible, in which only electrons are localized and not holes. (c) Type-II broken gap or Type-III.

QD-Flash is based on charge carrier localisation. Therefore, heterojunctions of type I and II are of interest for this work. Moreover, we will see in the following that QD-Flash operates by storing holes, so that heterojunctions of type II are preferable, with larger band discontinuities leading to longer storage times.

## 2.2. Nanostructures

Quantization effects begin dominating the behaviour of a particle as soon as its motion is restricted to dimensions comparable to its de Broglie wavelength, which can be written as:

$$\lambda = \frac{h}{p} = \frac{h}{\sqrt{3m^*k_B T}}, \quad (2.1)$$

where  $m^*$  is the effective mass,  $p$  the momentum,  $h$  the Planck constant,  $k_B$  the Boltzmann constant, and  $T$  the temperature. In semiconductors, the effective mass  $m^*$  can be considerably smaller than the mass of the free electrons  $m_0$  (for example, electrons

in GaAs at  $T = 300K$  present an effective mass  $m^* = 0.063m_0$  [6]). As a consequence quantization effects can arise already for restrictions far above the lattice constant.

The behaviour of the density of states for different degrees of spatial confinement is depicted in Fig. 2.3. Charge carriers in a bulk semiconductor are free to move in any spatial direction. The density of states  $D(E)$  is then proportional to  $\sqrt{E}$ , where  $E$  is the energy of the charge carrier (Fig. 2.3a). If motion is restricted in one spatial direction, we obtain a so-called *quantum well* (QW) (Fig. 2.3b), in which the density of states has a staircase shape due to the formation of several sub-bands of constant energy  $E_i$  [61]:

$$D_{2D}(E_i) = \frac{m^*}{\pi\hbar^2}, \quad (2.2)$$

where  $m^*$  is the effective mass and  $\hbar$  the reduced Planck constant. Restricting motion in one further spatial dimension results in a *quantum wire* (Fig. 2.3c). The density of states becomes then a series of “spikes”, each one proportional to  $1/\sqrt{E}$ . Finally, in a *quantum dot* motion is confined in all spatial dimensions (Fig. 2.3d). In this case, the density of states is discrete and can be expressed as [61]:

$$D_{QD}(E) = \sum_i \delta(E - E_i), \quad (2.3)$$

where  $E_i$  represent the energy levels inside the quantum dot. Eq. 2.3 resembles the density of states of the hydrogen atom, which explains why quantum dots are also referred to as “artificial atoms” [62].

### 2.3. Two-dimensional carrier gases

The two-dimensional case is especially important because the restriction of carrier movement in one spatial dimension creates a layer of very high mobility, which enabled the development of the *high-electron-mobility transistor* (HEMT), also known as *modulation-doped field-effect transistor* (MODFET) [6].

In order to create a two-dimensional carrier gas we need a quantum well to provide the two-dimensional confinement and the charge carriers to form the gas. The charge carriers can be provided by dopants, but once a dopant releases its charge carrier an ionised atom is left behind. If those atoms are placed inside the quantum well they will reduce the mobility of the carrier gas via Coulomb scattering [63], they will blur the energy levels, and they will disrupt the interference of carrier waves [61]. This problem can be circumvented with *remote* or *modulation doping* [64]: The dopants are placed outside the

## 2. Heterostructures and Nanostructures

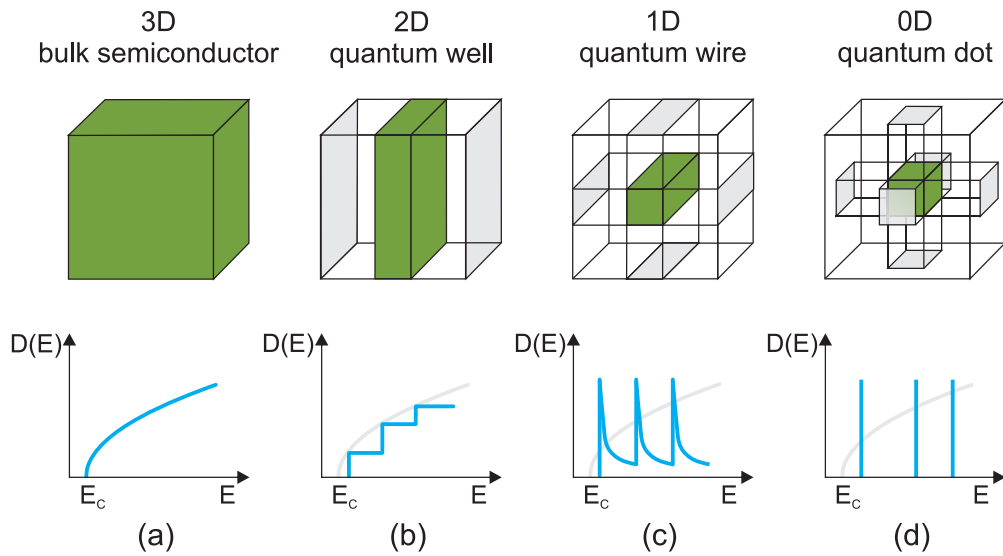


**Figure 2.3.:** Schematic representation of increasing degrees of spatial confinement in semiconductors (top row) and the resulting density of states (bottom row). (a) No spatial confinement (bulk semiconductor); density of state proportional to  $\sqrt{E}$ . (b) 2-dimensional confinement (quantum well); step-like density of states. (c) 1-dimensional system (quantum wire); spike-like density of states. (d) 0-dimensional system (quantum dot); discrete density of states. (After [7]).

quantum well and the charge carriers resulting from ionisation are made to flow into the well, thereby forming the carrier gas.

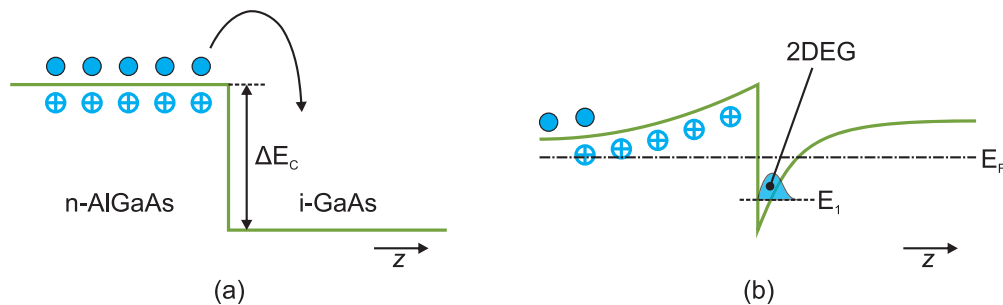


**Figure 2.4.:** Conduction band structure before and after the formation of a two-dimensional electron gas at the heterojunction interface between *n*-AlGaAs and *i*-GaAs. (a) Electrons diffuse from *n*-AlGaAs to *i*-GaAs and become trapped at the interface. (b) The flow of electrons lifts the Fermi level of *i*-GaAs up, creating a triangular band-bending at the interface. The electrons accumulate in the energy dip, forming a 2DEG. The blue sketch on the GaAs side represents the wave function of the ground state of the *z* quantization.

This process is exemplified for electrons in the AlGaAs/GaAs system in Fig. 2.4. AlGaAs and GaAs form a type-I heterojunction, with the band gap of GaAs completely

contained in the one of AlGaAs [56]. As a consequence, a thin layer of GaAs embedded in AlGaAs forms a quantum well both for electrons and holes. In Fig. 2.4 the AlGaAs has been doped negatively to produce an excess of electrons. Fig. 2.4a represents the conduction band structure when the junction has just been formed: The materials are neutral and the Fermi levels on the two sides of the junction are different. The electrons then start to diffuse from the AlGaAs side to the GaAs side. Once there, the discontinuity in the conduction band  $\Delta E_C$  prevents them from returning to the AlGaAs side in spite of the Coulomb attraction produced by the positive ions left behind. The electrons will then accumulate at the junction interface on the GaAs side, trapped in a field-induced triangular well with a typical width of  $\sim 10$  nm. Since the width of the well lies below the de Broglie wavelength of electrons, quantization along the  $z$  direction becomes relevant. If only the ground state is occupied, all electrons are in the same quantum state of the  $z$  quantization but remain free to move along the  $x$  and  $y$  directions. A two-dimensional electron gas (2DEG) is then formed (Fig. 2.4b) and the total energy of an electron populating its  $n$ th level can be expressed as [61]:

$$E_n(k_x, k_y) = E_n + \frac{\hbar^2 k_x^2}{2m^*} + \frac{\hbar^2 k_y^2}{2m^*}, \quad (2.4)$$

where  $k_x$  and  $k_y$  represent the wave vectors in the  $x$  and  $y$  directions, and  $m^*$  represents the effective mass. Modulation doping can be further improved by inserting an undoped spacer layer between doped layer and 2DEG. This technique yielded electron mobilities higher than  $10^7$  cm<sup>2</sup>/Vs in AlGaAs/GaAs at low temperatures ( $T < 1$  K) [65]. The achievement of such high mobilities at low temperatures enabled the discovery of the quantum Hall effect [66], which won Klaus von Klitzing the Nobel prize in 1985 [67].

A two-dimensional *hole* gas (2DHG) is formed analogously, but working on the valence band. For example, if we replace the n-AlGaAs in Fig. 2.4a with p-AlGaAs, a 2DHG will be formed at the junction interface with mobilities up to  $10^6$  cm<sup>2</sup>/Vs [68].

### 2.3.1. Modulation-doped field-effect transistor

The key feature of the MODFET — and its great advantage over conventional MOSFETs — is the very high mobility of the charge carriers in the channel, which is a two-dimensional carrier gas.

The structure of an enhancement-mode AlGaAs/GaAs MODFET is reported schematically in Fig. 2.5a. The epitaxial structure of the MODFET is a layer of n-AlGaAs grown on top of i-GaAs. As seen above, this configuration gives rise to a 2DEG at the interface,

## 2. Heterostructures and Nanostructures

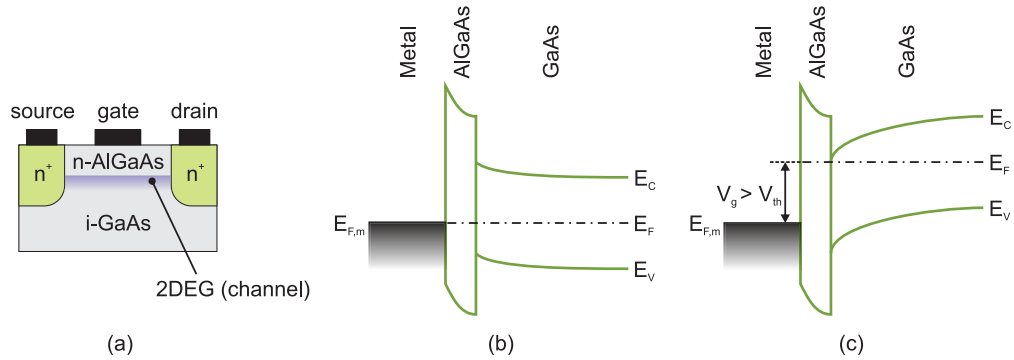


**Figure 2.5.:** Enhancement-mode modulation-doped field-effect transistor (MODFET). (a) Schematic cross section. (b) Band structure in the “off” state (gate voltage  $V_g = 0$  V). (c) Band structure in the “on” state ( $V_g > V_{th}$ , threshold voltage), with formation of a 2DEG in the conduction band at the heterojunction interface.

which constitutes the channel. Two highly-doped areas are created on either side of the channel in order to form the “source” and “drain” Ohmic contacts. The higher doping can be achieved either by ion implantation or by annealing of a previously deposited dopant. A Schottky contact is placed above the n-AlGaAs to control the charge carrier density in the 2DEG, as depicted in Fig. 2.5b and Fig. 2.5c. In Fig. 2.5b no external voltage is applied to the gate ( $V_g = 0$  V). The Fermi level is thus the same throughout the semiconductor and is equal to the Fermi level in the metal ( $E_F = E_{F,m}$ ), the source-drain conductance is very low, and the transistor is off. When the gate voltage is increased above a *threshold voltage*  $V_{th}$  (Fig. 2.5c), the Fermi level inside the device rises, thereby creating a bending in the conduction band where electrons accumulate to form a 2DEG. The conductance of the channel rises sharply and the transistor is on.

### 2.4. Self-organised quantum dots

Self-organised quantum dots (QDs) [7, 69] are a special case of the zero-dimensional semiconductor nanostructure discussed in Sc. 2.2 with the distinguishing feature that they arise *spontaneously* during growth (i.e. without the need for further processing after growth is completed). The special properties of semiconductor QDs resulted in several applications comprising lasers [70–75], high-frequency optical devices [76, 77], detectors [78, 79], amplifiers [80], single-photon sources [81–85], field-effect transistors [86, 87], and of course memories [88–93].

### 2.4.1. Fabrication

In general, QDs can be fabricated using either the *top-down* or *bottom-up* approach. In the top-down approach [7] a quantum well is prepared first by embedding a material of smaller band gap into one of wider band gap. Lithographic techniques (usually electron beam lithography) are used to define a mask on the surface of the sample. The mask is designed to create mesas of the appropriate lateral size to induce quantisation along the  $x$  and  $y$  axes. Once the sample is etched and the mask removed, the result is an array of mesas where carriers are confined in all three spatial dimensions:<sup>1</sup> An array of QDs is created. The top-down approach is intuitive and comparatively simple because it is derived from scaling down standard microelectronics techniques. The scaling, however, is limited by the resolution of the lithographic step.

Conversely, the bottom-up approach takes advantage of phenomena taking place at the nanoscopic level and is therefore better suited to the fabrication of semiconductor nanostructures. All samples used in this work were fabricated according to a bottom-up approach. This approach is based on epitaxial growth, which can be performed either via MOCVD or MBE (see Sc. 2.1 and [39] for further details on epitaxy technologies).

As mentioned in Sc. 2.1.1, different semiconductors present different lattice constants. However, epitaxial growth requires in principle that the lattice constant be the same throughout the whole crystal because atoms must align to stack on each other in an orderly and regular fashion. When growing a heterostructure three situations can arise:

1. In *matched growth* the lattice constants of the two materials are exactly the same. Atoms align with each other as if the crystal was made up of a single material. This is seldom the case in real applications.
2. In *strained growth* one of the materials is compressed or stretched out so that its lattice constant matches the one of the substrate it is being grown upon. This process creates a biaxial strain in the region near the interface which leads to a shift in the band edges [94]. Strained growth can only be sustained as long as the thickness of the epitaxial layer remains below a certain *critical thickness* which depends on the materials involved.
3. *Relaxed growth* begins as soon as the epitaxial layer reaches the aforementioned critical thickness. The energy stored into the strained bonds is released, partially relaxing the crystal structure by creating dislocations. Growth then proceeds with the original lattice constant of the material. Relaxed growth is normally undesirable

---

<sup>1</sup> $z$  quantisation is provided by the quantum well;  $x$  and  $y$  quantisation by the mesas.

## 2. Heterostructures and Nanostructures

in technological applications because the defects created during the relaxation process lower the quality of the device considerably and interfere heavily with the transport properties of the structure.

The critical thickness for strained growth depends on the lattice mismatch of the materials involved, with larger mismatches being associated with smaller critical thicknesses. In particular, the critical thickness is roughly inversely proportional to the lattice misfit [95]. The lattice misfit  $f$  is defined as:

$$f = \frac{a_0^{\text{sub}} - a_0^{\text{film}}}{a_0^{\text{film}}}, \quad (2.5)$$

where  $a_0^{\text{sub}}$  represents the unstrained lattice constant of the substrate and  $a_0^{\text{film}}$  that of the epitaxial layer. If  $t_c$  indicates the critical thickness we can then write  $t_c \sim 1/f$ .

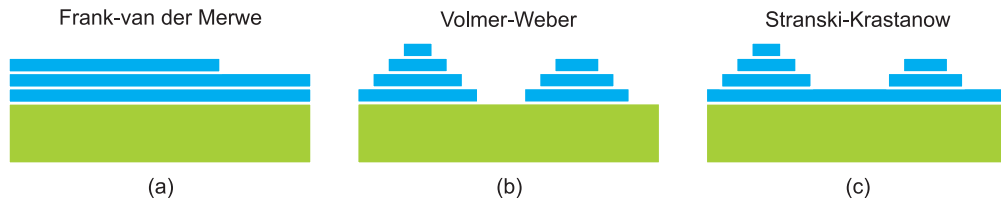


**Figure 2.6.:** Schematic representation of the three epitaxial growth modes: (a) Frank-van der Merwe, (b) Volmer-Weber, (c) Stranski-Krastanow.

Relaxation does not normally occur in the whole epitaxial layer at once. Sometimes the accumulated strain can lead to a transition from two-dimensional to three-dimensional growth mode, with the formation of islands where the strain is released and the total energy minimised [96]. There are three types of possible growth modes: Frank-van der Merwe (FM) [97], Volmer-Weber (VW) [98], and Stranski-Krastanow (SK) [99]. In *Frank-van der Merwe* growth (Fig. 2.6a), adatoms attach preferentially to surface sites resulting in atomically smooth, fully formed layers. Growth proceeds layer by layer, and the strain is relaxed gradually and without formation of dislocations across the first few layers from the interface. FM growth is typical of heterojunctions with very little lattice mismatch. In *Volmer-Weber* growth (Fig. 2.6b), adatoms attach preferentially to other adatoms. Non-contiguous islands start forming and grow three-dimensionally, leaving parts of the substrate exposed. Finally, *Stranski-Krastanow* growth (Fig. 2.6c) represents a mixture between FM and VW modes: The adatoms first cover the substrate completely, forming a so-called *wetting layer*, and then proceed to form three-dimensional islands. The islands have a lateral dimension of a few tens of nanometers and a height of a

## 2.4. Self-organised quantum dots

few nanometers [100], thereby fulfilling the conditions for quantization in all spatial directions, as specified in Eq. 2.1. The islands resulting from SK growth are *self-organised QDs* [7]. Once QDs have formed, they are normally overgrown with the matrix material (*capping*) so that they are completely surrounded by it in all spatial directions. The capping also allows for a contact to be placed above the QDs.

In this work we used exclusively (capped) QDs fabricated with SK growth.

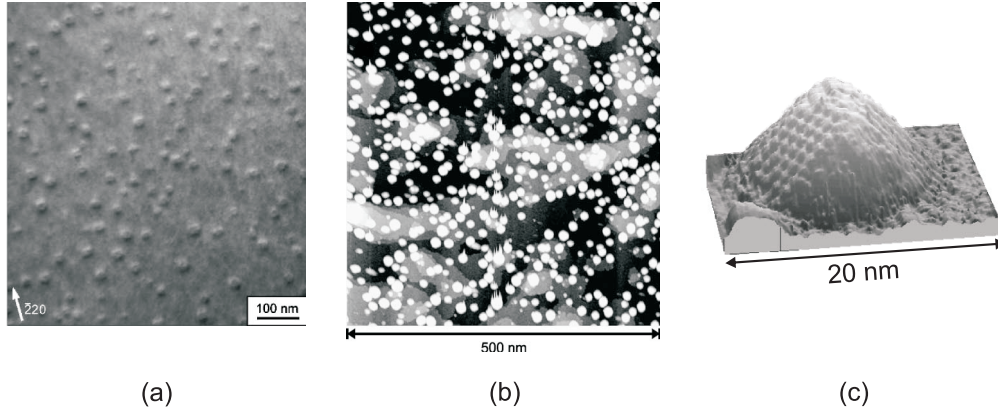


**Figure 2.7.:** (a) TEM image of GaSb/GaAs QDs with an areal density of  $3 \times 10^{10} \text{ cm}^{-2}$  (from [101]; courtesy of Appl. Phys. Lett.). (b) STM image of InAs/GaAs QDs with an areal density of  $1.9 \times 10^{11} \text{ cm}^{-2}$  (from [102]; courtesy of Prog. Surf. Sci.). (c) High-resolution STM image of a single uncapped InAs/GaAs QD (from [103]; courtesy of Appl. Phys. Lett.).

SK growth can result in QD densities up to  $10^{11} \text{ cm}^{-2}$ . Three microscope images of self-organised QDs are presented in Fig. 2.7 as an example. Fig. 2.7a shows a transmission electron microscope (TEM) image of GaSb/GaAs QDs. The QDs have an areal density of  $3 \times 10^{10} \text{ cm}^{-2}$ , a mean height of  $\sim 3.5 \text{ nm}$ , and a mean lateral dimension of  $26(\pm 4) \text{ nm}$  [101]. Fig. 2.7b shows a scanning tunnelling microscope (STM) image of InAs/GaAs QDs with an areal density of  $1.9 \times 10^{11} \text{ cm}^{-2}$ , a mean height of  $\sim 2.2 \text{ nm}$ , and a mean lateral dimension of  $12.5(\pm 1.0) \text{ nm}$  [102]. Finally, Fig. 2.7c shows a high-resolution STM image of a single uncapped InAs/GaAs QDs represented as a 3D model. The QD is  $\sim 3 \text{ nm}$  tall and  $\sim 15 \text{ nm}$  wide [103].

### 2.4.2. Modelling and electronic structure

To a first approximation, self-organised quantum dots can be described as three-dimensional potential wells of finite depth. This approximation results in a band structure of the type sketched in Fig. 2.8. Fig. 2.8 shows localisation of both electrons and holes in the QD. The internal electronic levels are marked as horizontal lines and labelled with

## 2. Heterostructures and Nanostructures

their energy:  $E_0^e, E_1^e, E_2^e$  for electrons;  $E_0^h, E_1^h, E_2^h$  for holes. The distance between the ground state for electrons (holes) and the edge of the conduction (valence) band is called *localization energy*  $E_{loc}^e$  ( $E_{loc}^h$ ) and it is equal to the energy of the ground state measured from the conduction (valence) band edge.

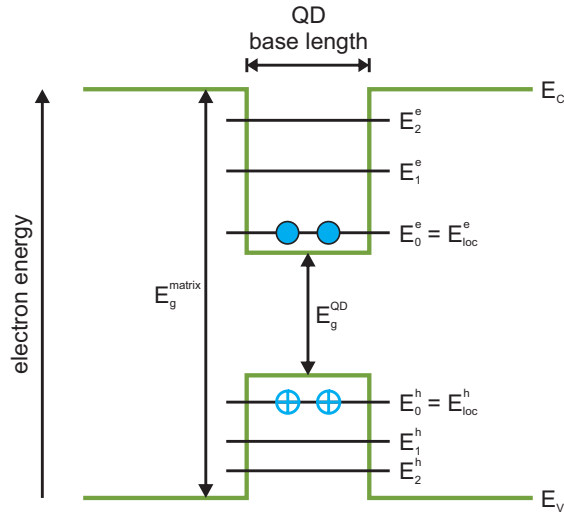


**Figure 2.8.:** Electronic structure of a quantum dot approximated with a finite potential well. The sketch shows a type-I quantum dot, able to confine both electrons and holes.

This simple model is useful for understanding qualitatively the electronic structure of QDs, but it neglects several important parameters like strain, piezoelectric effects, and the chemical composition of the QDs and of the surrounding matrix. More precise results can be obtained with the 8-band  $\mathbf{k} \cdot \mathbf{p}$  method [104–106], which takes all these parameters into account.

The method takes as input the known structural properties of the QDs (size, shape, composition...) and the properties of the matrix material. These properties are used to generate a strain map, which in turn is incorporated into the Hamiltonian of the system. The eigenstates of the Hamiltonian are then calculated taking into account the conduction band and the three valence bands (heavy-hole, light-hole, and split-off). Each of the bands has to be counted twice to account for the electron and hole spin. The total is eight bands, hence the name of the theory. The 8-band  $\mathbf{k} \cdot \mathbf{p}$  method is computationally very efficient and it requires knowledge of only a few of the parameters characterising the material system under study. Its main drawback is that it is only able to simulate the system in the close vicinity of the center of the Brillouin zone  $\Gamma$ , which is however sufficient within the scope of this work.

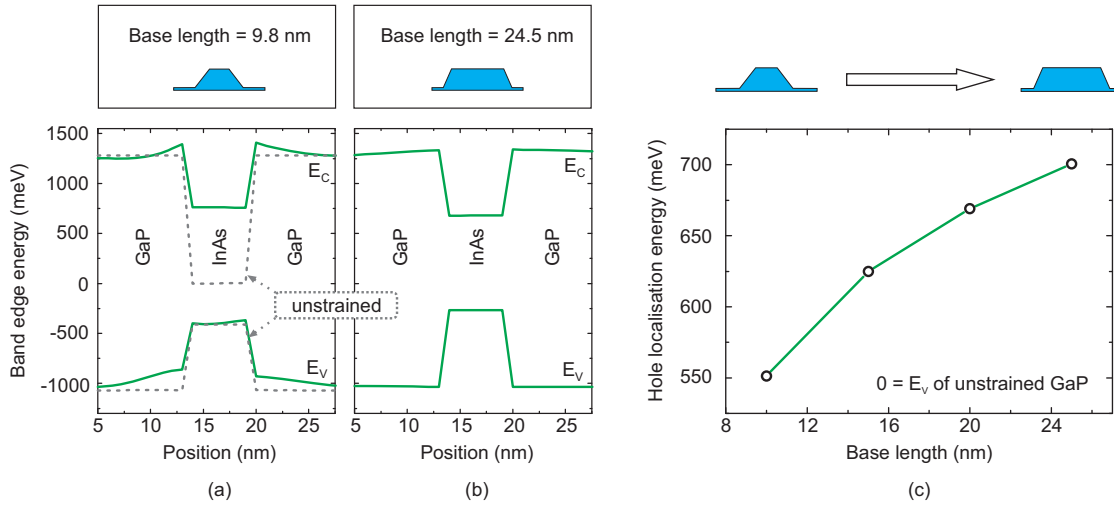


**Figure 2.9.:** Results of 8-band  $\mathbf{k} \cdot \mathbf{p}$  simulation of InAs QDs in GaP. (a) Band structure for QD base length 9.8 nm (green). The band alignment of the unstrained system is shown as a dashed grey line. (b) Band structure for QD base length 24.5 nm. (c) Hole localisation energy versus QD base length. (Courtesy of A. Schliwa, TU Berlin).

Two material systems were simulated by A. Schliwa at TU Berlin using 8-band  $\mathbf{k} \cdot \mathbf{p}$  theory: InAs/GaP QDs and GaSb/GaP QDs. The parameters for GaSb and GaP were taken from [56], those for InAs from [106].

The results of the simulation of the InAs/GaP QDs system are summarised in Fig. 2.9. Figs. 2.9a and 2.9b represent the effect of strain on the conduction and valence bands of the system (at the  $\Gamma$  point) for QDs of two different base lengths: 9.8 nm and 24.5 nm. The band configuration of the unstrained system is sketched as a grey dashed line in Fig. 2.9a. The system forms a type-I alignment both with and without strain. Strain, however, appears to deform the bands in the vicinity of the QD, strongly reducing electron localisation. For QDs of a larger base length (Fig. 2.9b) the strain at the base and at the tip of the QDs is reduced, and both electron and hole localisations are increased with respect to smaller QDs.

The hole localisation energy for different QD base lengths is shown in Fig. 2.9c, with  $E_{loc} = 0$  eV representing the valence band edge of unstrained GaP. The hole localisation energy of InAs/GaP QDs is 551 meV for a base length of 9.8 nm, and grows to 701 meV for a base length of 24.5 nm. The projected storage time at room temperature for the highest simulated localisation energy (701 meV) ranges from 5  $\mu$ s (calculated assuming a capture cross-section  $\sigma_{\infty} = 1 \times 10^{-9}$  cm<sup>2</sup>) up to 5 s (calculated assuming a capture cross-section  $\sigma_{\infty} = 1 \times 10^{-15}$  cm<sup>2</sup>).

## 2. Heterostructures and Nanostructures

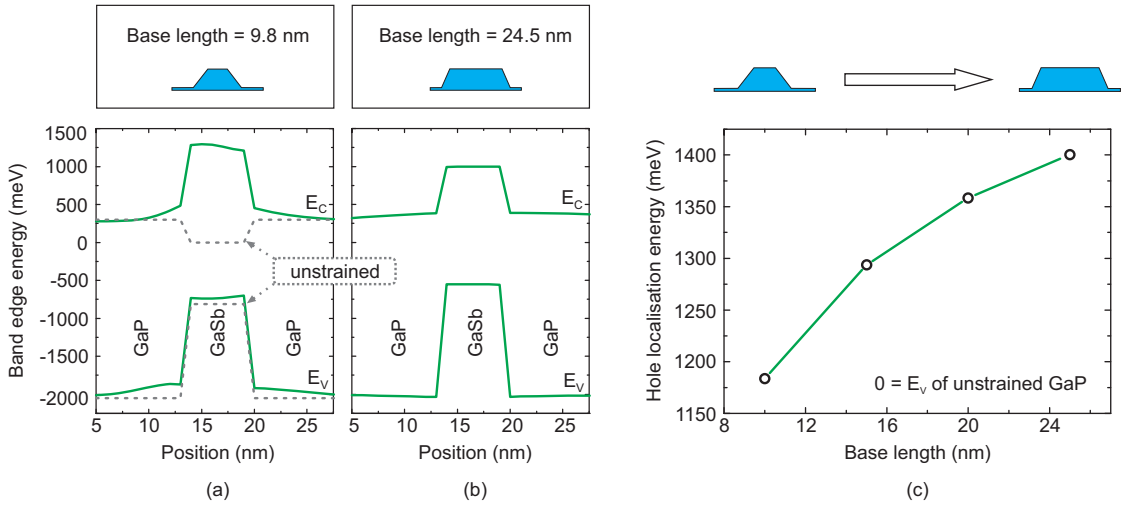


**Figure 2.10.:** Results of 8-band  $\mathbf{k} \cdot \mathbf{p}$  simulation of GaSb QDs in GaP. (a) Band structure for QD base length 9.8 nm (green). The band alignment of the unstrained system is shown as a dashed grey line. (b) Band structure for QD base length 24.5 nm. (c) Hole localisation energy versus QD base length. (Courtesy of A. Schliwa, TU Berlin).

Fig. 2.10 shows the results of the same simulation ran on the GaSb/GaP QDs system. One major difference becomes evident by comparing the unstrained band structure (dashed in gray in Fig. 2.10a) to the simulated band structures (green lines in Figs. 2.10a and 2.10b): The type-I alignment of the unstrained system is changed to a type-II alignment by strain (at the  $\Gamma$  point). The QDs lose in other words the ability to confine electrons. Hole localisation, on the other hand, increases (more markedly for a base length of 24.5 nm, Fig. 2.10b).

Fig. 2.10c reports hole localisation energy versus base length. Small QDs (base length 9.8 nm) result again in lower localisation energies (1184 meV), which grow up to 1400 meV for a base length of 24.5 nm. The projected hole storage times at room temperature for  $E_{loc} = 1400$  meV range between 30 days (for a capture cross-section  $\sigma_{\infty} = 1 \times 10^{-9} \text{ cm}^2$ ) and 90000 years (for a capture cross-section  $\sigma_{\infty} = 1 \times 10^{-15} \text{ cm}^2$ ).

### 2.4.3. Ensemble broadening

Self-organised quantum dots are not homogeneous in size, shape, and composition. The high number of QDs present in a sample can then be regarded as a statistical ensemble: The random distribution of physical parameters reflects into a Gaussian broadening of the energy levels. To give an idea of the order of magnitude of the phenomenon, the

#### 2.4. *Self-organised quantum dots*

ground state of InAs/GaAs QDs presents an ensemble broadening of  $\sim 30$  meV [107].

Ensemble broadening must be taken into account whenever it becomes larger than the energy separation between two adjacent levels. If this is the case, the separate resolution of the levels becomes impossible and the two levels are detected as a single one. However, ensemble broadening plays a marginal role in this work because the detection of single quantum levels is largely beyond its scope.

### Summary

- Epitaxial growth via MBE and MOCVD allows for stacking of layers of different semiconductors into *semiconductor heterostructures*. Depending on the band alignment, heterostructures are classified into *type-I*, *type-II staggered*, and *type-II broken gap*.
- III–V semiconductors can be combined into alloys, enabling the fine-tuning of their properties via *band structure engineering*.
- When the movement of charge carriers in a given spatial direction is confined to dimensions comparable to their de Broglie wavelength, the density of states along that direction becomes quantised. Different nanostructures are identified by the number of quantised spatial directions.
- Two-dimensional carrier gases (two-dimensional electron gas: 2DEG; two-dimensional hole gas: 2DHG) are formed when a quantum well is populated with charge carriers. 2DEGs/2DHGs are implemented as channels in MODFETs.
- Self-organised quantum dots are a zero-dimensional system, formed spontaneously in strained heterostructures via Stranski-Krastanow growth.
- Quantum dot localisation energies can be calculated using 8-band  $\mathbf{k} \cdot \mathbf{p}$  theory. According to simulations, larger QD sizes tend to yield higher localisation energies. The projected hole localisation energy of the InAs/GaP QDs system is 701 meV; that of the GaSb/GaP QDs system 1.4 eV (calculated for a QD size of 24.5 nm).

## 3. Charge-carrier dynamics in quantum dots

God runs electromagnetics by wave theory on Monday, Wednesday, and Friday, and the Devil runs them by quantum theory on Tuesday, Thursday, and Saturday.

---

*(Sir William Bragg)*

This chapter provides the theoretical framework describing capture and emission of charge carriers from quantum dots. These processes are central to this work because they underlie charge storage in quantum dots. In the following, we will describe at first the different types of capture and emission processes, then proceed to apply rate equation and detailed balance to derive an analytical expression for the respective rates. We will also discuss briefly some important effects able to influence said rates, namely many-particle effects [108, 109] and Poole-Frenkel effect [110].

The following description was originally developed for deep traps in semiconductors [111, 112]. The idea that it applies also to self-organised quantum dots comes from the similarity of their electronic structure to that of deep traps, especially if one focuses on the ground state of the quantum dots. Ample experimental proof exists that this is indeed the case [113–116], which justifies the choice of applying this theoretical framework to the case in study.

### 3.1. Emission processes

As we have seen, self-organised QDs are able to localise charge carriers for a limited amount of time. The length of the localisation time depends on the (finite) probability of emission of the charge carriers from the QDs. There are four kinds of emission from QDs [111]: *thermal emission*, *tunnel emission*, *thermally-assisted tunnelling*, and *optical excitation*. The experiments reported in this work are all run in darkness, so that optical excitation is excluded. The remaining processes are depicted in Fig. 3.1a and will be now described

### 3. Charge-carrier dynamics in quantum dots

in detail.

**Thermal emission** means that charge carriers are emitted through *exclusively thermally-activated* processes. In order for thermal emission to take place, a charge carrier has to absorb enough thermal energy to be able to overcome the emission barrier  $E_B$ . The thermal emission rate depends on the temperature of the system and on the height of the emission barrier  $E_B$ .

**Tunnel emission** takes place when a charge carrier is able to tunnel through the barrier *directly* into a free state in the valence or conduction band. The tunnelling rate depends on the height and shape of the barrier, and on the electric field in the vicinity of the QD.

**Thermally-assisted tunnelling** consists in a combination of thermal emission and tunnel emission. A charge carrier is thermally excited into a higher bound level of the QD, where the probability of tunnelling into the valence or conduction band is higher because the barrier is thinner (see Fig. 3.1a). The thermally-assisted tunnelling rate depends on the height and on the shape of the barrier, on the temperature of the system, and on the electric field.

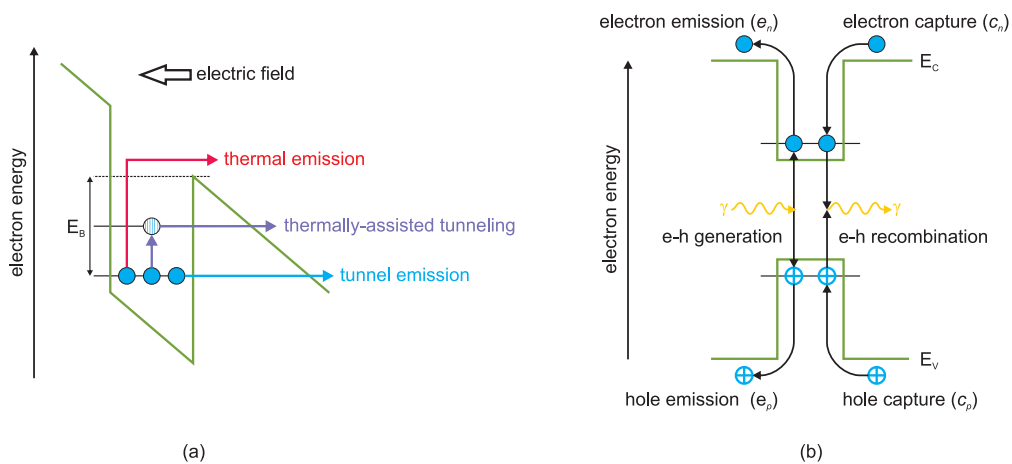


**Figure 3.1.:** (a) Electron emission processes from quantum dot states under an electric field (optical processes not depicted).  $E_B$  represents the height of the emission barrier. (b) Schematic depiction of all processes changing the occupancy of quantum dot states.

### 3.2. Rate equation

In general, the occupancy of an electron state can be changed by the following four processes [111] (sketched in Fig. 3.1b):

- Electron capture from the conduction band (occurring at a rate  $c_n$ );
- Electron emission to the conduction band (occurring at a rate  $e_n$ );
- Electron-hole pair generation (i.e. capture of electrons from the valence band);
- Electron-hole pair recombination (i.e. emission of electrons into the valence band).

Symmetrically, four processes can be identified for holes in the so-called “hole picture” (also sketched in Fig. 3.1b):

- Hole capture from the valence band (occurring at a rate  $c_p$ );
- Hole emission to the valence band (occurring at a rate  $e_p$ );
- Electron-hole pair generation (i.e. capture of holes from the conduction band);
- Electron-hole pair recombination (i.e. emission of holes into the conduction band).

As mentioned before, optical processes are not relevant to this work because all the experiments take place in the dark. Moreover, the large band gap of the materials involved further hinders optical generation. Recombination can also be excluded because in the samples under consideration the density of minority charge carriers is always several orders of magnitude smaller than the density of majority charge carriers. In the following we will thus focus only on single-charge-carrier capture and emission processes.

We will use the index  $n$  for electrons,  $p$  for holes, and QD for quantum dots. The density of quantum dots will be written  $N_{\text{QD}}$  and the density of occupied electron and hole states  $n_n$  and  $n_p$ , respectively. It follows that the density of unoccupied electron and hole states will be  $u_n = N_{\text{QD}} - n_n$  and  $u_p = N_{\text{QD}} - n_p$ . We can then write the *net emission rate* of electrons from QDs  $R_n^e(t) = e_n n_n(t)$  and the *net capture rate* of electrons into QDs  $R_n^c(t) = c_n u_n(t)$ . The former describes the change in the occupancy of occupied electron states, whereas the latter describes the change in the occupancy of unoccupied electron states. Both these rates are time-dependent. The time-independent rates  $e_n$  and  $c_n$  are to be understood per occupied and unoccupied electron state, respectively. For holes we can write symmetrically the net emission rate from QDs  $R_p^e(t) = e_p n_p(t)$  and the net capture rate into QDs  $R_p^c(t) = c_p u_p(t)$ .

### 3. Charge-carrier dynamics in quantum dots

Let us focus on electrons first. The change in occupancy of the electron states in time  $dn_n(t)/dt$  must equal the sum of the net emission and capture rates:

$$\frac{dn_n(t)}{dt} = R_n^c(t) - R_n^e(t) = c_n[N_{\text{QD}} - n_n(t)] - e_n n_n(t), \quad (3.1)$$

which is a first-order inhomogeneous differential equation. The solution for the initial condition  $n_n = n_n^0$  for  $t = 0$  is:

$$n_n(t) = n_n^\infty - (n_n^\infty - n_n^0) \cdot \exp[-(e_n + c_n)t], \quad (3.2)$$

where  $n_n^\infty$  indicates the equilibrium occupancy for  $t \rightarrow \infty$ . We can derive  $n_n^\infty$  by imposing  $dn_n(t)/dt = 0$  for  $t \rightarrow \infty$ :

$$n_n^\infty = N_{\text{QD}} \left( \frac{c_n}{e_n + c_n} \right). \quad (3.3)$$

We can then interpret the sum of the rates  $e_n + c_n$  as the inverse of the time-constant of the process  $\tau$ :

$$\frac{1}{\tau} = e_n + c_n \quad (3.4)$$

and rewrite Eq. 3.2 as:

$$n_n(t) = n_n^\infty - (n_n^\infty - n_n^0) \cdot \exp\left(-\frac{t}{\tau}\right). \quad (3.5)$$

Eq. 3.5 says that whenever the density of occupied electron states is changed from its equilibrium value  $n_n^\infty$  to  $n_n^0$  the system will relax back to  $n_n^\infty$  following a monoexponential decay with time constant  $\tau = 1/(e_n + c_n)$ . The derivation is identical for holes, for which we can write:

$$n_p(t) = n_p^\infty - (n_p^\infty - n_p^0) \cdot \exp\left(-\frac{t}{\tau}\right), \quad (3.6)$$

with  $\tau = 1/(e_p + c_p)$ .

The total rates which determine the time constant are in fact given by the combination of the rates for thermal emission, tunnel emission, and thermally-assisted tunnelling. The rates of each one of these processes are derived analytically in the following.

### 3.3. Capture processes

Capture processes occur in quantum dots in two steps: First a charge carrier has to be captured from the conduction or valence band into the quantum dot, then the charge

carrier relaxes down to the ground state of the quantum dot. If no capture barrier is present — which is normally the case in this work, since the system is brought into flatband configuration prior to capture — thermal capture occurs on the timescale of picoseconds [8, 9].

Concerning the relaxation step, it was previously thought that the zero-dimensionality of QDs and the lack of phonons would delay the relaxation, a hypothesis known as *phonon bottleneck* [117]. It was later understood that processes like Auger scattering, multiple LO-phonon emission, and electron-hole scattering are able to efficiently dissipate the energy of the charge carriers [8, 118, 119].

The capture of charge carriers into QDs is described with a semi-classical approach analogous to the one used in nuclear physics. A *capture cross-section*  $\sigma_n$  ( $\sigma_p$  for holes) is defined as an empirical constant representing the probability that any charge carrier be captured into the quantum dot. The capture cross section depends on temperature because of non-radiative capture processes and because of the dissipation involved in the relaxation to the ground state [111, 119]. However, it has been shown that the temperature dependence of the capture cross-section in QDs can be neglected [120]. In this model, the capture rate for electrons is given by the product of the capture cross-section and the electron flux at the position of the QD, i.e. the product of the density of electrons in the vicinity of the QD ( $n_{\text{QD}}$ ) and their mean thermal velocity  $\langle v_n \rangle = \sqrt{\frac{3k_B T}{m^*}}$ , with  $m^*$  the effective mass of the electrons in the conduction band:

$$c_n = \sigma_n \langle v_n \rangle n_{\text{QD}}. \quad (3.7)$$

Analogously for holes:

$$c_p = \sigma_p \langle v_p \rangle p_{\text{QD}}. \quad (3.8)$$

### 3.3.1. Many-particle effects

If more than one charge carrier is confined in a QD, as is often the case in the experiments carried out in this work, the interaction between different charge carriers has to be taken into account. First and foremost, the band structure in the vicinity of the QD will be modified by the electric field generated by the charge carrier, as depicted (for electrons) in Fig. 3.2a. As soon as one electron is confined in the QD, any further electron will have to overcome the additional barrier  $\Delta E_C$  created by the Coulomb interaction with the confined electron. At the same time, the spin degeneracy of the ground state of the QD is lifted and its potential energy is increased by the same amount  $\Delta E_C$ . As a result, the

### 3. Charge-carrier dynamics in quantum dots

effective emission barrier remains the same and the Coulomb interaction is not detectable in the DLTS experiments carried out in this work.

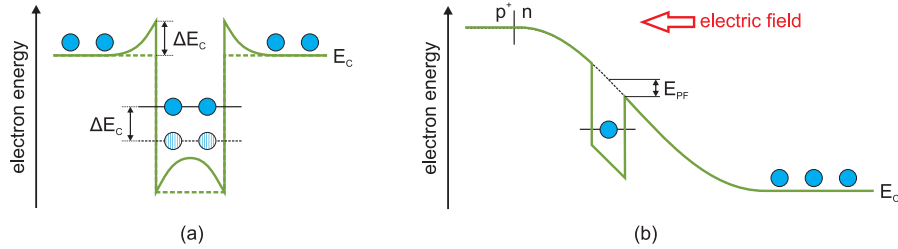


**Figure 3.2.:** (a) Conduction band bending caused by electrons localised in a quantum dot. The energy of the ground state is lifted by  $\Delta E_C$  and a capture barrier of height  $\Delta E_C$  is created. (b) The emission barrier from quantum dots subject to an electric field is lowered by  $E_{PF}$  due to the Poole-Frenkel effect [110].

Another many-particle effect relevant to the capture of charge carriers into quantum dots is the exchange interaction due to the Pauli exclusion principle: Since charge carriers are fermions, they cannot occupy the same level inside the QD unless their spins are antiparallel [121].

The individual contributions of Coulomb and exchange interactions in QDs were calculated in [108] for two-dimensional QDs with a parabolic potential and in [109] for more realistic geometrical shapes and potentials using 8-band  $\mathbf{k} \cdot \mathbf{p}$  theory. The results are not reported here because the effects are not detectable via DLTS and are therefore not relevant to this work.

#### 3.3.2. Poole-Frenkel effect

The Poole-Frenkel effect [110] was originally used to explain conduction in insulators: Even though electrons in insulators are strongly bound to their atoms, they are sometimes able to transition briefly to the conduction band via thermal fluctuations. If the electric field is intense enough, the electron might have enough time to travel to a neighbouring atom before being captured again into the valence band. This “hopping” transport of electrons can give rise to a small current through the insulator.

In the case of self-organised quantum dots, the Poole-Frenkel effect effectively lowers the emission barrier in presence of an electric field by  $E_{PF}$  (see Fig. 3.2b). Since in capacitance spectroscopy the quantum dots are located in the depletion layer of a p-n junction, they are subject to the electric field generated by the ionised dopants and the Poole-Frenkel effect has to be taken into account. However, for the bias voltages used in

DLTS, the correction amounts to  $E_{\text{PF}} \simeq 10$  meV and can thus be neglected.

### 3.4. Emission rates

The emission processes relevant to this work have been summarised in Fig. 3.1a. We will now proceed to derive the analytical expressions for the individual emission rates.

#### 3.4.1. Thermal emission rate

To derive the thermal emission rate we will start from the mean occupation of the quantum dots in equilibrium, as given by Eq. 3.3:

$$\frac{n_n^\infty}{N_{\text{QD}}} = \left( \frac{c_n}{e_n + c_n} \right). \quad (3.9)$$

On the other hand, the mean occupancy of an electron state in equilibrium must be described by the Fermi-Dirac distribution [111]:

$$\frac{n_n^\infty}{N_{\text{QD}}} = \frac{1}{1 + \frac{g_0}{g_1} \exp\left(\frac{E_0 - E_F}{kT}\right)}, \quad (3.10)$$

where  $E_0$  is the energy of the level in the QD,  $E_F$  is the Fermi energy of the system,  $g_0$  is the spin degeneracy of the unoccupied state, and  $g_1$  is the spin degeneracy of the occupied state. For a common spin-degenerate state,  $\frac{g_0}{g_1}$  equals  $\frac{1}{2}$  [122]. By equating the right-hand side of Eq. 3.9 and Eq. 3.10 and using the expression for  $c_n$  from Eq. 3.7 we obtain:

$$e_n^{\text{th}} = \sigma_n \langle v_n \rangle n_{\text{QD}} \frac{g_0}{g_1} \exp\left(\frac{E_0 - E_F}{kT}\right). \quad (3.11)$$

If the semiconductor is neutral and non-degenerate<sup>1</sup>, the density of free electrons is given by the Boltzmann distribution [6]:

$$n_{\text{QD}} = N_C \exp\left(-\frac{E_C - E_F}{k_B T}\right), \quad (3.12)$$

---

<sup>1</sup>A semiconductor is non-degenerate when the density of free electrons  $n_{\text{QD}}$  is smaller than the effective density of states in the conduction band. Equivalently, a semiconductor is non-degenerate if the Fermi energy is at least  $3k_B T$  away from either band edge. A qualitative interpretation of the condition of non-degeneracy is that the density of charge carriers is “low enough” for the behaviour of the system to be that of a typical semiconductor, whereas degenerate semiconductors behave “almost like” conductors. Moreover, non-degeneracy implies that the density of charge carriers can be approximated with the Boltzmann distribution.

### 3. Charge-carrier dynamics in quantum dots

where  $N_C = 2 \left( \frac{2\pi m_n^* k_B T}{h^2} \right)^{\frac{3}{2}}$  is the effective density of states at the conduction band edge.

We can now use Eq. 3.12 to rewrite Eq. 3.11 as:

$$e_n^{\text{th}} = \sigma_n \langle v_n \rangle N_C \frac{g_0}{g_1} \exp \left( -\frac{E_C - E_0}{k_B T} \right), \quad (3.13)$$

and symmetrically for holes:

$$e_h^{\text{th}} = \sigma_p \langle v_p \rangle N_V \frac{g_0}{g_1} \exp \left( -\frac{E_0 - E_V}{k_B T} \right), \quad (3.14)$$

where  $N_V$  is the density of states for holes at the valence band edge,  $E_V$  is the energy of the valence band edge, and  $E_0$  is the energy of the hole state in the quantum dot.

The energetic differences  $E_C - E_0$  and  $E_0 - E_V$  represent the emission barriers for electrons and holes, respectively, and are also known as *activation energies*  $E_a$ :  $E_a^e = E_C - E_0$  for electrons and  $E_a^h = E_0 - E_V$  for holes.

As mentioned in Sc. 3.3, the temperature dependence of the capture cross-section is negligible. We can then replace  $\sigma(T)$  with its value for  $T \rightarrow \infty$ :  $\sigma^\infty$ . Moreover, we can simplify Eq. 3.13 and Eq. 3.14 by grouping all pre-factors into a constant  $\gamma$ , which depends only on the matrix material. We then obtain for electrons:

$$e_n^{\text{th}}(T, E_a^e) = \gamma_n T^2 \sigma_n^\infty \exp \left( -\frac{E_a^e}{k_B T} \right) \quad (3.15)$$

and for holes:

$$e_p^{\text{th}}(T, E_a^h) = \gamma_p T^2 \sigma_p^\infty \exp \left( -\frac{E_a^h}{k_B T} \right). \quad (3.16)$$

Once written in this form, it becomes evident that the plot of  $\ln[e^{\text{th}}/(\gamma T^2)]$  against  $T^{-1}$  results in a straight line. This is known as *Arrhenius plot*. The steepness of the Arrhenius plot yields the activation energy  $E_a$ , and its  $y$ -intercept the capture cross-section  $\sigma$ .

#### 3.4.2. Tunnel emission rate

In general, the tunnelling probability of a particle through an energy barrier depends on its height, shape, and thickness. These properties are often expressed through the normalised tunnelling probability, called *transparency* of the barrier ( $T$ ). The derivation of the transparency involves rather long quantum mechanical calculations and lies outside

the scope of this work.

Since in this work we focus on quantum dots embedded in p–n junctions, the effective barrier seen by the confined charge carriers is a triangular one (see Fig. 3.1a). In this special case the transparency becomes [123]:

$$T(F, E_B) = \exp\left(-\frac{4}{3q\hbar F} \cdot \sqrt{2m^* E_B^3}\right), \quad (3.17)$$

where  $F$  is the electric field and  $E_B$  the height of the emission barrier. This expression can be extended to barriers of arbitrary shape using the WKB method,<sup>2</sup> which results in the more general expression [121]:

$$T(F, E_B) \simeq \exp\left[-\frac{2}{\hbar} \cdot \int_{z_0}^{z_1} \sqrt{2m^* \cdot (V(z, F) - E_B)} dz\right], \quad (3.18)$$

where  $z_0$  and  $z_1$  are the start and finish points of the tunnelling path, and  $V(z)$  is the shape of the position-dependent height of the barrier. The tunnel emission rate can thus be written:

$$e^{\text{tun}}(F, E_B) = \frac{qF}{4\sqrt{2m^* E_B}} \cdot \exp\left[-\frac{2}{\hbar} \cdot \int_{z_0}^{z_1} \sqrt{2m^* \cdot (V(z, F) - E_B)} dz\right]. \quad (3.19)$$

The previous expression can be applied to electrons or holes by substituting the appropriate  $E_B$  and  $m^*$ .

### 3.4.3. Thermally-assisted tunnelling rate

Thermally-assisted tunnelling can be understood as the thermal excitation of a charge carrier to a higher (real or virtual) energy level, followed by direct tunnelling through the barrier, which in the case of a triangular barrier will be thinner (see Fig. 3.1a). A charge carrier is thermally excited to the intermediate level  $E_i$  at a rate  $e^{\text{th}}(T, E_B - E_i)$ , and tunnels from the state  $E_i$  through the barrier at a rate  $e^{\text{tun}}(F, E_i)$ . The thermally-assisted tunnelling rate is then given by the product of the two rates:

$$e^{\text{tat},i}(T, F, E_B, E_i) = \gamma T^2 \sigma \cdot \exp\left(-\frac{E_B - E_i}{k_B T}\right) \cdot \exp\left[-\frac{2}{\hbar} \cdot \int_{z_0}^{z_1} \sqrt{2m^* \cdot (V(z, F) - E_B)} dz\right]. \quad (3.20)$$

<sup>2</sup>The *Wentzel-Kramers-Brillouin method* (also known as *Liouville-Brillouin* or *Jeffreys-Wentzel-Kramers-Brillouin method*) is used to find approximate solutions to linear differential equations with spatially varying coefficients. More details can be found in [61].

### 3. Charge-carrier dynamics in quantum dots

Eq. 3.20 must now be integrated over all the possible intermediate states  $E_i$ . The result is:

$$e^{\text{tat}}(T, F, E_B) = \gamma T^2 \sigma \cdot \int_0^{E_B} \exp\left(-\frac{E_B - E_i}{k_B T}\right) \cdot \exp\left[-\frac{2}{\hbar} \cdot \int_{z_0}^{z_1} \sqrt{2m^* \cdot (V(z, F) - E_B)} dz\right] dE_i, \quad (3.21)$$

again in the general form for electrons and holes.

#### 3.4.4. Total emission rate

The total emission rate is given by the sum of all the emission rates. Vincent, Chantre, and Bois [123] propose that the total emission rate is given by the sum of the thermal emission rate and the thermally-assisted tunnelling rate [123]:

$$e^{\text{tot,VCB}}(T, F, E_B) = e^{\text{tat}}(T, F, E_B) + e^{\text{th}}(T, E_B). \quad (3.22)$$

However, Marent [37] pointed out that in this case the total emission rate would always become zero for  $T \rightarrow 0$ . They therefore propose that the pure tunnelling rate also be added separately to the sum :

$$\boxed{e^{\text{tot}}(T, F, E_B) = e^{\text{tat}}(T, F, E_B) + e^{\text{th}}(T, E_B) + e^{\text{tun}}(F, E_B)}. \quad (3.23)$$

This hypothesis was confirmed in the same work [37], in simulations for GaSb QDs in a p-n junction [124], and experimentally for GaAsSb/GaAs QDs [125].

### Summary

- Charge carrier emission from QDs occurs via thermal emission, tunnelling emission, thermally-assisted tunnelling, or optical recombination. Within the scope of this work, optical recombination can be safely ignored because all experiments were carried out in darkness. The rate equation for emission processes is derived from detailed balance.
- Charge carrier capture into QDs occurs via thermal capture and subsequent relaxation into the ground state. The relaxation involves energy dissipation through various processes (Auger scattering, electron-hole scattering, ...). The total capture probability is expressed empirically by the *capture cross-section*  $\sigma$  ( $\sigma_p$  for holes;  $\sigma_n$  for electrons).  $\sigma$  depends on all processes involved in the relaxation.
- Analytical expressions can be derived for thermal emission rate, tunnelling emission rate, and thermally-assisted tunnelling rate. The total emission rate is given by the sum of the partial emission rates.



## 4. QD-Flash

A complex system that works is invariably found to have evolved from a simple system that works.

---

*(John Gall)*

QD-Flash is the name of a concept for a *quantum-dot based non-volatile memory* inspired by the Flash architecture. The concept was developed at Technische Universität Berlin by A. Marent, M. P. Geller, and D. Bimberg [10–12]. The defining features of QD-Flash are:

1. use of III-V semiconductors for the fabrication of the devices;
2. charge-based storage in self-organised quantum dots;
3. storage of holes instead of electrons;
4. embedding of the quantum dots in a MODFET structure.

The structure of a generic QD-Flash cell is sketched in Fig. 4.1. The quantum dot layer is embedded between the gate and the channel of a p-channel depletion MODFET. The channel — which is a 2DHG — is populated by holes released by a highly-doped layer placed below it ( $\delta$ -doping). The channel is contacted to source and drain via annealing, which creates a highly-doped region extending from the source and drain contacts down to the channel.

As discussed in Sc. 2.1.1, III–V semiconductors are a very flexible family of materials. The properties of heterostructures based on III–V semiconductors can be adjusted by means of substituting one material for another, creating alloys and varying their composition, and doping. This allows for engineering of the band structure to a much greater extent than the Si/SiO<sub>2</sub> combination employed in conventional Flash memory, where the only degree of freedom is the doping of the silicon. Moreover, almost atomically-abrupt heterointerfaces can be realised in structures based entirely on III–V semiconductors, owing to the fact that the entirety of the growth process is carried out inside an MOCVD

#### 4. QD-Flash

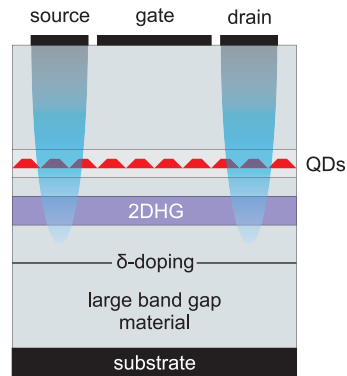


**Figure 4.1.:** Schematic cross-section of a QD-Flash cell. The source and drain contacts are connected via annealing to the two-dimensional hole gas, which is populated by the holes released by the underlying  $\delta$ -doping. The quantum dot layer is placed above the two-dimensional hole gas. The semiconductor making up the bulk of the structure must have a larger band gap than the one making up the quantum dots. (After [12, 13]).

or MBE reactor (see Sc. 2.1). Finally, thanks to the wide range of possible lattice mismatches and resulting strain patterns, III-V heterostructures are the ideal materials for the fabrication of self-organised quantum dots.

Self-organised quantum dots present the advantage over conventional floating-gate storage that the localisation effect is due to their very electronic structure, thereby removing the need for an additional barrier to trap the charge carriers. As mentioned in Sc. 1.3, the presence of the  $\text{SiO}_2$  barrier in conventional Flash is the reason for its long write/erase times and reduced durability. QD-Flash memory manages to decouple write and erase times through the use of quantum dots, because two very different physical processes underlie the two operations (see Sc. 3.1 and Sc. 3.3). Furthermore, the storage time is also completely decoupled from the write time, and its coupling with the erase time is weaker than in conventional Flash, where all three times (write, erase, and storage) are coupled. Another important aspect is the fact that quantum dots are fabricated in a self-organised fashion, which generates interfaces of a higher quality because the accumulated strain is released through island formation instead of through the formation of defects and dislocations (see Sc. 2.4.1).

Self-organised quantum dots also enable the use of holes instead of electrons for storage. Holes have the distinct advantage of having a much larger effective mass than electrons [6], which leads to longer storage times for the same localisation energy (compare Eq. 3.15 and Eq. 3.16). For this reason QD-Flash uses preferably type-II quantum dots which localise only holes, so that the entirety of the band gap mismatch can be exploited.

Finally, the use of a MODFET structure allows for the completely electrical operation of QD-Flash: The charge state of the quantum dots can be controlled via the gate voltage and read through the 2DHG.

## 4.1. Storage

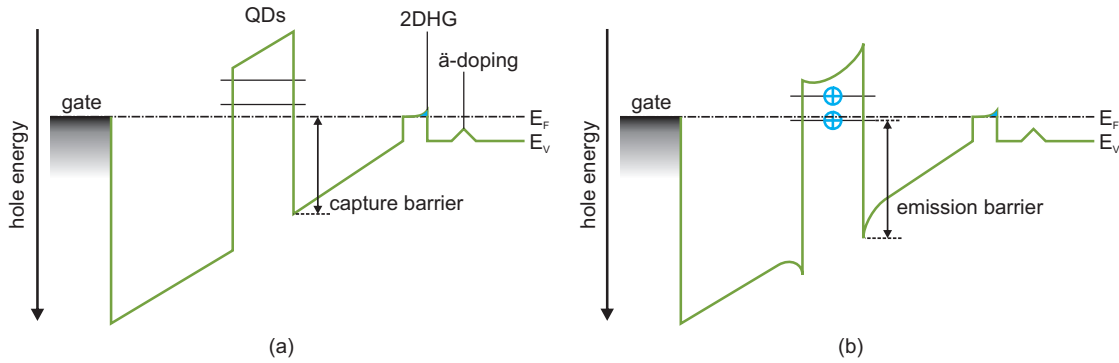


**Figure 4.2.:** Schematic depiction of the valence band in a QD-Flash cell while storing (a) the logic “0” (unoccupied QDs) and (b) the logic “1” (occupied QDs). The capture and emission barriers are marked.

The storage configuration is defined by the absence of an applied voltage, since a non-volatile memory is characterised by its ability to retain information without an external power supply. In QD-Flash the logic “0” and the logic “1” are represented by the hole occupancy number of the quantum dots. Naturally, the maximum degree of distinguishability is achieved if “0” is represented by fully unoccupied quantum dots and “1” by fully occupied quantum dots. This condition optimises the read-out process because the relative difference in conductivity of the 2DHG in the two states is maximised, thereby minimising the sensitivity required for its measurement.

The valence band configuration of a QD-Flash cell storing a “0” is sketched in Fig. 4.2a. The Fermi level is pinned by the  $\delta$ -doping, so that the 2DHG is always partially populated by holes. Since the energy difference at the metal-semiconductor interface is fixed [6], the valence band must bend continuously between said interface and the 2DHG, forming a depletion layer. The bending forms a triangular barrier preventing holes from being captured into the quantum dots (right-hand side of Fig. 4.2a), thus forming the *capture barrier*.

The valence band configuration of a QD-Flash cell storing a “1” is sketched in Fig. 4.2b. In this case the quantum dots are occupied by holes, leading to a small deformation

#### 4. QD-Flash

of the valence band in their vicinity and to a small shift in the energies of the bound states (see Sc. 3.3.1). The emission of holes from the quantum dots is hindered by the localisation of the quantum dots themselves. The *emission barrier* is thus formed by the difference between the valence band edge next to the quantum dots and the Fermi level.

It is worth noting that, by the very definition of charge-storage memory, storage takes place *out of equilibrium*. If this wasn't the case, the storage time would always be infinite. Once the desired state ("0" or "1") is prepared, the quantum dot ensemble will return to its equilibrium occupancy following an exponential decay with the storage time as a time-constant. The equilibrium occupancy of the ensemble depends on the energy of the bound states relative to the Fermi level. For example, the quantum dots in Fig. 4.2a would be *always occupied* at equilibrium. From Fig. 4.2a it is also clear that, as far as the storage time is concerned, the quantum dots should be placed as close as possible to the gate contact, so that all of their bound states lie well below the Fermi level. In this case the equilibrium occupation of the quantum dots is 0, so that the storage time of the logic "0" is indeed virtually infinite, and the storage time of the logic "1" is maximised because the entirety of the localisation energy contributes to the emission barrier. The localisation energy will then represent exactly the emission barrier.

The storage time for holes in self-organised quantum dots has been investigated for several material combinations [14, 126–128]. The record figure at the beginning of this work was 1.6 s at room temperature for InAs/GaAs QDs with an additional Al<sub>0.9</sub>Ga<sub>0.1</sub>As barrier [14].

### 4.2. Write operation

The write operation (writing the logic "1") is accomplished in QD-Flash by applying a positive bias to the gate, which shifts the (quasi-)Fermi level of the gate contact towards higher energies, bringing the valence band into flatband configuration (Fig. 4.3). The capture barrier is thereby removed and the holes can be thermally captured into the quantum dots.<sup>1</sup>

Self-organised quantum dots typically present capture cross-sections of the order of  $10^{-9}$ – $10^{-15}$  cm<sup>2</sup>, orders of magnitude larger than that of the typical deep trap [129, 130]. As a result, thermal capture of charge carriers is extremely fast, taking place in times of the order of picoseconds or tenths of picoseconds [8, 9]. The shortest write time

---

<sup>1</sup>In Fig. 4.3 the holes are captured directly from the valence band. In reality they are usually captured from the 2DHG, the localisation energy of which is of the order of  $k_B T$  at room temperature. This process depletes the 2DHG, contributing to its decrease in conductivity when the quantum dots are occupied.

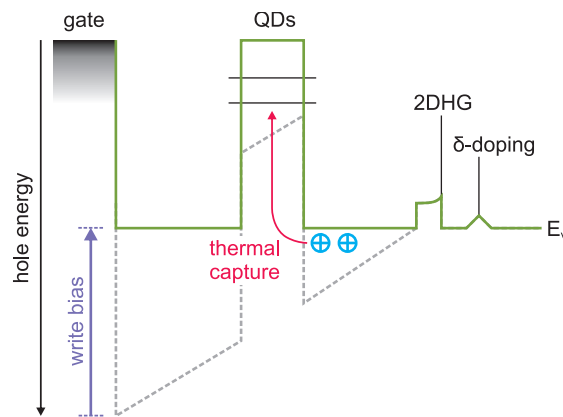


**Figure 4.3.:** Schematic depiction of the valence band in a QD-Flash cell while writing the logic “1”. A positive bias is applied to the gate in order to bring the valence band into flatband configuration and allow thermal capture of holes into the QDs.

demonstrated in QD-Flash is 6 ns [15], in the same order of magnitude of the write time of DRAM (10 ns). Shorter write times could not be achieved because of the parasitic RC low-pass filter created by the gate contact. Reducing the surface area of the gate contact would reduce its capacitance and enable the measurement of faster write times.

The decisive advantage of QD-Flash over conventional Flash memory lies in the write operation. The emission barrier in conventional Flash is given by the Si/SiO<sub>2</sub> band discontinuity, which cannot be modified by the external voltage without destroying the cell. Flash must then make use of slower processes (Fowler-Nordheim tunnelling and hot-electron injection) in order to write information. On the other hand, the capture barrier in QD-Flash can be controlled electrically, enabling its complete removal at an appropriate write voltage. As a consequence, the write process can take advantage of the extremely fast thermal capture process and the write time is completely decoupled from the storage time.

### 4.3. Erase operation

As sketched in Fig. 4.4, the erase operation (writing the logic “0”) is accomplished in QD-Flash by applying a negative bias to the gate. The valence band is then bent further, so that the triangular barrier adjacent to the quantum dots becomes thinner, and the holes can efficiently tunnel out of the quantum dots and into the valence band. As opposed to the write operation, the erase operation does not involve completely cancelling the emission barrier. As a consequence, the erase time is not completely decoupled from the storage

#### 4. QD-Flash

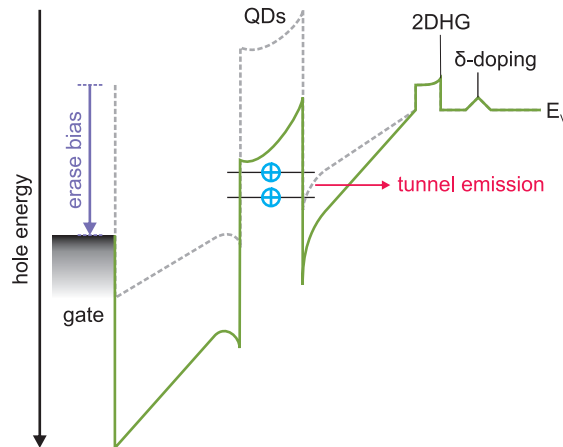


**Figure 4.4.:** Schematic depiction of the valence band in a QD-Flash cell while erasing (i.e. writing the logic “0”). A negative bias is applied to the gate in order to reduce the thickness of the emission barrier. The holes can then tunnel through it.

time, since longer storage times (i.e. higher localisation energies) also imply thicker emission barriers to cross (and therefore longer erase times). However, the coupling is of a very different nature from the one of conventional Flash memory because the properties of the emission barrier can be finely tuned through band engineering. For example, the erase time can be improved by implementing a *resonant tunnelling structure*, i.e. an array of quantum wells between the quantum dots and the 2DHG which would form a superlattice and therefore increase the transparency of the barrier.

The fastest erase time demonstrated in QD-Flash is 44 ns [37], again in the same order of magnitude of DRAM.

#### 4.4. Read-out

The read-out operation is performed through a conductivity measurement on the source-drain contacts. As discussed in Sc. 2.3, the presence of fixed charges in the vicinity of a two-dimensional carrier gas disrupts its conductivity. Whereas this phenomenon is undesirable in the fabrication of a traditional field-effect transistor, it is exploited in QD-Flash in order to read the charge state of the quantum dots. When the quantum dots are occupied, the holes localised in them lower the mobility of the 2DHG [64, 131] and reduce its charge-carrier density by field effect [27, 132, 133]. As a consequence, the conductivity of the 2DHG is reduced and the charge state can be detected by measuring it. The conductivity of the channel can be measured by applying a voltage on the source and

#### *4.4. Read-out*

drain contacts and measuring the current flowing through them, making the read-out operation very simple and efficient.

### Summary

- QD-Flash is a novel memory architecture based on III–V semiconductors. Information is stored as holes in self-organised quantum dots. The quantum dots are embedded in a MODFET, so that their charge state can be inferred from the conductivity of the channel.
- In the storage configuration, the localisation energy of the quantum dots provides the emission barrier, whereas the bending of the valence band provides the capture barrier.
- The write operation is performed by applying a positive voltage to the gate so that holes can be thermally captured into the quantum dots.
- The erase operation is performed by applying a negative voltage to the gate so that the emission barrier becomes thin and the holes can tunnel out of the quantum dots.
- Prior research at TU Berlin lead to the following results before the beginning of this thesis:
  - A fully-functional demonstrator was fabricated in order to prove the feasibility of QD-Flash. Read and write times of the order of DRAM were achieved.
  - Erase times of the order of DRAM could only be demonstrated for low localisation energies. However, the erase operation can be optimised by implementing an array of quantum wells between the quantum dots and the 2DHG. The array would form a superlattice, enabling the selective increase of the transparency for specific gate voltages.
  - The longest storage time at room temperature demonstrated in QD-Flash was 1.6 s for InAs/GaAs QDs with an additional  $\text{Al}_{0.9}\text{Ga}_{0.1}\text{As}$  barrier.

## 5. Experimental Techniques

Machines take me by surprise with  
great frequency.

---

(Alan Turing)

In this work, charge carrier dynamics is investigated through capacitance spectroscopy, which is the focus of the present chapter. Before describing the experimental techniques employed in this work, we will discuss the properties of the depletion layer in a p–n junction, with special focus on its capacitance. We will then introduce the static capacitance spectroscopy measurement and the influence that quantum dots can have on it. Finally, we will come to time-resolved capacitance spectroscopy, analysing in particular deep-level transient spectroscopy (DLTS), both in its original form proposed by Lang in 1974 [134], and in the charge-selective mode developed at TU Berlin by Geller [120].

### 5.1. The p–n junction

P–n junctions represent the simplest semiconductor device, namely the diode. They are formed by doping contiguous portions of a semiconducting material in opposite ways: One side is n-doped, i.e. it contains doping atoms that *release* electrons when ionised (*donors*); the other side is p-doped, i.e. it contains doping atoms that *capture* electrons when ionised (*acceptors*). In the hole picture, acceptors can be equivalently seen as “releasing holes” when ionised. In a doped semiconductor, one speaks of *majority* and *minority* charge carriers. The majority charge carriers of an n-doped semiconductor are electrons; of a p-doped semiconductor holes.

#### 5.1.1. Depletion layer

In the following we will consider an abrupt junction between a homogeneously p-doped semiconductor and a homogeneously n-doped semiconductor. The discussion follows Sze et al. [6].

## 5. Experimental Techniques

Before the semiconductors are brought into contact, their Fermi levels  $E_F$  will be different. After contact is created, electrons will start flowing from the n-side to the p-side, thereby bringing the Fermi levels to the same energy. The electrons will recombine with the ionised acceptors in the region closest to the junction on the p-side, leaving behind ionised donors on the n-side, until the electric field created by the fixed charges creates a drift current able to compensate the flow of electrons (see Fig. 5.1). This process bends the conduction band and the valence band by the amount  $qV_{bi}$ , where  $V_{bi}$  is the *built-in voltage*. The built-in voltage equals the difference between the initial Fermi level of the n-side and that of the p-side divided by the elementary charge:  $qV_{bi} = E_F^n - E_F^p$ . Only fixed charges (the ionised atoms) are present in the region where the bands are bent, without any free charge carriers. This region is therefore called *depletion layer* or *space-charge region*. We assume here that the concentration of the fixed charges can be expressed as a square function (*Schottky approximation*), which means that the concentration of free charge carriers falls abruptly from its bulk value to 0 at the edge of the depletion layer. In reality, the concentration of free charge carriers decays exponentially at the edge of the depletion layer over a length negligible with respect to the width of the depletion layer, making the Schottky approximation a good approximation.

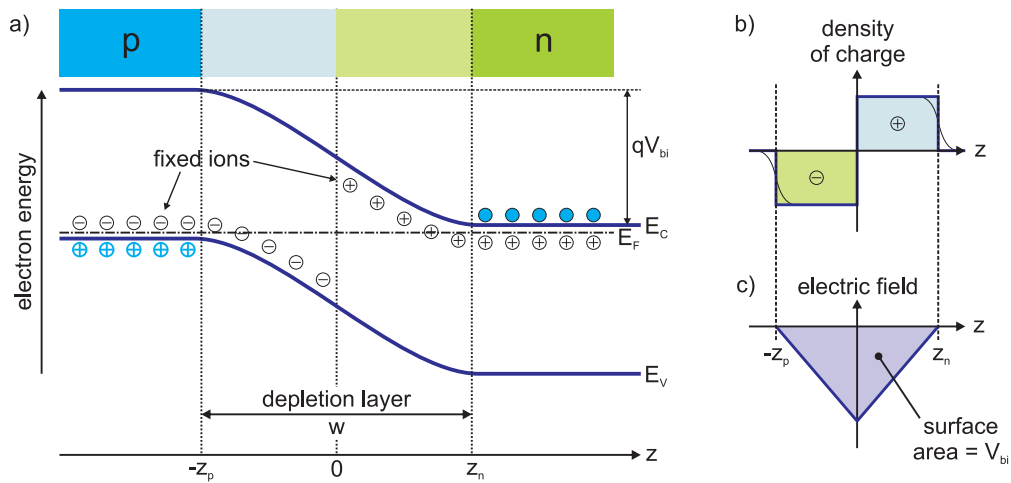


**Figure 5.1.:** (a) Schematic representation of the band structure in the depletion region of a (symmetric) p–n junction located at  $z = 0$ . The depletion region extends to  $-z_p$  into the p layer and to  $z_n$  into the n layer. At equilibrium (i.e. when the Fermi level  $E_F$  is uniform) the built-in potential  $V_{bi}$  is formed across the junction. Free charge carriers are depicted in blue, fixed ions in black. (b) Schottky approximation of the density of charge. The thin black line is an exaggerated representation of the actual density of charge, which follows the Fermi distribution. (c) Electric field in the depletion region. The area below the curve equals the built-in potential  $V_{bi}$ . (After [6]).

## 5.1. The p–n junction

If no external voltage is applied to the junction, the potential difference between the two sides generated by the fixed charges is the *built-in voltage* [6]:

$$V_{bi} = \frac{k_B T}{q} \ln \left( \frac{N_A N_D}{n_i^2} \right), \quad (5.1)$$

where  $N_A$  is the number of acceptors on the p-side,  $N_D$  the number of donors on the n-side, and  $n_i$  the intrinsic carrier concentration. For the GaP samples used in this work (typically  $N_A = 2 \times 10^{16} \text{ cm}^{-2}$ ;  $N_D = 1 \times 10^{18} \text{ cm}^{-2}$ ),  $V_{bi} \simeq 2.04 \text{ V}$  at room temperature ( $T = 300 \text{ K}$ ). The length of the depletion layer is:

$$w = \sqrt{\frac{2\varepsilon_r \varepsilon_0 V_{bi}}{q} \cdot \frac{N_A + N_D}{N_A N_D}}. \quad (5.2)$$

The built-in potential causes the rectifying behaviour of the p–n junction. If an external voltage is applied with a polarity that compensates the built-in potential (i.e. with the positive pole on the p-side), the width of the depletion layer can be reduced until it disappears and electrons can flow unhindered. This configuration is called *forward bias*. In the opposite case (*reverse bias*) only a small current is able to flow because the external voltage and the built-in potential add up, extending the width of the depletion layer. Eq. 5.2 has to be modified to account for the external voltage  $V_{ext}$ :

$$w = \sqrt{\frac{2\varepsilon_r \varepsilon_0 (V_{bi} - V_{ext})}{q} \cdot \frac{N_A + N_D}{N_A N_D}}. \quad (5.3)$$

In the samples used in this work, the doping on the n-side is always several orders of magnitude larger than the doping on the p-side. Such junctions are often referred to as *n–p<sup>+</sup> junctions* if  $N_A \gg N_D$ , and *p–n<sup>+</sup> junctions* if  $N_D \gg N_A$ . In this case Eq. 5.3 can be approximated with:

$$w = \sqrt{\frac{2\varepsilon_r \varepsilon_0 (V_{bi} - V_{ext})}{q N_B}}, \quad (5.4)$$

where  $N_B$  is the doping concentration of the side with the lower doping.

### 5.1.2. Capacitance of a p–n junction

The fixed charges in the depletion layer form spatially-separated positive and negative charges. The separation of charges gives rise to a capacitance. Since the width of the depletion layer (and hence the separation of the charges) depends on the applied voltage,

## 5. Experimental Techniques

the expression for the differential capacitance per unit area  $C = dQ/dV$  has to be used. Using the differential expressions of the electric field  $dE = dQ/\varepsilon_r\varepsilon_0$  and of the potential  $dV = wdE$  (where  $w$  is again the width of the depletion layer) we have:

$$C = \frac{dQ}{dV} = \frac{dQ}{q \frac{dQ}{\varepsilon_r\varepsilon_0}} = \frac{\varepsilon_r\varepsilon_0}{w}. \quad (5.5)$$

The total capacitance of the junction equals the capacitance per unit area (Eq. 5.5) times the surface area of the section of the junction  $A$ :

$$C = \frac{\varepsilon_r\varepsilon_0 A}{w}, \quad (5.6)$$

which is the familiar expression for the capacitance of a parallel plate capacitor. The capacitance of a p–n junction equals in other words that of a parallel plate capacitor where the surface area is the same as the section of the junction and the distance between the plates is the width of the depletion layer. The expression for the capacitance of a p–n junction can then be obtained by plugging Eq. 5.3 into Eq. 5.6:

$$C = A \cdot \sqrt{\frac{\varepsilon_r\varepsilon_0 q}{2(V_{bi} - V_{ext})} \cdot \frac{N_A N_D}{N_A + N_D}}. \quad (5.7)$$

As with the width of the depletion layer, if the doping is much higher on one side than on the other Eq. 5.7 can be approximated with:

$$C = A \cdot \sqrt{\frac{\varepsilon_r\varepsilon_0 q N_B}{2(V_{bi} - V_{ext})}}, \quad (5.8)$$

where  $N_B$  is the doping concentration of the side of lower doping.

### 5.2. Static capacitance spectroscopy

Capacitance–voltage profiling (C–V profiling) is a static capacitance spectroscopy method commonly used to determine the doping density of semiconductors [6, 111, 135]. In the Schottky approximation, the charge carrier fluctuation under variation of the external bias takes place exclusively at the edge of the depletion layer. If the doping on one side of the junction is much higher than on the other, the depletion layer will extend almost only into the side of lower doping. If we assume that the doping density equals the density of

ionised doping atoms,<sup>1</sup> Eq. 5.8 can then be used to determine the doping density of the lowly-doped side. The inverse square of the capacitance is namely:

$$\frac{1}{C(V_{ext})^2} = \frac{2(V_{bi} - V_{ext})}{q\varepsilon_r\varepsilon_0 A^2 N_B} = \frac{2V_{bi}}{q\varepsilon_r\varepsilon_0 A^2 N_B} - \frac{2}{q\varepsilon_r\varepsilon_0 A^2 N_B} V_{ext}, \quad (5.9)$$

so that if the doping density  $N_B$  is constant, the plot of  $1/C^2$  over  $V_{ext}$  is a line. The doping density can then be extracted from its slope and the built-in voltage from the intercept with the  $y$ -axis.

If the doping density is not constant in space, the expression for  $N_B$  has to be derived through differentiation. The “slope” is then represented by the first derivative of  $1/C^2$  and the doping density becomes:

$$N_B(z) = \frac{1}{A^2 \varepsilon_r \varepsilon_0 q} \left[ \frac{1}{\frac{d}{dV_{ext}} \left( \frac{1}{C^2} \right)} \right], \quad (5.10)$$

where  $z$  is the distance from the junction surface into the semiconductor of lower doping and has to be derived experimentally from Eq. 5.4 ( $z = w$ ). The measurement of the capacitance as a function of the applied voltage can therefore be used to determine the doping profile of the low-doping side of the junction.

### 5.2.1. Effect of quantum dots

If quantum dots are embedded in a p–n junction, the charge distribution is different than assumed above because localised charge carriers can locally compensate the space charge provided by the ionised dopants. As a consequence the width of the depletion layer increases and the capacitance of the junction is lowered.

Let us assume that the quantum dots are embedded in the p-side of an  $n^+ - p$  junction and that they are able to localise holes. As sketched in Fig. 5.2a, the charge stored in the quantum dots is modelled as a layer of uniform surface charge placed at  $z = -z_{QD}$ . The depletion layer extends from  $-z_p$  on the p-side to  $z_n$  on the n-side, with  $z = 0$  representing the junction surface. We are here concerned with the static case, so that we can consider the storage time of the quantum dots infinite. When writing Poisson’s equation we have to take into account the charge stored in the quantum dots:

$$-\frac{d^2\varphi(z)}{dz^2} = \frac{dE}{dz} = \frac{\rho(z)}{\varepsilon_r \varepsilon_0}, \quad (5.11)$$

<sup>1</sup>This is equivalent to assuming that all doping atoms are ionised, which is very reasonable, at least at room temperature.

## 5. Experimental Techniques

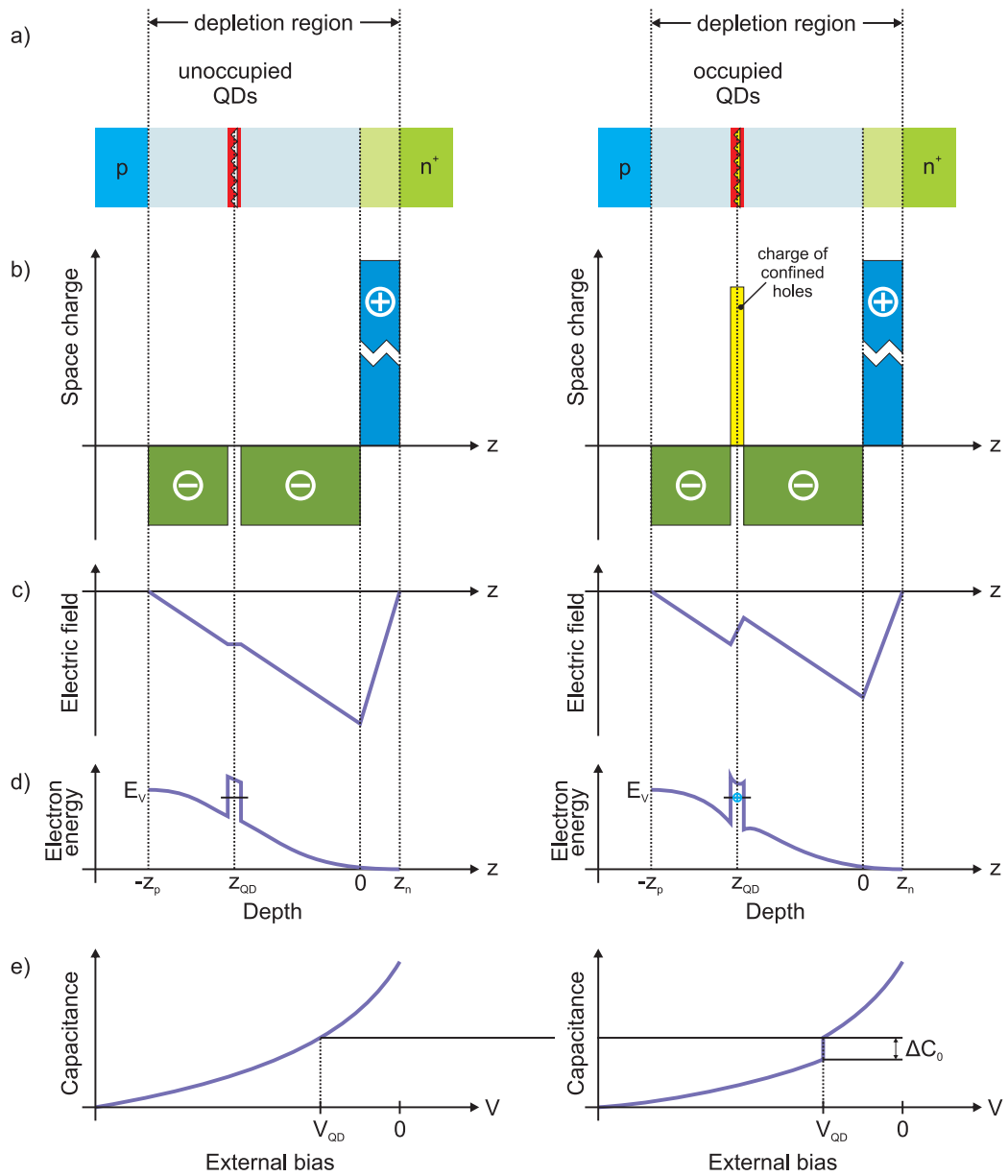


**Figure 5.2.:** Effect of the localisation of holes in QDs embedded in a  $p$ - $n^+$  junction (the storage time of the QDs is here assumed infinite). The left-hand side refers to the case of unoccupied QDs, the right-hand side to the case of occupied QDs. (a) Sketch of the  $p$ - $n^+$  junction ( $p$  layer in blue,  $n$  layer in green), (b) charge distribution inside the junction (negative ions: green, positive ions: blue, confined holes: yellow), (c) electric field, (d) valence band in the vicinity of the QD layer, and (e) capacitance of the junction. The capacitance profile is undisturbed by the presence of unoccupied QDs (left-hand side). If the QDs are occupied, however, the capacitance is shifted down by an amount  $\Delta C_0$  once the edge of the depletion layer crosses the QD layer because the localised holes effectively shield part of the charge of the fixed ions. (Adapted from [124]).

with the charge density given by:

$$\rho(z) = \begin{cases} -qN_A & \text{for } z \neq -z_{QD} \\ qN_{QD}n_h & \text{for } z = -z_{QD} \end{cases}. \quad (5.12)$$

$N_{QD}$  represents here the density of quantum dots and  $n_h$  the number of holes per quantum dot. The solution of Eq. 5.11 yields the width of the depletion layer:

$$z_p = w_{QD} = \sqrt{\frac{2}{qN_B}[\varepsilon_r\varepsilon_0(V_{bi} - V_{ext}) + qN_{QD}n_h z_{QD}]}. \quad (5.13)$$

The modification of the depletion layer width reflects onto its capacitance:

$$C_{QD} = \varepsilon_r\varepsilon_0A \cdot \sqrt{\frac{qN_B}{2[\varepsilon_r\varepsilon_0(V_{bi} - V_{ext}) + qN_{QD}n_h z_{QD}]}}. \quad (5.14)$$

Dividing Eq. 5.8 by Eq. 5.14 yields the relative variation in capacitance due to the quantum dots:

$$\Delta C = \frac{C}{C_{QD}} = \varepsilon_0\varepsilon_r \cdot \sqrt{1 + \frac{qN_{QD}n_h z_{QD}}{\varepsilon_0\varepsilon_r(V_{bi} - V_{ext})}}. \quad (5.15)$$

The effect of quantum dots is illustrated graphically in Fig. 5.2, where the left-hand side refers to non-occupied QDs and the right-hand side to occupied QDs. As mentioned above, the holes in the QDs partially compensate the negative ions in the depletion layer, which in turn has to extend further in order to maintain electric neutrality against the positive ions on the n-side (Fig. 5.2b). The electric field in the vicinity of the QDs is thus reversed (Fig. 5.2c) and the capacitance will be lower for occupied QDs than for unoccupied QDs (Fig. 5.2e).

The presence of QDs in a p–n junction can often be detected via a hysteresis measurement. In this case, however, the finite storage time of real QDs has to be taken into account.

The capacitance of a simple p–n diode (i.e without QDs) is sketched as a dashed red line in Fig. 5.3. If the voltage sweep is conducted starting from 0 V towards higher reverse biases, the QDs will be initially occupied as they are outside the depletion layer ( $z_p < z_{QD}$ ). At this stage, the QDs do not influence the capacitance, which therefore equals that of a simple p–n diode (i.e.  $\sim \sqrt{1/V}$ , see Eq. 5.8), marked by a dashed red line in Fig. 5.3. When the edge of the depletion layer reaches the vicinity of the QDs, the holes stored in them will partially balance the charged of the negative ions in the depletion layer, thereby increasing its length and lowering the capacitance. The capacitance curve

## 5. Experimental Techniques

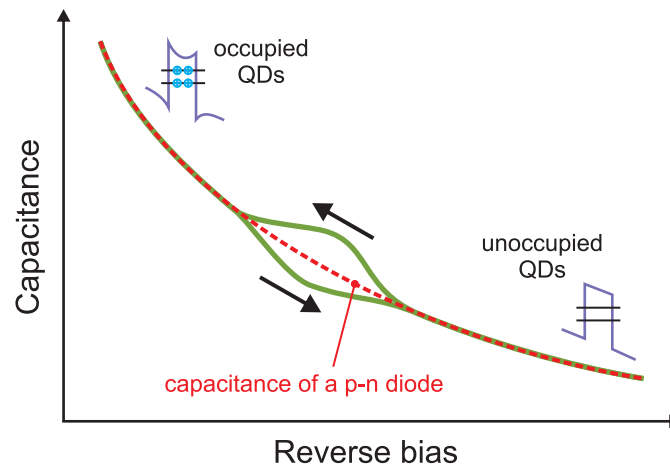


**Figure 5.3.:** Hysteresis in the  $C$ - $V$  curve. In the downward sweep the QDs are initially charged, lowering the capacitance until the holes are emitted. In the upward sweep the QDs are initially unoccupied, increasing the capacitance until holes are captured.

will then be the lower one in Fig. 5.3. Once the reverse bias is high enough, the holes are emitted and the capacitance equals again that of a simple p-n diode (right-hand side of Fig. 5.3). Conversely, during the upward sweep the capacitance will be increased until holes are captured into the QDs (lower curve in Fig. 5.3). A hysteresis opening is then formed of a magnitude proportional to the QD density and to the distance of the QD layer from the junction surface.

The (finite) storage time of the QDs comes into play because the capacitance measurement is performed by recording the response of the system to an AC voltage superimposed to the DC voltage that determines the width of the depletion layer.<sup>2</sup> As a consequence, holes are captured and emitted several times during the collection of each data point. If the frequency of the AC signal is too high, the QDs will not have time to go through a complete cycle of capture and emission during one oscillation of the signal and their effect on the capacitance will be averaged out of the measurement. Therefore, the hysteresis opening becomes wider as the measurement frequency approaches the capture/emission rate at the measurement temperature.

<sup>2</sup>The DC voltage is in other words what is reported on the  $x$ -axis in Fig. 5.3.

### 5.3. Time-resolved capacitance spectroscopy

Eq. 5.15 states that the variation in capacitance due to the presence of quantum dots in a p–n junction is proportional to their occupation  $n_h$ . As mentioned above, the occupation of real QDs may vary in time:  $n_h = n_h(t)$ . As a consequence Eq. 5.15 has to be rewritten:

$$\Delta C(t) = \frac{C}{C_{QD}(t)} = \varepsilon_0 \varepsilon_r \cdot \sqrt{1 + \frac{qN_{QD}n_h(t)z_{QD}}{\varepsilon_0 \varepsilon_r (V_{bi} - V_{ext})}}. \quad (5.16)$$

A time-resolved measurement of the capacitance under variation of the external bias can then be used to obtain information on the capture and emission dynamics of charge carriers in quantum dots.

Deep Level Transient Spectroscopy (DLTS) [119, 134, 136, 137] was developed by Lang in 1974 for the determination of activation energy and capture cross-section of deep levels in semiconductors [111]. It is based on the time-resolved measurement of the capacitance of a p–n junction under varying bias voltages and temperatures. Since it has been demonstrated experimentally that the physics of deep levels also applies to QDs [15, 114–116], DLTS can also be used to study the internal levels of quantum dots [14, 93, 113, 138–142].

#### 5.3.1. The DLTS sample

Since DLTS is a purely capacitive measurement, a simplified sample can be used instead of the complete QD-Flash cell depicted in Fig. 4.1. The DLTS sample is sketched in Fig. 5.4 in two completely equivalent versions which differ only for a minor processing step. Fig. 5.4a represents the result of a three-step processing (three optical lithographies, two metallisations, and one etching step) where both the top and back contacts are placed on the top side of the sample. This has the advantage that the doping of the substrate is irrelevant for the functioning of the structure. Fig. 5.4b represents the result of a simplified processing (one optical lithography and two metallisations) where the back contact is placed on the bottom side of the sample. The advantage of this method is that the processing can be performed in one day instead of the three days involved in the other method. However, this processing is only applicable to samples grown on a highly p-doped substrate. Further details on processing are provided in App. C.

The sample itself consists of a p–n<sup>+</sup> junction with a quantum dot layer embedded in the p layer. The quantum dots are embedded in the p layer in order to study the dynamics of holes; a symmetrical structure can be used to study the dynamics of electrons. A p<sup>+</sup> layer

## 5. Experimental Techniques

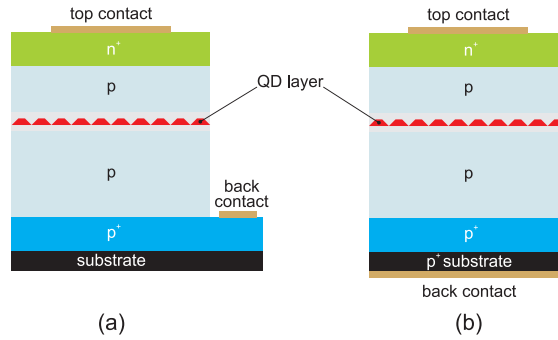


**Figure 5.4.:** Schematic representation of the structure of a DLTS sample, i.e. a  $p$ - $n^+$  junction with QDs embedded in the  $p$  layer. A  $p^+$  layer is grown first to facilitate the formation of Ohmic contacts. (a) Result of the standard three-step processing, necessary if the substrate is not  $p$ -doped. (b) Result of the simplified two-step processing, where the back contact is deposited directly on the substrate from the bottom.

is placed below the  $p$  layer to ensure that the contact is Ohmic.

Unless otherwise specified, all of the following refers to the DLTS sample.

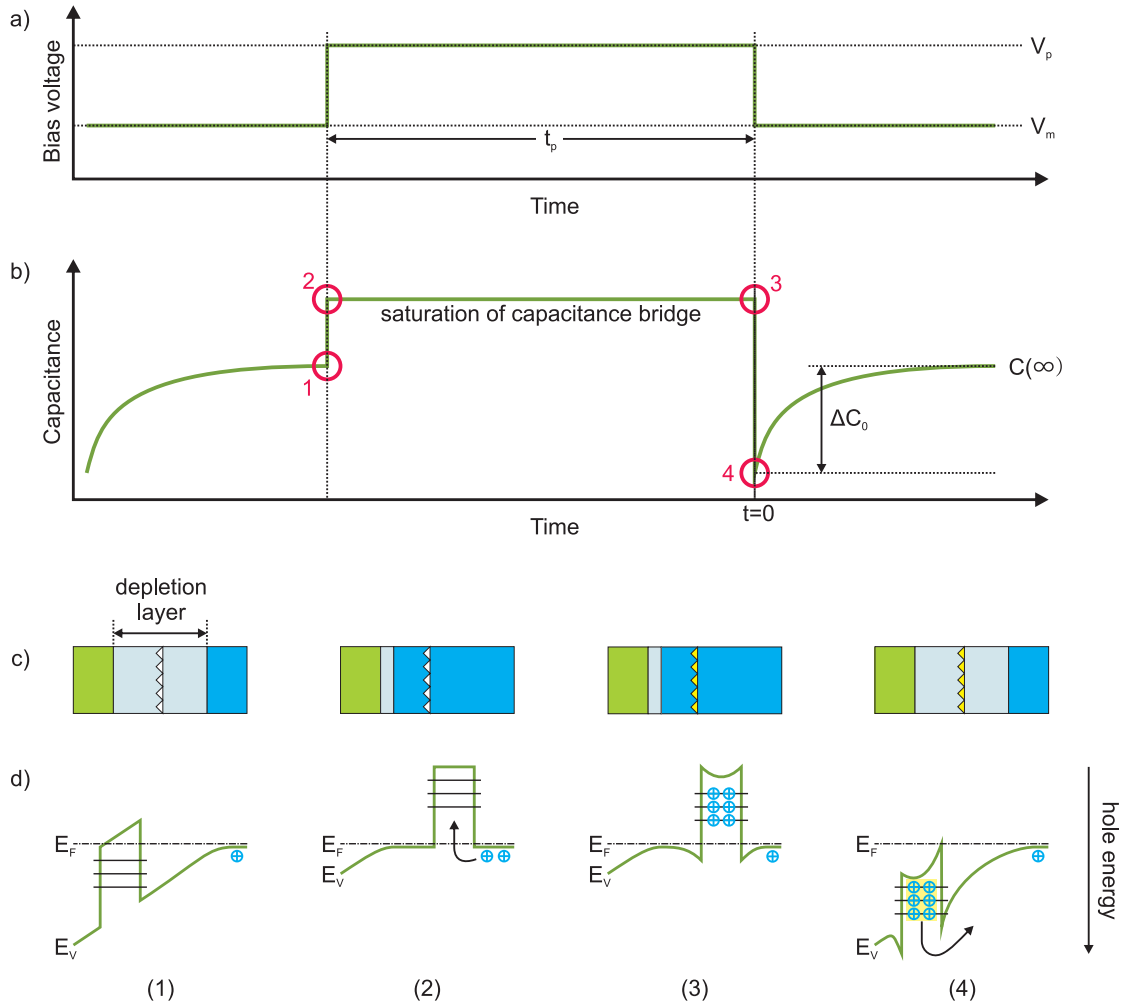
### 5.3.2. Measurement protocol

Fig. 5.5 summarizes the work cycle of a DLTS measurement. A DLTS measurement takes place in four steps (marked in Fig. 5.5 with the numbers 1 to 4). The measurement starts with the applied voltage  $V_{ext}$  set to  $V_m$  (measurement voltage).  $V_m$  is chosen so that at that voltage the quantum dot layer is inside the depletion layer (Fig. 5.5c-1). The quantum dots are therefore completely unoccupied (Fig. 5.5d-1).  $V_{ext}$  is then increased to the pulse voltage  $V_p$ , which is chosen so that the quantum dot layer is outside the depletion layer (Fig. 5.5c-2). As a consequence the capacitance of the junction increases because of the shortening of the depletion layer (Fig. 5.5b). Moreover, holes are thermally captured into the quantum dots (Fig. 5.5d-2) until all internal states up to the Fermi level are occupied. As soon as the quantum dots are completely occupied (Fig. 5.5d-3), the applied voltage can be switched back to  $V_m$ . The capacitance is now lower than during step 1 because of the charge carriers trapped in the quantum dots. Since the quantum dot layer is again outside the depletion layer (Fig. 5.5c-4), holes are emitted from the quantum dots (Fig. 5.5d-4) and their emission causes the capacitance to rise to the equilibrium capacitance  $C(\infty)$ . According to Eq. 5.16, the capacitance transient is a monoexponential decay of time constant  $\tau$ , and its amplitude  $\Delta C_0$  is proportional to the number of charge carriers involved. The capacitance transient can thus be expressed as

[111]:

$$C(t) = C(\infty) - \Delta C_0 \exp\left(-\frac{t}{\tau}\right). \quad (5.17)$$

Now the emission rate for holes  $e_p$  is defined as the reciprocal of the characteristic time  $\tau$ :  $e_p = 1/\tau$ . Once  $\tau$  is extracted from the capacitance transient, it can be used to determine the activation energy and the capture cross-section of the system, as discussed in Sc. 3.4.



**Figure 5.5.:** (a) Applied voltage, (b) capacitance, (c) sketch of the depletion layer, and (d) valence band over the course of one DLTS cycle. The cycle starts off at the measurement voltage  $V_m$ , where the QDs are empty (1). The QDs are then filled at the pulse voltage  $V_p$  (2). Once they are occupied (3), the voltage is switched back to  $V_m$  (4) and the emission transient is observed.

The signal-to-noise ratio (SNR) is usually enhanced by repeating the measurement several times (10–30) and averaging the resulting transients.

## 5. Experimental Techniques

It is worth noting that the actual behaviour of the capacitance during the charge pulse is not the one depicted in Fig. 5.5b. Just as the capacitance increases exponentially during the emission phase, it must decrease exponentially during the capture phase. Indeed, the capacitance at step 2 is higher than the capacitance at step 3 because of the lack of holes in the quantum dots which temporarily “masks” the shortening of the depletion layer. However, this capture transient is normally not visible in our measurements because the capacitance bridge is saturated during the charge pulse. This is because the measurement range is chosen small in order to achieve the greatest possible resolution for the emission transient. This choice does not introduce any error in the measurement because the capture transient is not relevant to this work, which focuses on the emission transient.

### 5.3.3. Rate window and double-boxcar method

Eq. 5.17 suggests that  $\tau$  can be determined with a simple exponential fit. Unfortunately, the ensemble broadening, the co-existence of multiple emission paths, and many particle effects introduce other time constants, rendering the emission transient multiexponential [143] and its direct exponential fit impossible. To overcome this issue, the *rate window* (or *boxcar*) *method* was developed. The idea behind the rate window method is that instead of following the logical course of action of choosing a temperature and determining the time constant at that temperature, one chooses a given time constant instead and sweeps through different temperatures in order to find the one where the chosen time constant is realised.

In order to apply the rate window protocol, several transients must be acquired at different temperatures (depicted on the left-hand side of Fig. 5.6). Logically, the transients acquired at lower temperatures will present longer time constants than those acquired at higher temperatures. Two time points  $t_1$  and  $t_2$  are then chosen arbitrarily, defining the rate window  $[t_1, t_2]$ , and the difference in capacitance across the rate window is calculated for each temperature:

$$S(T, t_1, t_2) = C(T, t_2) - C(T, t_1) = \Delta C_0 \left[ \exp\left(-\frac{t_2}{\tau(T)}\right) - \exp\left(-\frac{t_1}{\tau(T)}\right) \right]. \quad (5.18)$$

The resulting curve  $S(T, t_1, t_2)$  is plotted against  $T$  (right-hand side of Fig. 5.6). The maximum of Eq. 5.18 can be obtained by differentiation with respect to  $\tau$  and occurs for:

$$\tau(T) = \frac{t_2 - t_1}{\ln\left(\frac{t_2}{t_1}\right)} \equiv \tau_{\text{ref}}. \quad (5.19)$$

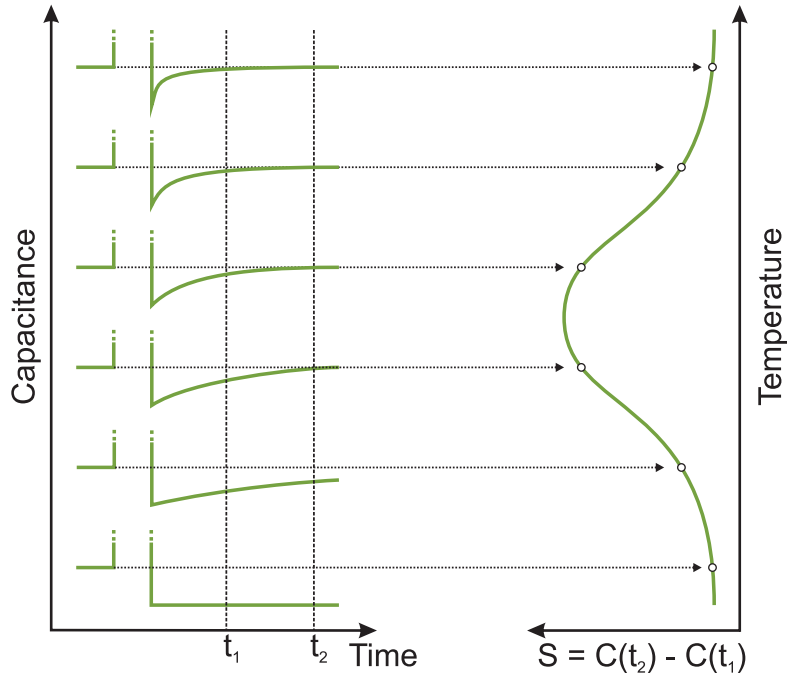


**Figure 5.6.:** Operation principle of the rate window evaluation method. Capacitance transients are acquired at different temperatures (left-hand side) and the difference in capacitance at two set instants  $t_1, t_2$  is plotted against the temperature (right-hand side). The position of the peak reveals the temperature at which the reference time  $\tau_{\text{ref}}(t_1, t_2)$  is the characteristic time of the process.

$\tau_{\text{ref}}$  is the *reference time constant* of the rate window and it represent the time constant of the system for the temperature  $T$  at which the maximum occurs.

The DLTS signal  $S(T, t_1, t_2)$  presents a maximum only if the holes are emitted thermally because tunnelling emission does not depend on temperature and therefore generates a constant DLTS signal [122].

If DLTS is performed on an ensemble of self-organised quantum dots, the DLTS signal will be broadened inhomogeneously, representing the “average” of all thermally activated emission processes involved. We have seen before that the energy levels of an ensemble of self-organised quantum dots are subject to Gaussian broadening (see Sc. 2.4.3). The rate window method yields in this case the time constant of the level at the maximum of the Gaussian [143].

We can now use  $\tau_{\text{ref}} = 1/e_p^{th}$  and Eq. 3.16 to write:

$$\frac{1}{\tau_{\text{ref}}} = \gamma_p T^2 \sigma_p^\infty \exp\left(-\frac{E_a^h}{k_B T}\right). \quad (5.20)$$

## 5. Experimental Techniques

Rearranging Eq. 5.20 and taking the natural logarithm of both sides yields:

$$\ln(\gamma_p \tau_{\text{ref}} T^2) = \frac{E_a^h}{k} \frac{1}{T} - \ln(\sigma_p^\infty), \quad (5.21)$$

which is linear in  $\frac{1}{T}$ . Different  $\tau_{\text{ref}}$  are chosen and the resulting  $\ln(\gamma_p \tau_{\text{ref}} T^2)$  are plotted against  $\frac{1}{T}$ , resulting in the *Arrhenius plot*. The activation energy  $E_a^h$  and the apparent capture cross section  $\sigma_p^\infty$  can then be determined from the slope and  $y$  intercept of the linear fit, respectively.

The signal-to-noise ratio (SNR) can be improved by averaging the value of the transients over an interval  $t_{av}$  around  $t_1$  and  $t_2$  [144]. The method is known as *double-boxcar method* and  $\tau_{\text{ref}}$  is given by:

$$\tau_{\text{ref}} = \frac{t_2 - t_1}{\ln \left( \frac{t_2 + \frac{1}{2} t_{av}}{t_1 + \frac{1}{2} t_{av}} \right)}. \quad (5.22)$$

When using the double-boxcar method, the SNR scales like  $\sqrt{t_{av}}$  [136].

### 5.3.4. Charge selective DLTS

DLTS was originally developed for deep levels in semiconductors, which are characterised by a single bound state. Quantum dots, by contrast, typically present several bound states. When conventional DLTS (i.e. DLTS in its original form, as described above) is applied to quantum dots, the resulting DLTS spectrum is given by the simultaneous emission of charge carriers from all occupied states. The DLTS spectrum is thus broadened and the extracted activation energy represents the mean activation energy of the bound states of the quantum dots.

The internal electronic structure of quantum dots can be investigated in greater detail by means of *charge selective DLTS*, a technique initially developed by Geller [120] and successfully applied to several material systems [14, 113, 145]. The idea behind charge selective DLTS is to choose the measurement voltage  $V_m$  and the pulse voltage  $V_p$  in such a way that only one single state is involved in the measurement. The measurement voltage is then increased and the process repeated until all bound states have been measured.

The valence band in the vicinity of the quantum dots during a typical charge selective DLTS cycle is sketched in Fig. 5.7 (in this example the energy of the second bound state of the quantum dot is measured). It is worth noting that in charge selective DLTS, the quantum dot layer is *always inside the depletion layer*, as opposed to conventional DLTS where the length of the depletion layer is used to determine the occupation of the quantum dots. The initial voltage  $V_m$  is chosen so that for  $V_{\text{ext}} = V_m$  the Fermi level

### 5.3. Time-resolved capacitance spectroscopy

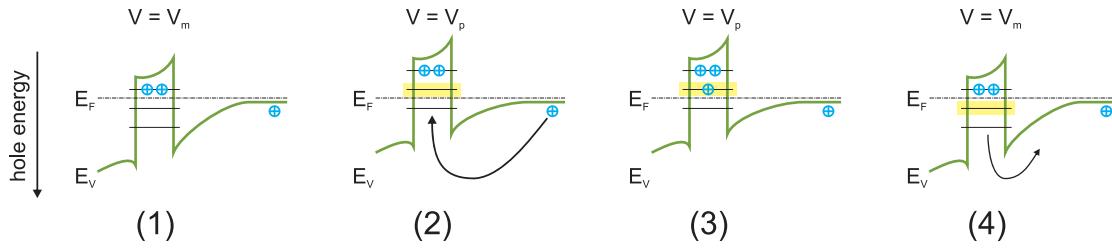


**Figure 5.7.:** Depiction of the valence band during one charge-selective DLTS cycle. The process is analogous to conventional DLTS, except that only one hole per QD is involved.

is positioned between the first and second QD level. The first level is then completely occupied, whereas the second level is completely unoccupied (Fig. 5.7–1). The applied voltage is then pulsed to the voltage  $V_p$ , chosen so that for  $V_{\text{ext}} = V_p$  the Fermi level is positioned between the second and third QD level. Holes will then be captured from the valence band (Fig. 5.7–2) into the second level. On average, one hole is captured per quantum dot (Fig. 5.7–3). The voltage is afterwards returned to the original value  $V_m$ . The second QD level is now again below the Fermi level, which causes the hole to be emitted (Fig. 5.7–4). The generated capacitance transient can be analysed with the double-boxcar method to extract the activation energy and the capture cross-section of the second QD level. The process is then repeated for the other bound states. In particular, the totality of the bound states can be measured by keeping the pulse height  $\Delta V = V_p - V_m$  constant and varying  $V_m$  in steps of amplitude  $\Delta V$ . The resulting set of activation energies and capture cross-sections represent all the hole levels, starting from the ground state up to the last bound state [113]. The activation energy of the ground state is referred to as *localisation energy*. It is the most important characteristic of the quantum dot ensemble because, together with the capture cross-section of the ground state, it determines the localisation time for holes in the quantum dots, and thus the storage time of the memory.

### **Summary**

- The separation of charges across the depletion layer of a p–n junction gives rise to a capacitance. Capacitance–voltage (C–V) profiling can be used to determine the doping profile of the junction.
- If quantum dots are embedded in the junction, they produce a plateau and hysteresis in the C–V curve.
- Deep-level transient spectroscopy (DLTS) is a time-resolved capacitance spectroscopy technique used to determine the activation energy and the capture cross-section of quantum dots.
- Charge-selective DLTS is a technique developed from conventional DLTS in order to study the internal electronic structure of quantum dots. Charge-selective DLTS is used to determine the energy of the ground state of the quantum dots, which is referred to as *localisation energy*  $E_{loc}$ .

## 6. InGaAs QDs in GaP

Man muss etwas Neues machen, um etwas Neues zu sehen.

---

*(Georg Christoph Lichtenberg)*

This chapter will focus on the growth and characterisation of a set of samples containing  $\text{In}_{0.5}\text{Ga}_{0.5}\text{As}$  QDs embedded in GaP, with an additional AIP barrier to increase the storage time. The samples were grown via MOCVD at TU Berlin by G. Stracke and E. Sala. The growth of InGaAs/GaP QDs proved particularly challenging. For this reason, a preliminary set of samples with  $x_{\text{In}} = 25\%$  was grown also at TU Berlin by G. Stracke and A. Glacki. Results concerning  $\text{In}_{0.25}\text{Ga}_{0.75}\text{As}/\text{GaP}$  QDs will be summarised in Section 6.1 to serve as the starting point for the discussion of the results regarding  $\text{In}_{0.5}\text{Ga}_{0.5}\text{As}$  QDs.

Some of these results have already been published in [128, 146, 147].

### 6.1. $\text{In}_{0.25}\text{Ga}_{0.75}\text{As}$ QDs in GaP

The growth of self-assembled InGaAs QDs on GaAs is a well-established technology, and their properties have already been studied extensively [73, 148, 149]. Growing the same dots in GaP is appealing because the much wider band gap of GaP compared to GaAs implies a much larger localisation energy in the dots: The valence band discontinuity of strained InAs in GaP was calculated to 0.93 eV [150], as opposed to 0.25 eV for InAs/GaAs QDs [104]. Moreover, 8-band  $\mathbf{k}\cdot\mathbf{p}$  simulations predict a hole localisation energy of 701 meV for InAs/GaP QDs (see Sc. 2.4.2). However, GaP(001) surfaces present significantly higher formation energies of relevant surface reconstructions than GaAs(001) surfaces [151, 152], thereby inhibiting transition to the three-dimensional Stranski-Krastanow growth mode and QD formation. This problem can be solved — and island formation induced — by depositing a thin GaAs interlayer (IL) on GaP before commencing InGaAs deposition [128].

The epitaxial structure of the samples used is sketched in Fig. 6.1. One QD sample

## 6. InGaAs QDs in GaP

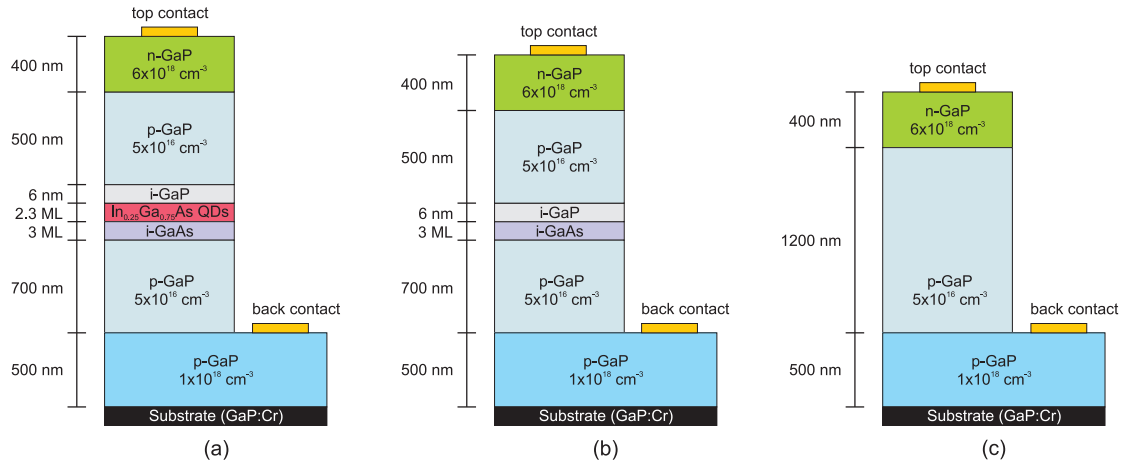


**Figure 6.1:** Epitaxial structures of the  $\text{In}_{0.25}\text{Ga}_{0.75}\text{As}/\text{GaAs}/\text{GaP}$  sample set. (a) QD sample:  $\text{In}_{0.25}\text{Ga}_{0.75}\text{As}$  QDs on a GaAs interlayer embedded in a GaP  $p-n^+$  diode. (b) IL sample: GaAs interlayer embedded in a GaP  $p-n^+$  diode. (c)  $p-n$  sample: GaP  $p-n^+$  diode only.

(Fig. 6.1a) and two reference samples were grown: one containing only the GaAs interlayer but no QDs (Fig. 6.1b), and one containing neither (i.e. a simple  $p-n$  diode; Fig. 6.1c). All samples were grown on semi-insulating GaP(001) substrates (GaP:Cr) using MOCVD. The 500 nm thick  $p^+$ -doped ( $p = 1 \times 10^{18} \text{ cm}^{-3}$ ) GaP contact layer and the 700 nm thick lowly  $p$ -doped ( $p = 5 \times 10^{16} \text{ cm}^{-3}$ ) GaP layer were grown at a substrate temperature of  $750^\circ\text{C}$ . The temperature was then lowered to  $500^\circ\text{C}$  for the growth of GaAs (3 ML<sup>1</sup>) and  $\text{In}_{0.25}\text{Ga}_{0.75}\text{As}$  (2.3 ML). After deposition of the  $\text{In}_{0.25}\text{Ga}_{0.75}\text{As}$  layer, a growth interruption (GRI) of 100 s is applied, followed by the deposition of a 6 nm thick GaP cap layer. Subsequent GaP layers were grown at  $600^\circ\text{C}$ . Zn (for  $p$ ) and Si (for  $n$ ) were used as dopants. A set of identical samples were grown for atomic force microscopy (AFM) measurements, but in this case the growth was stopped right after the 6 nm thick cap layer so that the underlying structure is still accessible via AFM. All samples for DLTS are processed into round mesa structures of diameter  $d = 400 \mu\text{m}$  via standard optical lithography and dry etching methods. For the metallisation process, Ni/AuGe/Au and Ni/Zn/Au are deposited on the  $n$  side and  $p$  side, respectively. See App. C for details on the processing.

An AFM micrograph of the QD sample is shown in Fig. 6.2b. The QDs have a height between 4 nm and 8 nm and a lateral extension of 70 nm to 100 nm with an area density of  $1.2 \times 10^{10} \text{ cm}^{-2}$ , the size of the QDs being overestimated because of the capping

<sup>1</sup>A monolayer (ML) is a one-molecule-thick layer.

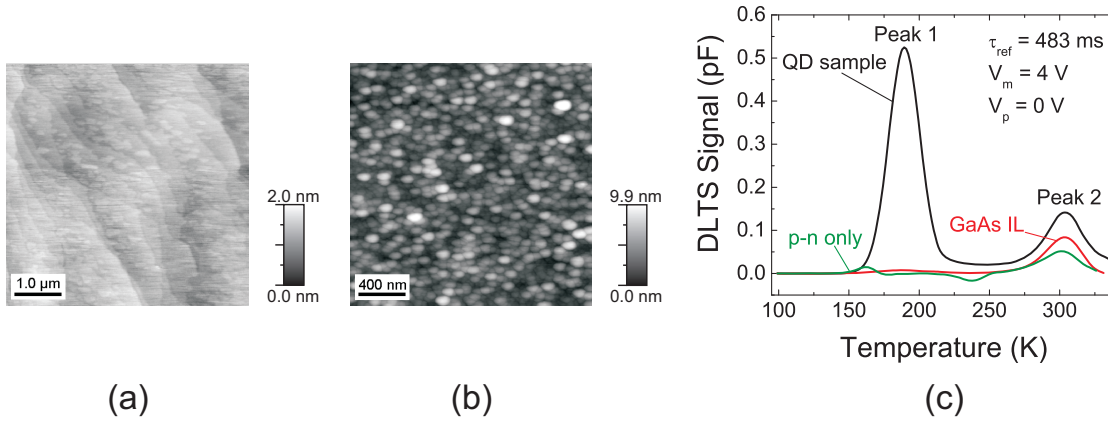


**Figure 6.2.:** (a) AFM micrograph of 2.4 ML  $In_{0.83}Ga_{0.17}As$  deposited on GaP with GRI = 180 s. No QD formation is visible. (b) AFM micrograph of 2.3 ML  $In_{0.25}Ga_{0.75}As$  deposited on a 3 ML GaAs interlayer on GaP with GRI = 100 s. Islands with a density of  $1.2 \times 10^{10} \text{ cm}^{-2}$  are clearly visible. Both samples were capped with 6 nm *i*-GaP. (c) Comparison of conventional DLTS spectra of the three samples of Fig. 6.1. Only the QD sample presents a very large peak centered around 190 K (Peak 1). All samples present a peak around 305 K (Peak 2), attributed to a deep state. (Reprint from [128]).

layer. By comparison, an AFM micrograph of a sample where 2.4 ML of  $In_{0.83}Ga_{0.17}As$  were deposited directly on GaP(001) is shown in Fig. 6.2a. The surface is flat and no QD morphology is visible.<sup>2</sup>

Conventional DLTS was performed on all samples between the temperatures 100 K and 330 K. The measurement voltage was set at  $V_m = 4 \text{ V}$  (reverse bias) and the QDs were charged with a 100 ms long pulse to  $V_p = 0 \text{ V}$ . A comparison of the results for the reference time  $\tau_{\text{ref}} = 483 \text{ s}$  is reported in Fig. 6.2c. The QD sample presents a very large peak around 190 K, which is attributed to the QDs. The other samples present only very small peaks in the same region (the p–n sample at 160 K and the IL sample at 190 K). Additionally, the pn sample presents a small negative peak around 235 K. All three samples present similar peaks around 305 K, which are therefore attributed to a deep defect in the GaP matrix. The respective activation energies and capture cross-sections are obtained through Arrhenius plots and reported in Table 6.1. Without entering into too much detail, the best estimate for the mean activation energy of the QDs is  $E_a = 450(\pm 20) \text{ meV}$ , with an apparent capture cross-section  $\sigma_\infty = 2 \times 10^{-13} \text{ cm}^2$  (with an uncertainty of 0.6 orders of magnitude). The resulting storage time at room temperature is 3  $\mu\text{s}$  (with an uncertainty of 0.3 orders of magnitude).

<sup>2</sup>For a more thorough discussion of the role played by the interlayer in enabling Stranski-Krastanow growth mode see [128].

## 6. InGaAs QDs in GaP

Sample	Peak	$\overline{E}_a$ (meV)	$\sigma_\infty$ (cm <sup>2</sup> )
QD	1	450	$2 \times 10^{-13}$
IL	1	380	$1 \times 10^{-15}$
p-n	1	430	$3 \times 10^{-12}$
QD	2	690	$5 \times 10^{-15}$
IL	2	680	$5 \times 10^{-15}$
p-n	2	650	$2 \times 10^{-15}$
p-n	neg.	660	$6 \times 10^{-12}$

**Table 6.1.:** Summary of the results of conventional DLTS on the three samples of Fig. 6.1, grouped by the peak to which they refer. Peak 1 and Peak 2 are marked in Fig. 6.2. The p-n sample is the only one presenting a negative peak (marked “neg.” in the table).

More detailed information on the localisation energy of the QDs can normally be retrieved from charge-selective DLTS. Unfortunately, charge-selective DLTS measurements could not be performed on this set of samples because the Zn ions used as dopants freeze out at low temperatures: Since the activation energy of Zn is relatively large (70 meV [130]), thermal excitation alone fails to ionise the dopants once the temperature is lowered, reducing the number of available charge carriers at lower temperatures. This issue did not disrupt conventional DLTS but proves critical for charge-selective DLTS, where a much smaller number of charge carriers has to be detected. A rough estimate of the localisation energy can be given based on the empirical observation that the ratio of the localisation energy to the mean activation energy is about  $E_{loc}/\overline{E}_a \simeq 1.4 - 2.0$  [14, 126–128, 145, 147, 153]. We then have  $E_{loc} \simeq 630 - 900$  meV for In<sub>0.25</sub>Ga<sub>0.75</sub>As/GaAs/GaP QDs [154], in agreement with the theoretical calculation of  $\sim 700$  meV for InAs/GaP QDs (Sc. 2.4.2).

### 6.2. Growth of In<sub>0.5</sub>Ga<sub>0.5</sub>As QDs in GaP

After perfecting the techniques developed for the growth via In<sub>0.25</sub>Ga<sub>0.75</sub>As/GaP QDs and described in the previous section, In<sub>0.5</sub>Ga<sub>0.5</sub>As QDs could be successfully grown via MOCVD at TU Berlin by G. Stracke and E. Sala, once again using a GaAs interlayer. In order to increase the localisation energy (and thereby the storage time) over the previous set of samples, two improvements were made to the design: On the one hand the In content was increased from  $x_{In} = 25\%$  to  $x_{In} = 50\%$ ; on the other hand an AIP barrier was placed below the QDs to hinder the emission of holes, but not their absorption. A sketch of the epitaxial structure of the samples in this batch is reported in Fig. 6.3. The

## 6.2. Growth of $In_{0.5}Ga_{0.5}As$ QDs in GaP

first sample (QD sample, Fig. 6.3a) contains both the QDs and the barrier; the second sample (barrier sample, Fig. 6.3b) contains only the AIP barrier; the third sample (p-n sample, Fig. 6.3c) contains neither, resulting in a simple GaP p-n<sup>+</sup> diode.

In the following, we will refer to these samples as *1-QD*, *1-Barr*, and *1-Ref*, respectively.

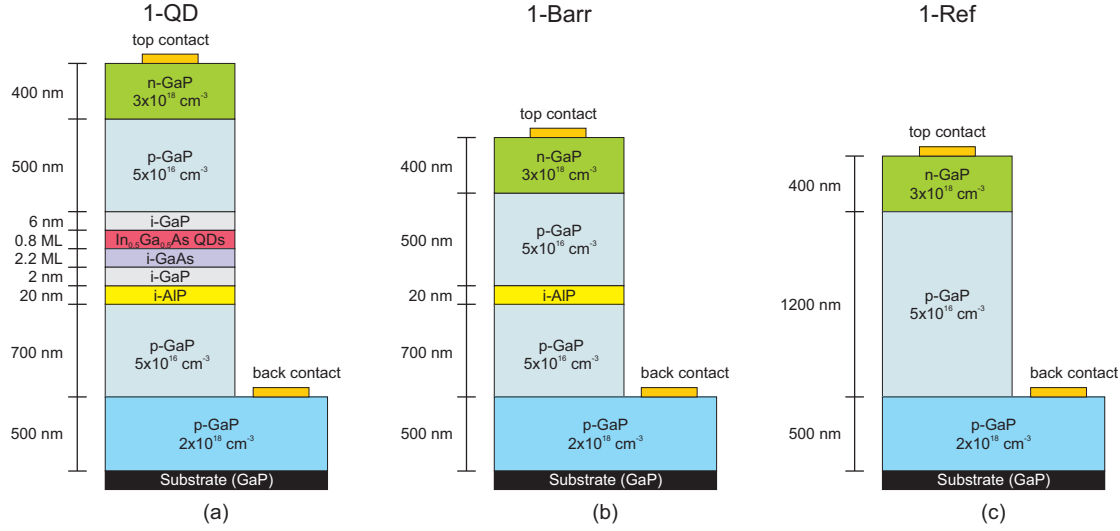


**Figure 6.3.:** Epitaxial structures of the  $In_{0.25}Ga_{0.75}As/GaAs/AIP/GaP$  sample set. (a) QD sample with barrier (1-QD):  $In_{0.5}Ga_{0.5}As$  QDs on a GaAs interlayer on an AIP barrier embedded in a GaP p-n<sup>+</sup> diode. (b) Barrier sample (1-Barr): AIP barrier layer embedded in a GaP p-n<sup>+</sup> diode. (c) p-n sample (1-Ref): GaP p-n<sup>+</sup> diode only.

All samples were grown on p-doped GaP(001) substrates using MOCVD. The 500 nm thick p<sup>+</sup>-doped ( $p = 2 \times 10^{18} \text{ cm}^{-3}$ ) GaP contact layer and the 700 nm thick lowly p-doped ( $p = 5 \times 10^{16} \text{ cm}^{-3}$ ) GaP layer were grown at a substrate temperature of 750 °C. The 20 nm AIP barrier and 2 nm i-GaP were grown at 800 °C. The 2 nm GaP layer serves to prevent the AIP surface from adsorbing impurities while cooling down to the QD growth temperature, which is 500 °C. 2.2 ML GaAs are deposited at this temperature, followed by 0.8 ML  $In_{0.5}Ga_{0.5}As$ . After deposition of the  $In_{0.5}Ga_{0.5}As$  layer a growth interruption (GRI) of 200 s is applied, followed by the deposition of a 6 nm thick i-GaP cap layer. Subsequent GaP layers were grown at 620 °C. Zn (for p) and Si (for n) were used as dopants. A set of identical samples were grown for AFM measurements, but in this case the QDs were left uncapped so that they can be observed via AFM. Further details on the growth of the samples and on the optimisation of the growth parameters can be found in [146]. All samples for DLTS are processed into round mesa structures of diameter  $d_1 = 400 \text{ }\mu\text{m}$  and  $d_2 = 800 \text{ }\mu\text{m}$  via standard optical lithography and dry

## 6. InGaAs QDs in GaP

etching methods. Two different sizes are used because larger mesas yield a more intense DLTS signal, but smaller mesas present a reduced RC low-pass filter effect. The contacts are evaporated thermally and annealed at 400 °C for 3 min, where Ni/AuGe/Au is used on the n side and Ni/Zn/Au on the p side. See App. C for details on the processing.

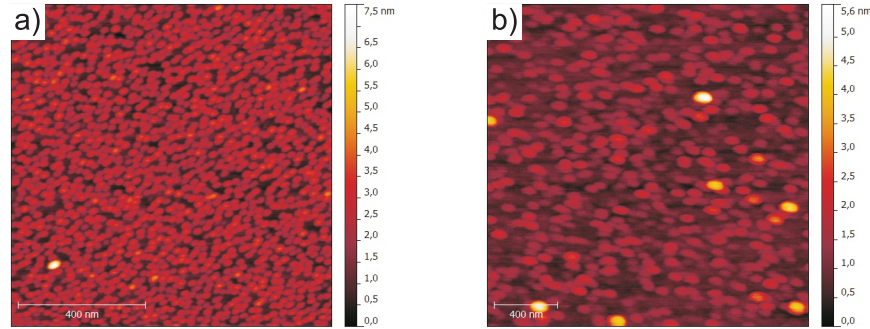


**Figure 6.4.:** AFM micrographs of (a) 1 ML  $\text{In}_{0.5}\text{Ga}_{0.5}\text{As}$  deposited on 2.2 ML GaAs on GaP (uncapped) and (b) 0.85 ML  $\text{In}_{0.5}\text{Ga}_{0.5}\text{As}$  deposited on 2 ML GaAs on GaP, capped with 6 nm GaP after a GRI of 200 s. QD nucleation is clearly visible in both samples, but the QDs are larger and less dense after the GRI and capping. The bright dot in (a) is a defect. (Courtesy of G. Stracke and E. Sala).

Fig. 6.4 shows AFM images of QD samples before capping (Fig. 6.4a) and after capping (Fig. 6.4b). Before capping the QDs have a density of  $1.5 \times 10^{11} \text{ cm}^{-2}$ , an average height of  $3.1(\pm 0.5) \text{ nm}$ , and an average base length of  $21.7(\pm 2.0) \text{ nm}$ . The sample in Fig. 6.4b is capped after a GRI of 200 s and presents larger QDs, which implies that ripening occurs during the GRI [146].

### 6.3. C-V characterisation

As a pre-characterisation step, static capacitance–voltage measurements are performed on the samples using measurement frequencies  $f = 1 \text{ kHz}$ ,  $f = 10 \text{ kHz}$ ,  $f = 100 \text{ kHz}$ , and  $f = 1 \text{ MHz}$ . The voltage was swept from  $V = -1.0 \text{ V}$  (forward bias) to  $V = 10.0 \text{ V}$  (reverse bias) in 0.05 V steps. The sampled temperatures range from  $T = 100 \text{ K}$  to  $T = 400 \text{ K}$ , in 50 K steps. As mentioned in Section 5.2.1, the hysteresis effect becomes more evident when the measurement frequency  $f$  is close to the inverse of the storage time  $1/\tau$ . Since long storage times are predicted for  $\text{In}_{0.5}\text{Ga}_{0.5}\text{As}/\text{GaP}$  QDs, we expect the effect to be more pronounced for smaller frequencies and for higher temperatures ( $\tau \sim e^{1/T}$ , see Eq. 3.16).

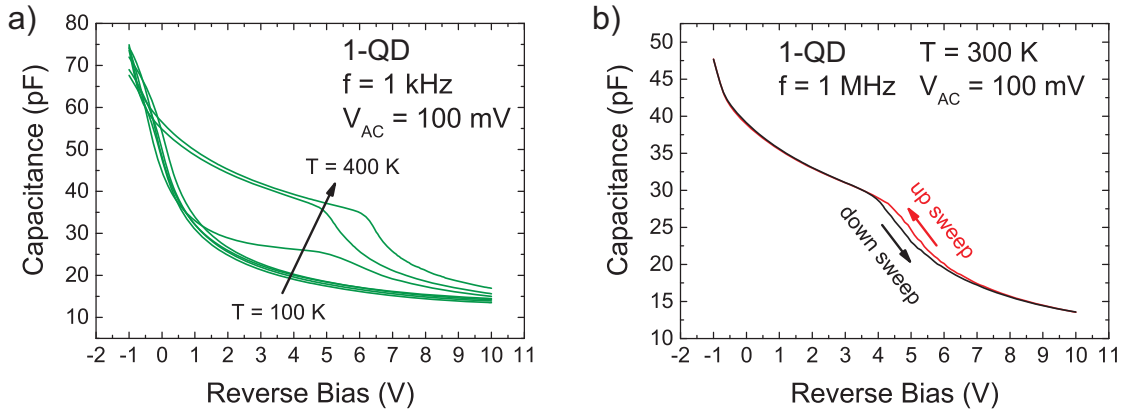


**Figure 6.5.:** (a)  $C$ - $V$  profiles of the sample 1-QD at temperatures ranging from  $T = 100$  K to  $T = 400$  K (measurement frequency  $f = 1$  kHz). The plateau induced by the QDs is visible from  $T = 300$  K upwards and extends roughly from 0 V to 6 V. (b) Room-temperature hysteresis in the capacitance of the QD sample ( $T = 300$  K,  $f = 1$  MHz). The hysteresis opening is located between 4 V and 6 V.

The temperature sweep (from  $T = 100$  K to  $T = 400$  K) for  $f = 1$  kHz is reported in Fig. 6.5a. The QD plateau is visible from a temperature of 300 K, where it ranges from ca. 1 V to ca. 5 V. It becomes larger for higher temperatures, extending from ca. 0 V to ca. 6 V for  $T = 400$  K. The hysteresis is shown directly in Fig. 6.5b for  $f = 1$  MHz and  $T = 300$  K. The frequency is higher than in Fig. 6.5a and the effect of the QDs less pronounced. Nonetheless, a clear hysteresis opening is visible between 4 V and 6 V. The  $C$ - $V$  characterisation indicates that the QDs are electrically active for a reverse bias  $V < 7$  V, and that they exhibit the strongest localization for reverse biases between 4 V and 6 V. The bias ranges determined via  $C$ - $V$  profiling will be used as orientation for the DLTS measurements to follow.

## 6.4. Conventional DLTS

In order to determine the mean activation energy  $E_A$  and the mean apparent capture cross-section for holes  $\sigma_\infty$ , “conventional” DLTS was performed on all samples (see Section 5.3). According to Fig. 6.5a, the QDs are completely unoccupied for a reverse bias  $V > 6$  V, and completely occupied for  $V < 0$  V. The measurement voltage is thus chosen as  $V_m = 7$  V (reverse bias) and the pulse voltage as  $V_p = -1$  V (forward bias), so that the totality of the bound states are involved in the measurement. The pulse length is chosen such that for all temperatures the hole capture process is completed before the end of

## 6. InGaAs QDs in GaP

the pulse ( $t_p = 2$  s), after which the emission transient is recorded for 18 s. Ten transients are recorded and averaged for each temperature in order to increase the signal-to-noise ratio (SNR). The temperature is swept from  $T = 100$  K to  $T = 400$  K in 2 K increases.

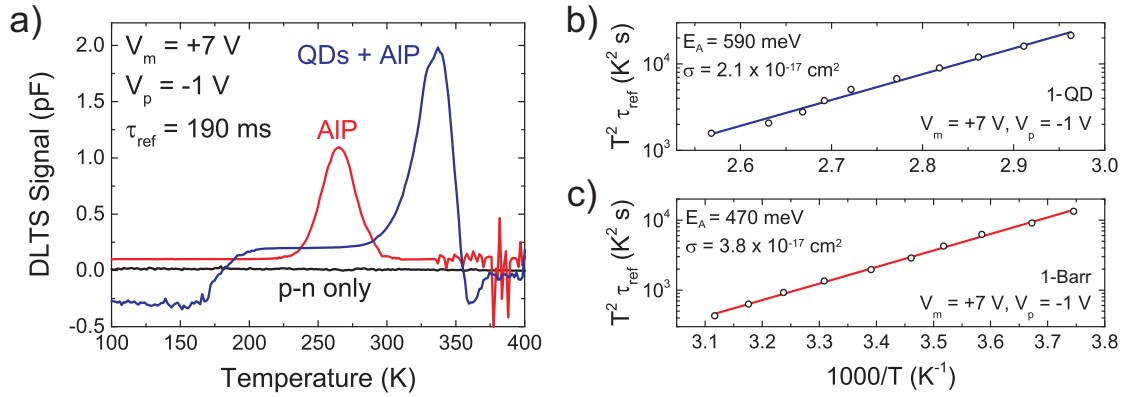


**Figure 6.6.:** (a) Comparison of conventional DLTS measurements carried out on the three samples. Sample 1-QD (blue) presents the largest peak, centred around  $T = 330$  K; sample 1-Barr (red) presents a smaller peak, centred around  $T = 265$  K; sample 1-Ref (black) presents no peak. (Reprint from [147]). Right-hand side: Corresponding Arrhenius plots for the QD sample (b) and AIP sample (c).

The DLTS spectra of the three samples are compared for  $\tau_{ref} = 190$  ms in Fig. 6.6a. The signals originating from the three samples are clearly distinguishable, with the QD sample producing the strongest signal (peak around  $T = 330$  K). The barrier contained in the AIP sample induces a peak in the DLTS signal centred around  $T = 265$  K, whereas the p–n sample produces a flat DLTS signal with no relevant features. The increased noise recorded from the AIP sample for higher temperatures is due to degradation of the sample, which was indeed destroyed during the measurement.

For  $T < 170$  K the signal from the QD sample becomes negative and remains constant at ca. -0.5 pF. A negative DLTS signal indicates either electron emission or hole capture, while a constant DLTS signal indicates a temperature-independent capture or emission process, i.e. tunnelling (see Ch. 3). Since the QDs are embedded in the p layer, electrons are the minority charge carriers and are therefore unlikely to be detected in DLTS. We therefore attribute the shoulder to hole capture into the QDs or into a deep defect via tunnelling.

Another dip of unknown origin is recorded for the QD sample at high temperatures. Considering that the dip disappears in charge-selective DLTS (see Fig. 6.7a), we attribute it to capture into a single-level system, i.e. a deep defect.

The results of conventional DLTS are analysed using the double-boxcar method setting

$t_1$  from 2 ms to 3 s,  $t_2 = 3t_1$ , and  $t_{av} = 0.5t_1$ . Ten DLTS spectra are thus obtained with  $\tau_{ref}$  ranging from 4 ms to 3.1 s. The results of the analysis (summarised in Table 6.2) confirm that the mean activation energy of the QD sample (580( $\pm$ 10) meV) is much higher than that of the AIP sample (470( $\pm$ 10) meV). The relative difference is expected to increase for the actual localisation energy, determined by charge-selective DLTS.

Sample	Peak	$\overline{E_a}$ (eV)	$\sigma_\infty$ (cm <sup>2</sup> )
1-QD	pos.	0.58( $\pm$ 0.01)	$2 \times 10^{-17}$ (0.1)
1-Barr	pos.	0.47( $\pm$ 0.01)	$4 \times 10^{-17}$ (0.1)
1-Ref	n/a	n/a	n/a
QD	neg.	0.73( $\pm$ 0.01)	$4 \times 10^{-16}$ (0.2)

**Table 6.2.:** Summary of the results of conventional DLTS on the three samples of Fig. 6.3. The  $p$ - $n$  sample does not present any peak. Only the QD sample presents a negative peak. The error on  $\sigma_\infty$  is reported in orders of magnitude in parentheses.

The double-boxcar method entails graphically identifying the position of the maximum of each DLTS spectrum. Since the identification of the peak is in itself a source of error, the procedure is repeated several times for each DLTS spectrum and the results of the separate evaluation are averaged to obtain the best estimate of the required parameters. The standard deviation from the average constitutes the best estimate of the experimental error. The uncertainty on  $\sigma_\infty$  is expressed in orders of magnitude because  $\sigma_\infty$  is derived from exponentiation of the intercept of the fit of the (linearised) Arrhenius plot. The error analysis is discussed in detail in App. A.

## 6.5. Charge-selective DLTS

The internal electronic structure of the QDs — and thereby their localisation energy — can be investigated by means of charge-selective DLTS (see Section 5.3.4). The relevant voltage range is the same as the one used for conventional DLTS, and the height of the pulse must be chosen so that a small number of charge carriers (ideally one per QD) is captured and re-emitted for each voltage step. For the QD sample, the measurement voltage is incremented from  $V_m = 0.0$  V to  $V_m = 6.5$  V in 0.5 V steps, with a pulse height of 0.5 V ( $V_p = V_m - 0.5$  V). As before, the pulse length is 2 s, after which the transient is recorded for 18 s. The temperature is swept from  $T = 100$  K to  $T = 400$  K in 2 K increments and ten transient are recorded and averaged per temperature step.

The results of this measurement are again analysed using the double-boxcar method

## 6. InGaAs QDs in GaP

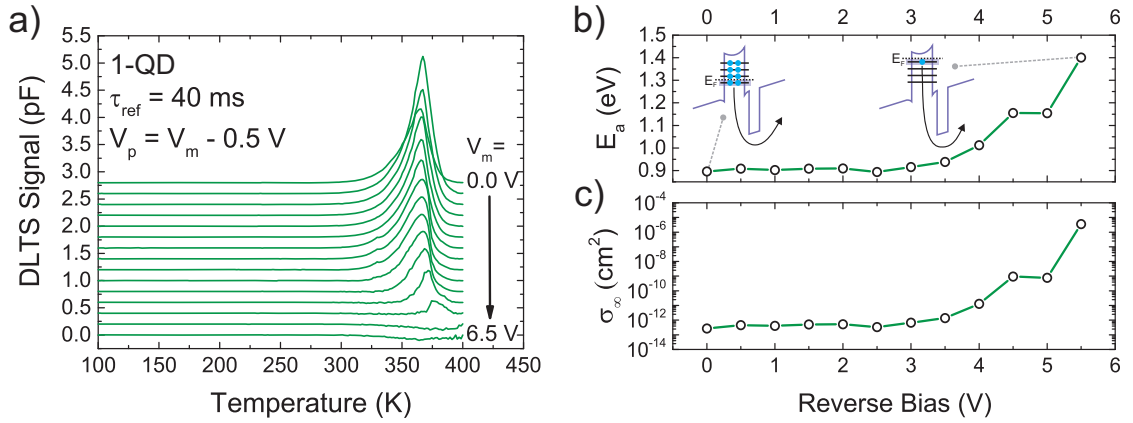


**Figure 6.7.:** Summary of the results of charge-selective DLTS on sample 1-QD. (a) DLTS signal for  $\tau_{\text{ref}} = 40$  ms and measurement voltages spanning the interval  $V_m = 0$  V to  $V_m = 6.5$  V (offset for ease of reading). (b) Activation energies and (c) capture cross-sections extracted from the same measurement. The activation energy increases sharply for higher voltages because deeper and deeper bound states in the QDs are being probed, as sketched in (b). (Partially reprinted from [147]).

with  $t_1$  from 2 ms to 3 s,  $t_2 = 3t_1$ , and  $t_{av} = 0.5t_1$ . Ten DLTS spectra are thus obtained for each voltage with  $\tau_{\text{ref}}$  ranging from 4 ms to 3.1 s. The spectra with  $\tau_{\text{ref}} = 40$  ms are reported for all voltages in Fig. 6.7a. A single peak is visible in the charge-selective DLTS measurement and it is located around  $T = 365$  K for all voltages  $V_m \leq 3.0$  V, at which point it starts shifting towards higher temperatures until it reaches ca.  $T = 380$  K for  $V_m = 5.5$  V. The peak vanishes for  $V_m \geq 6.0$  V, indicating that for higher biases the charge pulse is not sufficient to charge any bound state of the QDs. In other words, for  $V_{\text{ext}} > 5.5$  V (reverse bias) the QD layer is always inside the depletion layer, where no holes are available for capture and subsequent re-emission. As a consequence, the DLTS signal remains flat across the temperature range of interest.

The measured activation energy (Fig. 6.7b) starts off at about  $0.90(\pm 0.01)$  eV for  $V_m = 0.0$  V and gradually increases until  $1.40(\pm 0.07)$  eV for  $V_m = 5.5$  V, as the charge-selective DLTS measurement probes deeper and deeper bound states. The capture cross-section (Fig. 6.7c) follows a similar pattern, starting off at  $4 \times 10^{-13}$  cm<sup>2</sup> (with an uncertainty of 0.1 orders of magnitude) and increasing until  $8 \times 10^{-7}$  cm<sup>2</sup> (with an uncertainty of 0.8 orders of magnitude).

Since the peak for  $V_m = 5.5$  V is very small, the accuracy of the estimate of the corresponding activation energy is also small. Furthermore, the activation energies and capture cross-sections for  $V_m = 5.0$  V and  $V_m = 4.5$  V are identical (within their uncer-

ainties):  $E_a = 1.15(\pm 0.03)$  eV,  $\sigma_\infty = 8 \times 10^{-10}$  cm<sup>2</sup> (with an uncertainty of 0.4 orders of magnitude); and  $E_a = 1.15(\pm 0.02)$  eV,  $\sigma_\infty = 9 \times 10^{-10}$  cm<sup>2</sup> (with an uncertainty of 0.3 orders of magnitude), respectively. We therefore interpret the two data points as originating from the same internal level in the QDs. We decide to discard the data relative to the point at  $V_m = 5.5$  V as an artefact and assign to the “QDs + AIP” system a localization energy of  $1.15(\pm 0.03)$  eV with an associated capture cross-section of  $8 \times 10^{-10}$  cm<sup>2</sup> (with an uncertainty of 0.4 orders of magnitude). We attribute the  $0.90(\pm 0.01)$  eV localization visible for  $V_r \leq 2.5$  V to the effect of the barrier. For further details on data analysis and attribution of the experimental error see App. A.

A similar charge-selective DLTS measurement was carried out on the AIP barrier sample with measurement voltages spanning the interval from  $V_m = 0.0$  V to  $V_m = 7.0$  V in 1.0 V increments. As before, the pulse length is 2 s, after which the transient is recorded for 18 s; the temperature is swept from  $T = 100$  K to  $T = 400$  K in 2 K increments; and ten transient are recorded and averaged per temperature step.

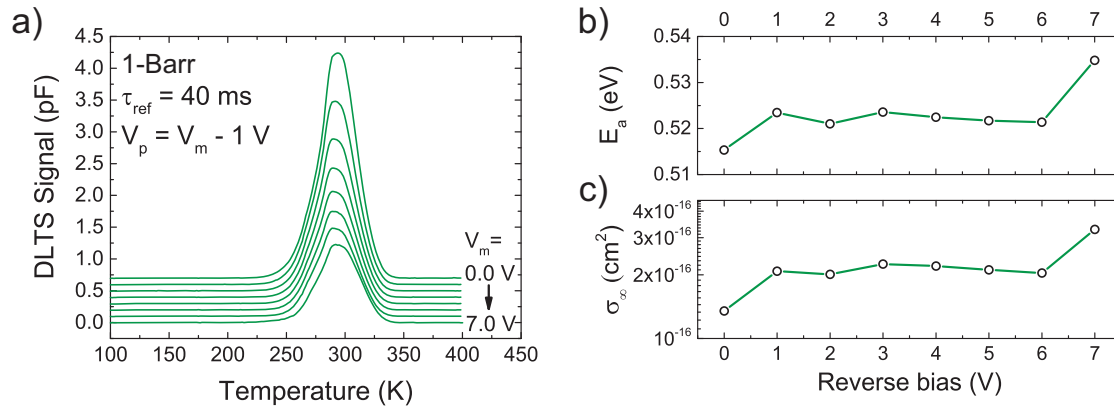


**Figure 6.8.:** Summary of the results of charge-selective DLTS on the QD sample. (a) DLTS signal for  $\tau_{ref} = 40$  ms and measurement voltages spanning the interval  $V_m = 0$  V to  $V_m = 7$  V (offset for ease of reading). (b) Activation energies and (c) capture cross-sections extracted from the same measurement. The activation energy remains roughly constant for all biases because a barrier (as opposed to QDs) does not create multiple bound states with different energies. (Partially reprinted from [147]).

Also these results are analysed using the double-boxcar method with  $t_1$  from 2 ms to 3 s,  $t_2 = 3t_1$ , and  $t_{av} = 0.5t_1$ . Ten DLTS spectra are thus obtained for each voltage with  $\tau_{ref}$  ranging from 4 ms to 3.1 s. The spectra with  $\tau_{ref} = 40$  ms are reported for all voltages in Fig. 6.8a. Again, one single peak is visible in the DLTS signal, but this time it is centred around ca.  $T = 290$  K for all voltages, changing only in amplitude from one voltage to the next. The fact that the peak does not shift indicates that the localisation

## 6. InGaAs QDs in GaP

effect is the same for all voltages, as expected for a barrier as opposed to quantum dots. The hypothesis is confirmed by the activation energy (Fig. 6.8b), which oscillates around a value of  $0.52(\pm 0.01)$  eV for all voltages. Correspondingly, the capture cross-section oscillates around the average value of  $2 \times 10^{-16}$  cm<sup>2</sup>, with an uncertainty of 0.1 orders of magnitude (Fig. 6.8c). The literature value for the valence band mismatch of AIP in GaP is ca. 0.50 eV [56], in good agreement with our result. In principle, one would expect to measure in sample 1-Barr the same activation energy measured in sample 1-QD for low voltages, where the effect of quantum dots should not be visible. However, the value of 0.90 eV does not represent the height of the AIP barrier alone, but rather the combined effect of the barrier and the QDs. The shallowest bound level in the QDs is deeper into the band gap than the top of the valence band and therefore contributes additional localization energy (see Fig. 6.7b for a sketch of the emission process).

A charge-selective DLTS measurement is carried out also on the reference sample (p–n diode) with the same parameters as the AIP barrier sample ( $V_m = 0.0$  V to  $V_m = 7.0$  V in 1.0 V increments; pulse length 2 s; transient length 18 s;  $T = 100$  K to  $T = 400$  K in 2 K increments; 10 transients per temperature step). As expected for the reference sample, the DLTS spectra obtained via double-boxcar analysis do not show any relevant feature and are therefore not reported here.

The localisation energy of the sole InGaAs QDs can be estimated by subtracting the height of the barrier from the total localisation energy:

$$1.15(\pm 0.03) \text{ eV} - 0.52(\pm 0.01) \text{ eV} = 0.63(\pm 0.03) \text{ eV}.$$

The projected localisation energy for InAs QDs in GaP is 701 eV. This value has to be corrected downwards because the QDs are not pure InAs QDs, but rather InGaAs QDs. Once the correction and the experimental error are taken into account, the measured value is in good agreement with the estimate.

### 6.6. Storage time at room temperature

The storage time at room temperature for holes can be extrapolated from the localisation energy and the capture cross-section by rearranging Eq. 3.16 as:

$$\tau = \frac{1}{\gamma_p T^2 \sigma_p^\infty} \exp\left(\frac{E_{\text{loc}}^p}{k_B T}\right), \quad (6.1)$$

## 6.6. Storage time at room temperature

where  $\gamma_p$  is a material-specific parameter (for GaP:  $\gamma_p^{\text{GaP}} = 2.57 \times 10^{25}$ ) and  $k_B$  is Boltzmann's constant. By substituting  $E_{\text{loc}} = 1.15(\pm 0.03)$  eV,  $\sigma_p^\infty = 8 \times 10^{-10}$  cm<sup>2</sup> (with an uncertainty of 0.4 orders of magnitude), and  $T = 300$  K, Eq. 6.1 yields a storage time at room temperature for holes in In<sub>0.5</sub>Ga<sub>0.5</sub>As/AIP/GaSb QDs  $\tau = 260$  s (with an uncertainty of 0.1 orders of magnitude). The rather large uncertainty associated to the extrapolation is due to the uncertainty on the estimate of the capture cross-section via double-boxcar method. Nonetheless, even within the error margin, the storage time of In<sub>0.5</sub>Ga<sub>0.5</sub>As/AIP/GaSb QDs represents an improvement of 2 orders of magnitude over the previous record value of 1.6 s for GaSb/Al<sub>0.9</sub>Ga<sub>0.1</sub>As/GaAs QDs [14].

As a side note, the localisation energy measured for In<sub>0.5</sub>Ga<sub>0.5</sub>As/AIP/GaSb QDs would be sufficient for non-volatility if the capture cross-section was smaller than  $4 \times 10^{-16}$  cm<sup>2</sup>, which lies outside the range of usual capture cross-sections for self-organised QDs. This system is therefore not a promising candidate for achieving non volatility.

### Summary

- Direct growth of InGaAs on GaP does not show quantum dot nucleation. Nucleation can be induced by introducing a thin (few monolayers thick) GaAs interlayer below the InGaAs layer.
- Three InGaAs/GaP QDs samples were characterised: Sample 1-QD, containing  $\text{In}_{0.5}\text{Ga}_{0.5}\text{As}$  QDs embedded in GaP with an AlP barrier; Sample 1-Barr, containing only the barrier; Sample 1-Ref, constituted by a simple p-n<sup>+</sup> diode and used as a reference.
- The effect of quantum dots is clearly visible in the C-V characteristic, both as a plateau and as a hysteresis opening.
- Samples 1-QD and 1-Barr both present one large peak in the conventional DLTS signal. The positions of the peaks and their associated activation energies, however, are clearly distinguished. Conventional DTLS on sample 1-Ref does not present any peak.
- The localisation energies of samples 1-QD and 1-Barr are determined via charge-selective DLTS as  $1.15(\pm 0.03)$  eV (with an associated capture cross-section of  $8 \times 10^{-10}$  cm<sup>2</sup> with an uncertainty of 0.4 orders of magnitude) and  $0.52(\pm 0.01)$  eV (with an associated capture cross-section of  $2 \times 10^{-16}$  cm<sup>2</sup> with an uncertainty of 0.1 orders of magnitude). Subtracting the former from the latter yields a hole localisation energy for the sole QDs (without the barrier) of  $0.63(\pm 0.03)$  eV.
- The room-temperature storage time for holes in  $\text{In}_{0.5}\text{Ga}_{0.5}\text{As}/\text{GaAs}/\text{AlP}/\text{GaP}$  QDs is 260 s (with an uncertainty of 0.1 orders of magnitude), an improvement of 2 orders of magnitude over the previous record figure.

## 7. GaSb QDs in GaP

The more you love a memory, the stronger and stranger it is.

---

*(Vladimir Nabokov)*

This chapter describes the growth and characterization of a set of samples containing GaSb QDs embedded in GaP. Each sample was grown under slightly different growth conditions in order to test their effect on the localisation energy and capture cross-section of the QDs. The samples were grown by MBE by Xavier Wallart's group, at the Institute of Electronics, Microelectronics and Nanotechnology (IEMN) of the University of Lille Nord, France.

Some of these results have already been published in [153]. An article detailing the growth of the samples is under consideration by the journal *Nanotechnology*.<sup>1</sup>

### 7.1. Growth of GaSb QDs in GaP

The GaSb/GaP QDs system is very interesting not only because of the very high projected localisation energy of 1.4 eV [56, 155, 156], but also because it represents a completely novel system, its first successful growth having been reported only in 2012 [157, 158]. Seven different samples were grown, each of them with slight variations in the growth parameters, so that their effect on localisation energy and capture cross-section can be determined experimentally. Schematics of the epitaxial structure of the sample batch are reported in Fig. 7.1. Five samples (2-QD-A, 2-QD-B, 2-QD-C, 2-QD-D, 2-QD-E) contain GaSb QDs. The deposition temperature was increased in 20 °C steps while keeping the deposition thickness constant (1.2 ML) in the first three samples. The fourth sample was grown at the highest temperature, but the growth rate was halved. In the fifth sample,

---

<sup>1</sup>L. Desplanque, C. Coinon, D. Troadec, P. Ruterana, G. Patriarche, L. Bonato, D. Bimberg and X. Wallart, "Morphology and valence band offset of GaSb quantum dots grown on GaP(001) and their evolution upon capping".

## 7. GaSb QDs in GaP

the layer thickness is increased to 1.6 ML and the temperature reduced again to 450 °C. An additional sample (2-QD-AIP) was grown under the same conditions as those of sample 2-QD-D, but in this case the QDs were capped with a thin layer of i-AIP (3 nm) before proceeding with the growth of the layers above the QDs. Finally, a sample without the QD layer was grown as reference.

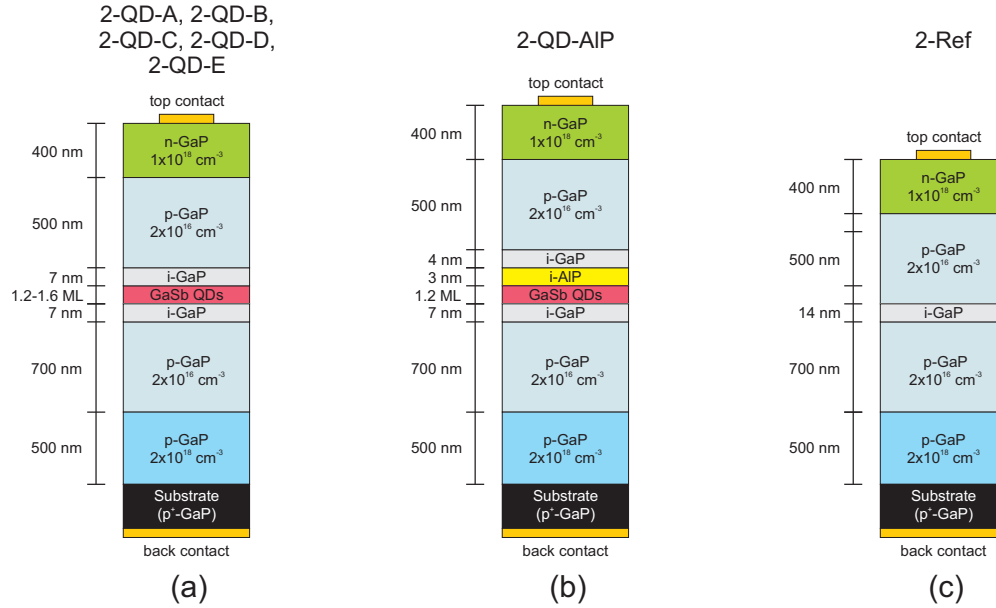


**Figure 7.1.:** Epitaxial structure of the batch of sample containing GaSb QDs embedded in GaP. (a) Common structure of the 5 QD samples 2-QD-A, 2-QD-B, 2-QD-C, 2-QD-D, and 2-QD-E. The differences in the growth parameters are reported in Tab. 7.1. (b) 2-QD-AIP sample (with 3 nm AIP capping). (c) Reference sample (2-Ref): p-n diode with embedded 14 nm i-GaP.

Sample	QD thickness	QD temperature	$v_{\text{Ga}}$
2-QD-A	1.2 ML	430 °C	0.2 ML/s
2-QD-B	1.2 ML	450 °C	0.2 ML/s
2-QD-C	1.2 ML	470 °C	0.2 ML/s
2-QD-D	1.2 ML	470 °C	0.1 ML/s
2-QD-E	1.6 ML	450 °C	0.2 ML/s
2-QD-AIP	1.2 ML	470 °C	0.1 ML/s
2-Ref	n/a	n/a	0.2 ML/s

**Table 7.1.:** Growth parameters used for the QD layer in the 7 samples of the GaSb/GaP QDs batch: Thickness of the QD layer (in monolayers), deposition temperature of the QD layer, and growth rate (expressed as Ga flux  $v_{\text{Ga}}$ , reported in ML/s).

### 7.1. Growth of GaSb QDs in GaP

All samples were grown on p-doped (nominal  $p = 1.3 \times 10^{18} \text{ cm}^{-3}$ ) GaP(001) substrates using MBE. The 500 nm thick p<sup>+</sup>-doped ( $p = 2 \times 10^{18} \text{ cm}^{-3}$ ) GaP contact layer was grown at 600 °C at a growth rate of 1 ML/s, whereas the 700 nm thick lowly p-doped ( $p = 2 \times 10^{16} \text{ cm}^{-3}$ ) GaP layer and the 7 nm undoped GaP layer were grown at 560 °C. The growth parameters for the QD layer are reported in Tab. 7.1. After a growth interruption of 50 s, the QDs were capped with 7 nm of undoped GaP at 430 °C and 0.2 ML/s growth rate (for sample 2-QD-AIP: 3 nm of i-AIP, followed by 4 nm of i-GaP). Subsequent layers were grown at 560 °C (500 nm,  $p = 2 \times 10^{16} \text{ cm}^{-3}$ ) and 600 °C (400 nm,  $n = 1 \times 10^{18} \text{ cm}^{-3}$ ). Be (for p) and Si (for n) were used as dopants. All samples for DLTS are processed using the simplified processing described in App. C, which results in structures of effective diameter  $d_1 = 400 \mu\text{m}$  and  $d_2 = 800 \mu\text{m}$ . The contacts are evaporated thermally and annealed at 400 °C for 3 min, where Ni/AuGe/Au is used on the n side and Ni/Zn/Au on the p side.

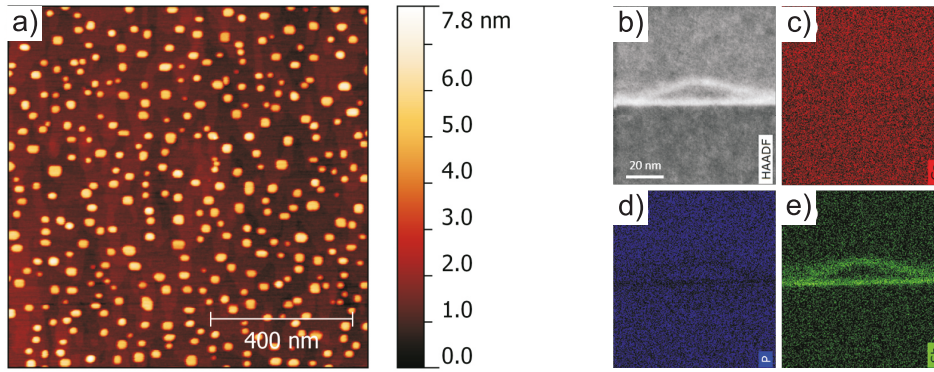


**Figure 7.2.:** (a) AFM micrograph of a GaSb/GaP QDs sample, uncapped. (Courtesy of IEMN, Lille). (b) HAADF-STEM image of a single QD from the same sample, with EDX maps representing the content of Ga (c), P (d), and Sb (e). (Courtesy of C2N, Marcoussis).

Fig. 7.2a shows an AFM micrograph of a sample identical to 2-QD-D up to the QD layer, which is then left uncapped. The average lateral size of the QDs is ca. 36 nm, their height ca. 8 nm, and their density  $9 \times 10^9 \text{ cm}^{-2}$ .

The capped samples were also characterised by high annular dark field (HAADF) analysis [159] carried out in a scanning electron microscope (STEM). The image of a single QD from sample 2-QD-D is reported in Fig. 7.2b, alongside the energy-dispersive X-ray spectroscopy (EDX) maps constructed from the image to determine the relative content of Ga (Fig. 7.2c), P (Fig. 7.2d), and Sb (Fig. 7.2e). The EDX maps indicate that the QDs become some kind of core-shell structure upon capping, with segregation of Sb on the edge of the dots. Fig. 7.2d indicates strong intermixing of P into the QDs. It is

important to note that the estimate for the localisation energy of 1.4 eV does not account for intermixing, which is expected to reduce the localisation energy sizeably.

## 7.2. C-V characterisation

Capacitance–voltage characteristics were acquired for all samples using measurement frequencies  $f = 1$  kHz,  $f = 10$  kHz,  $f = 100$  kHz, and  $f = 1$  MHz. The voltage was swept from  $V = -1.0$  V (forward bias) to  $V = 15.0$  V (reverse bias) in 0.05 V steps. The sampled temperatures range from  $T = 100$  K to  $T = 400$  K, in 50 K steps. A plateau could be identified in all samples containing QDs, and its position determined the voltages used for DLTS (see below).

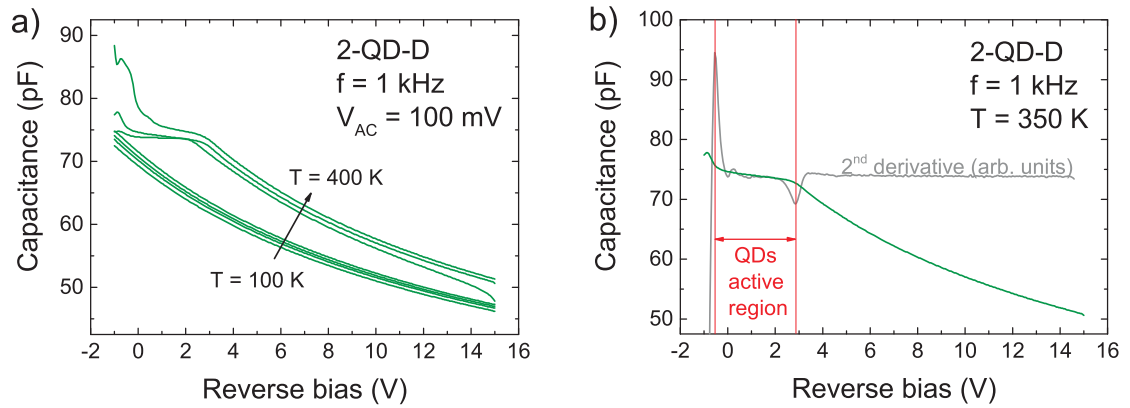


**Figure 7.3.:** (a) C–V profiles of sample 2-QD-D for temperatures ranging from  $T = 100$  K to  $T = 400$  K (measurement frequency  $f = 1$  kHz). The QD plateau becomes visible from  $T = 300$  K and becomes more pronounced for higher temperatures. (b) C–V profile for  $T = 350$  K (green) and second derivative of the profile (gray). The (local) maximum and minimum of the second derivative (highlighted with red lines) identify the range of voltages for which the QDs are electrically active.

As an example, the C–V profiles of sample 2-QD-D for  $f = 1$  kHz are reported in Fig. 7.3a. The QD plateau becomes visible at  $T = 300$  K in the region between  $V = -1.0$  V (forward bias) and  $V = 4.0$  V (reverse bias), becoming more pronounced for higher temperatures. Fig. 7.3b reports only the C–V profile acquired at  $T = 350$  K alongside its second derivative (gray). The second derivative shows a clear (local) maximum at  $V \simeq -0.5$  V and (local) minimum at  $V \simeq 3.0$  V. These voltages identify the interval where QDs are electrically active and will be used as orientation for the DLTS measurements.

### 7.3. Conventional DLTS

Conventional DLTS was performed on all samples of the batch using the bias voltages obtained from the respective C–V profiles. The bias used are reported in the second and third column of Tab. 7.2. For all measurements, the charging pulse lasted 5 s and the subsequent capacitance transient was recorded for 95 s. The temperature was swept from  $T = 200$  K to  $T = 400$  K in 2 K steps. Ten transients were acquired per step and averaged to increase the signal-to-noise ratio.

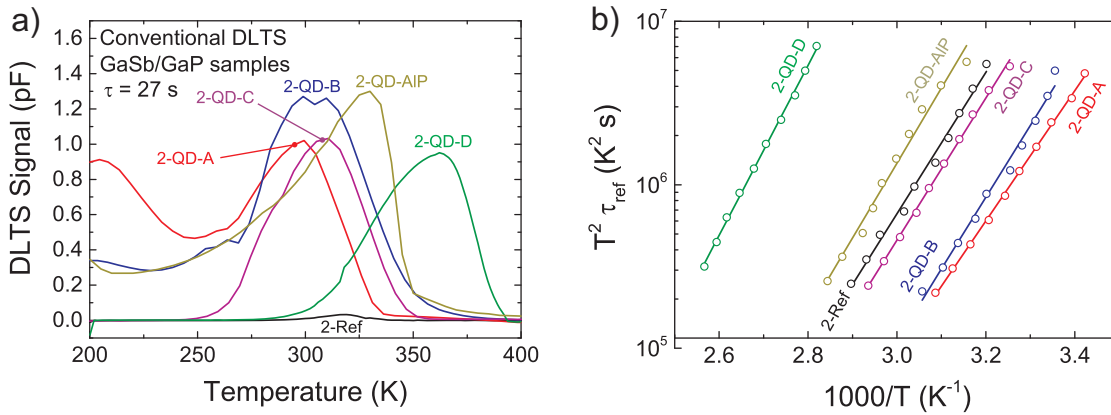


**Figure 7.4.:** (a) Conventional DLTS measurements performed on all GaSb/GaP QDs samples with reference time  $\tau_{\text{ref}} = 27$  s. (b) Arrhenius plots of the same measurements.

The conventional DLTS measurements were analysed with the double-boxcar method with  $t_1$  ranging from 1 s to 27 s,  $t_2 = 3t_1$ , and  $t_{\text{av}} = 0.5t_1$ . These parameters yield reference times  $\tau_{\text{ref}}$  between 2 s and 56 s. Fig. 7.4a shows the spectra of all samples with  $\tau_{\text{ref}} = 27$  s. Sample 2-Ref presents only one very small peak, centred around  $T \simeq 320$  K. Samples 2-QD-A, 2-QD-B, and 2-QD-C present similar peaks, all centred around 300 K. We expect these three samples to demonstrate similar localisation energies. Sample 2-QD-AIP presents one asymmetric peak which reaches its maximum around  $T \simeq 330$  K. Finally, sample 2-QD-D presents one peak at much higher temperatures ( $T \simeq 365$  K), suggesting a much longer localisation time than the other samples.

Sample 2-QD-E is missing from Fig. 7.4 because it presents no DLTS peaks. The sample will therefore be excluded from the present discussion.

Only sample 2-QD-A presents a second peak (partially visible in Fig. 7.4a at low temperatures). The peak can be made to fall completely in the chosen temperature range by reducing the reference time appropriately ( $t_1$  ranging from 100 ms to 1 s were used in this case, yielding reference times between 200 ms and 2 s). The activation energy is thus

## 7. GaSb QDs in GaP

determined as  $E_a = 580$  meV, with an apparent capture cross-section  $\sigma_\infty = 2 \times 10^{-13}$  cm<sup>2</sup>. The peak is attributed to a defect.

Sample	$V_m$ (V)	$V_p$ (V)	$E_a$ (meV)	$\sigma_\infty$ (cm <sup>2</sup> )
2-Ref	4.0	-1.0	852( $\pm 9$ )	$9 \times 10^{-15}$ (0.1)
2-QD-A	10.0	-1.0	790( $\pm 10$ )	$6 \times 10^{-15}$ (0.2)
2-QD-B	10.0	-1.0	850( $\pm 10$ )	$9 \times 10^{-14}$ (0.2)
2-QD-C	6.0	-1.0	860( $\pm 20$ )	$2 \times 10^{-14}$ (0.4)
2-QD-D	4.0	-2.0	1030( $\pm 10$ )	$5 \times 10^{-14}$ (0.2)
2-QD-AIP	15.0	-1.0	890( $\pm 20$ )	$2 \times 10^{-14}$ (0.3)

**Table 7.2.:** Bias settings and results for the main peaks of conventional DLTS on the GaSb/GaP samples. The error on  $\sigma_\infty$  is reported in orders of magnitude in parentheses.

The analysis of the main peaks yields the Arrhenius plots in Fig. 7.4b, and the estimates for mean, ensemble activation energy and apparent capture cross-section reported in Tab. 7.2 (for further details on data analysis and attribution of the uncertainty see App. A). These values represent the average over all internal states of the QDs, which are expected to demonstrate much higher localisation energies in charge-selective DTLS.

The mean activation energies of all samples fall between 790 meV and 890 meV, with the notable exception of sample 1-QD-D, which presents a much higher activation energy  $E_a = 1.03(\pm 0.01)$  eV, with an associated capture cross-section  $\sigma_\infty = 5 \times 10^{-14}$  cm<sup>2</sup>(with an uncertainty of 0.2 orders of magnitude). The mean, ensemble storage time at room temperature resulting from these values is  $\tau = 36000$  s (0.4 days), with an uncertainty of 0.04 orders of magnitude.

### 7.4. Charge-selective DLTS

Charge-selective DLTS was performed on all samples, choosing the biases according to the results of conventional DLTS. The temperature was swept from  $T = 200$  K to  $T = 400$  K in 2 K steps. The pulse length was 5 s and the subsequent transient was recorded for 95 s. Ten transients were acquired for each step and averaged to improve the signal-to-noise ratio. All DLTS spectra were analysed with the double-boxcar method, with  $t_1$  ranging from 1 s to 27 s,  $t_2 = 3t_1$ ,  $t_{av} = 0.5t_1$ . The resulting reference times span the 2 s to 56 s interval. The experimental error was attributed according to App. A, which also contains details on the statistical analysis.

Sample 2-QD-E is not reported on because the DLTS spectra do not present any feature of interest.

### 7.4.1. Sample 2-Ref

Charge-selective DLTS was performed on sample 2-Ref with measurement voltages ranging from  $V_m = -0.5$  V to  $V_m = 4.0$  V in 0.5 V steps. As shown in Fig. 7.5, the DLTS signal is flat for all measurement voltages. Charge-selective DLTS is mostly sensitive to localisation centres concentrated in a plane, and yields the best results for localisation centres presenting several bound states. As a consequence, charge-selective DLTS is suitable for self-organised QDs, but not for deep defects distributed uniformly in the bulk of the material. The absence of peaks in this measurement therefore confirms that the small peak seen in conventional DLTS (see Fig. 7.4 and Tab. 7.2) originates from a deep defect.

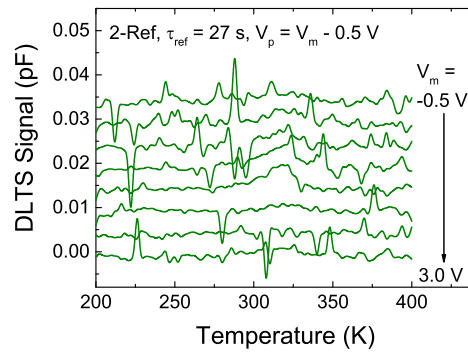


*Figure 7.5.: Charge-selective DLTS spectra measured on sample 2-Ref for  $\tau_{ref} = 27$  s. As expected, the reference sample produces no peaks.*

### 7.4.2. Sample 2-QD-A

Charge-selective DLTS was performed on sample 2-QD-A with measurement voltages ranging from  $V_m = 0.0$  V to  $V_m = 10.0$  V in 1.0 V steps. Fig. 7.6a reports the DLTS spectra for  $\tau_{ref} = 27$  s. A single peak is visible around  $T \simeq 200$  K for  $V_m = 0.0$  V, and shifts smoothly towards higher temperatures with increasing biases, until it reaches  $T \simeq 300$  K for  $V_m = 10.0$  V.

Correspondingly, the activation energy starts off at  $E_a = 578(\pm 6)$  meV, increasing gradually to  $E_a = 900(\pm 20)$  meV for  $V_m = 10.0$  V (see Fig. 7.6b). The last value represents the localisation energy of this sample.

The apparent capture cross-section (Fig. 7.6c) appears to vary in the  $10^{-13}$ – $10^{-11}$  cm<sup>2</sup> interval without a defined trend. At  $V_m = 0.0$  V it amounts to  $9 \times 10^{-14}$  cm<sup>2</sup> (with an

## 7. GaSb QDs in GaP

uncertainty of 0.1 orders of magnitude), and at  $V_m = 10.0$  V to  $4 \times 10^{-13}$  cm<sup>2</sup> (with an uncertainty of 0.3 orders of magnitude).

To sum up, the localisation energy of sample 2-QD-A is  $E_{loc} = 900(\pm 20)$  meV, with an associated apparent capture cross-section  $\sigma_\infty = 4 \times 10^{-13}$  cm<sup>2</sup> (with an uncertainty of 0.3 orders of magnitude).

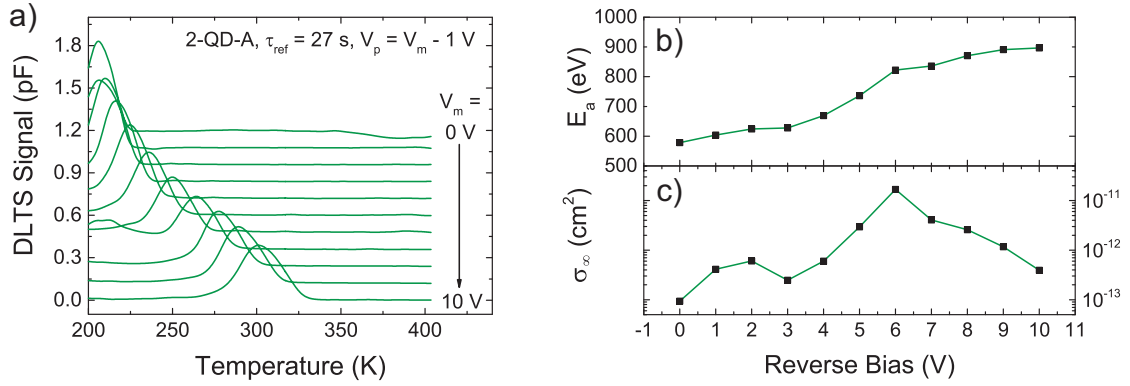


**Figure 7.6.:** Summary of the results of charge-selective DLTS on sample 2-QD-A. (a) DLTS signal for  $\tau_{ref} = 27$  s,  $V_m = 0.0$  V to  $V_m = 10.0$  V,  $V_p = V_m - 1.0$  V (offset for ease of reading). (b) Activation energies and (c) capture cross-sections extracted from the same measurement.

### 7.4.3. Sample 2-QD-B

Charge-selective DLTS was performed on sample 2-QD-B with measurement voltages ranging from  $V_m = 0.0$  V to  $V_m = 10.0$  V in 1.0 V steps. Fig. 7.7a reports the DLTS spectra for  $\tau_{ref} = 27$  s for the measurement voltages  $V_m = 1.0$  V to  $V_m = 10.0$  V. The spectra acquired at  $V_m = 0.0$  V do not present any peaks. The spectra are noticeably noisier than those of the other samples, indicating that either the structural integrity of the sample or the quality of the contacts might be compromised. The smaller signal-to-noise ratio reflects into larger uncertainties on the estimates of activation energy and capture cross-section, but does not prevent the analysis of the spectra: A single peak is still clearly distinguishable in Fig. 7.7a. It appears around  $T \simeq 270$  K for  $V_m = 1.0$  V and shifts smoothly towards higher temperatures with increasing biases, until it reaches  $T \simeq 350$  K for  $V_m = 10.0$  V.

The activation energy starts off at  $E_a = 687(\pm 7)$  meV, increasing gradually to  $E_a = 1100(\pm 30)$  meV for  $V_m = 10.0$  V (see Fig. 7.7b). The last value represents the localisation energy of this sample.

The apparent capture cross-section (Fig. 7.7c) shows little variation for biases between

1.0 V and 8.0 V, with values around  $10^{-13}$  cm<sup>2</sup> for all voltages (with the notable exception of  $\sigma_{\infty} = 2 \times 10^{-12}$  cm<sup>2</sup> for  $V_m = 3.0$  V). It increases abruptly for  $V_m = 9.0$  V and  $V_m = 10.0$  V, reaching the order of magnitude of  $10^{-11}$  cm<sup>2</sup>. At  $V_m = 1.0$  V it amounts to  $5 \times 10^{-14}$  cm<sup>2</sup> (with an uncertainty of 0.2 orders of magnitude), and at  $V_m = 10.0$  V to  $4 \times 10^{-11}$  cm<sup>2</sup> (with an uncertainty of 0.5 orders of magnitude).

To sum up, the localisation energy of sample 2-QD-B is  $E_{loc} = 900(\pm 20)$  meV, with an associated apparent capture cross-section  $\sigma_{\infty} = 4 \times 10^{-13}$  cm<sup>2</sup> (with an uncertainty of 0.3 orders of magnitude).

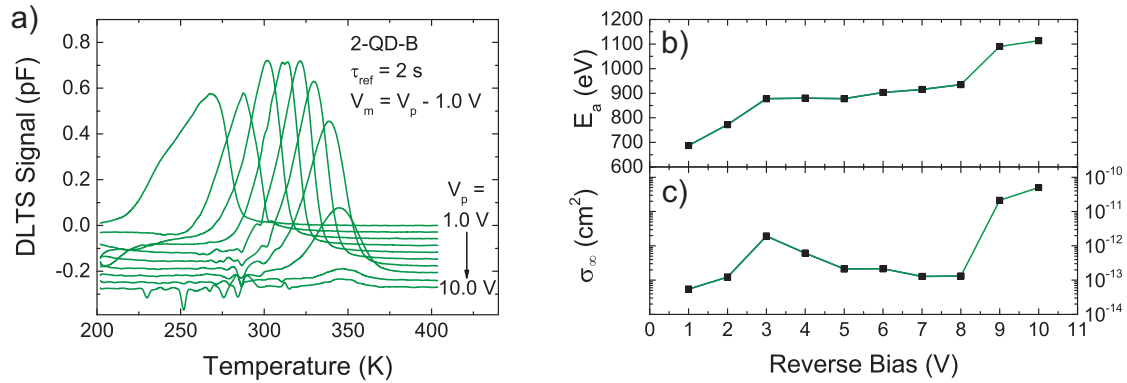


**Figure 7.7.:** Summary of the results of charge-selective DLTS on sample 2-QD-B. (a) DLTS signal for  $\tau_{ref} = 2$  s,  $V_m = 1.0$  V to  $V_m = 10.0$  V,  $V_p = V_m - 1.0$  V (offset for ease of reading). (b) Activation energies and (c) capture cross-sections extracted from the same measurement.

#### 7.4.4. Sample 2-QD-C

Charge-selective DLTS was performed on sample 2-QD-C with measurement voltages ranging from  $V_m = 0.0$  V to  $V_m = 6.0$  V in 1.0 V steps. Fig. 7.8a reports the DLTS spectra for  $\tau_{ref} = 27$  s for the measurement voltages  $V_m = 2.0$  V to  $V_m = 5.0$  V. The other spectra do not present any peaks. A single peak is clearly distinguishable in Fig. 7.8a. It appears around  $T \simeq 305$  K for  $V_m = 2.0$  V and shifts smoothly towards higher temperatures with increasing biases, until it reaches  $T \simeq 325$  K for  $V_m = 5.0$  V. The fact that the peak is only visible in such a small range of measurement voltages indicates that the QDs have in this case only a limited number of bound states. This hypothesis is supported by the fact that a charge-selective DLTS measurement with finer voltage steps (0.5 V) did not improve the results.

The activation energy starts off at  $E_a = 959(\pm 6)$  meV for  $V_m = 2.0$  V and remains approximately the same for  $V_m = 3.0$  V and  $V_m = 4.0$  V. At  $V_m = 5.0$  V it reaches

## 7. GaSb QDs in GaP

$E_a = 1070(\pm 10)$  meV (see Fig. 7.7b), which represents the localisation energy of this sample. The pattern can be interpreted either as two bound states, one with activation energy  $E_a^0 = 1070(\pm 10)$  meV and one with activation energy  $E_a^1 = 960(\pm 10)$  meV, or as a single ensemble-broadened bound state with activation energy  $E_a^0 = 1010(\pm 60)$  meV. In the latter case, the two different activation energies would represent the two opposite “halves” of the Gaussian distribution of energies caused by the broadening (see Sc. 2.4.3). Since the energy 960(±10) meV is measured for several voltages and is not compatible within its uncertainty with 1070(±10) meV, we choose the former interpretation and attribute two bound states to the QDs. Ensemble broadening justifies the fact that the lower-energy level is accessible at several bias voltages.

The apparent capture cross-section (Fig. 7.7c) follows roughly the same trend as the activation energy, starting off at  $\sigma_\infty = 8 \times 10^{-13}$  cm<sup>2</sup> (with an error of 0.1 orders of magnitude) for  $V_m = 2.0$  V, remaining almost constant for  $V_m = 3.0$  V and  $V_m = 4.0$  V, and finally increasing to  $\sigma_\infty = 7 \times 10^{-12}$  cm<sup>2</sup> (with an error of 0.2 orders of magnitude) for  $V_m = 5.0$  V. This pattern confirms the observation on the electronic structure of the QDs made above.

To sum up, the localisation energy of sample 2-QD-C is  $E_{loc} = 1070(\pm 10)$  meV, with an associated apparent capture cross-section  $\sigma_\infty = 7 \times 10^{-12}$  cm<sup>2</sup> (with an uncertainty of 0.2 orders of magnitude).

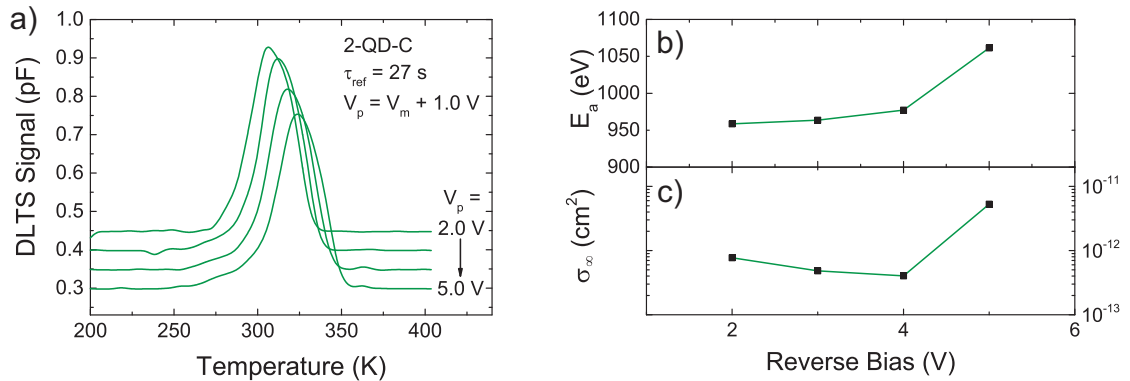


**Figure 7.8.:** Summary of the results of charge-selective DLTS on sample 2-QD-C. (a) DLTS signal for  $\tau_{ref} = 27$  s,  $V_m = 2.0$  V to  $V_m = 5.0$  V,  $V_p = V_m - 1.0$  V (offset for ease of reading). (b) Activation energies and (c) capture cross-sections extracted from the same measurement.

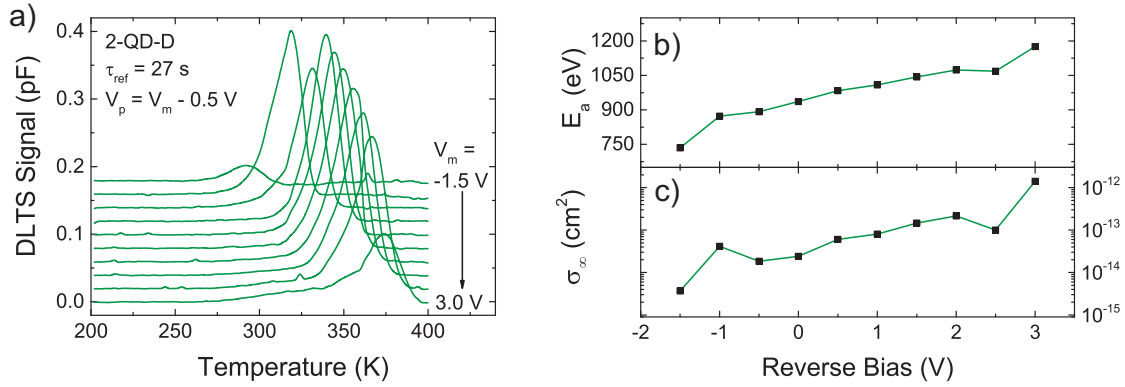


**Figure 7.9.:** Summary of the results of charge-selective DLTS on sample 2-QD-D. (a) DLTS signal for  $\tau_{ref} = 27$  s,  $V_m = -1.5$  V to  $V_m = 3.0$  V,  $V_p = V_m - 0.5$  V (offset for ease of reading). (b) Activation energies and (c) capture cross-sections extracted from the same measurement.

### 7.4.5. Sample 2-QD-D

Charge-selective DLTS was performed on sample 2-QD-D with measurement voltages ranging from  $V_m = -1.5$  V to  $V_m = 4.0$  V in 0.5 V steps. Fig. 7.9a reports the DLTS spectra for  $\tau_{ref} = 27$  s for the measurement voltages  $V_m = -1.5$  V to  $V_m = 3.0$  V. The other spectra are excluded from the analysis because the peaks they present are much smaller and arise at lower temperatures, suggesting that they do not originate from the QDs directly.<sup>2</sup> A single peak is clearly distinguishable in the remaining spectra. It appears around  $T \simeq 290$  K for  $V_m = -1.5$  V and shifts smoothly towards higher temperatures with increasing biases, until it reaches  $T \simeq 375$  K for  $V_m = 3.0$  V. The fact that the peak is only visible in a smaller range of measurement voltages (compared for example to samples 2-QD-A and 2-QD-B) is probably due to a slightly lower doping of the p-layer in which the QDs are embedded (see Fig. 7.1a). Lower dopings do indeed cause the depletion layer to extend further into the p-layer above the QDs. For a sufficiently low doping, the depletion layer can extend to the full 514 nm necessary to cross the QD layer already at a reverse bias  $V = 3.5$  V, as is the case for sample 2-QD-D.

The activation energy starts off at  $E_a = 735(\pm 7)$  meV for  $V_m = -1.5$  V and increases gradually to  $E_a = 1180(\pm 9)$  meV for  $V_m = 3.0$  V (see Fig. 7.9b), which represents the localisation energy of this sample.

The apparent capture cross-section (Fig. 7.9c) follows roughly the same trend as the activation energy, starting off at  $\sigma_\infty = 2 \times 10^{-15}$  cm<sup>2</sup> (with an error of 0.1 orders of

<sup>2</sup>Charge-selective DLTS measurements produce spurious peaks relatively often. Their origin can be traced either to deep defects located in the vicinity of the QDs, or to the effect of ensemble broadening.

## 7. GaSb QDs in GaP

magnitude) for  $V_m = -1.5$  V and reaching  $\sigma_\infty = 1 \times 10^{-12}$  cm<sup>2</sup> (with an error of 0.1 orders of magnitude) for  $V_m = 3.0$  V.

To sum up, the localisation energy of sample 2-QD-D is  $E_{loc} = 1180(\pm 9)$  meV, with an associated apparent capture cross-section  $\sigma_\infty = 1 \times 10^{-12}$  cm<sup>2</sup> (with an uncertainty of 0.1 orders of magnitude).

### 7.4.6. Sample 2-QD-AIP

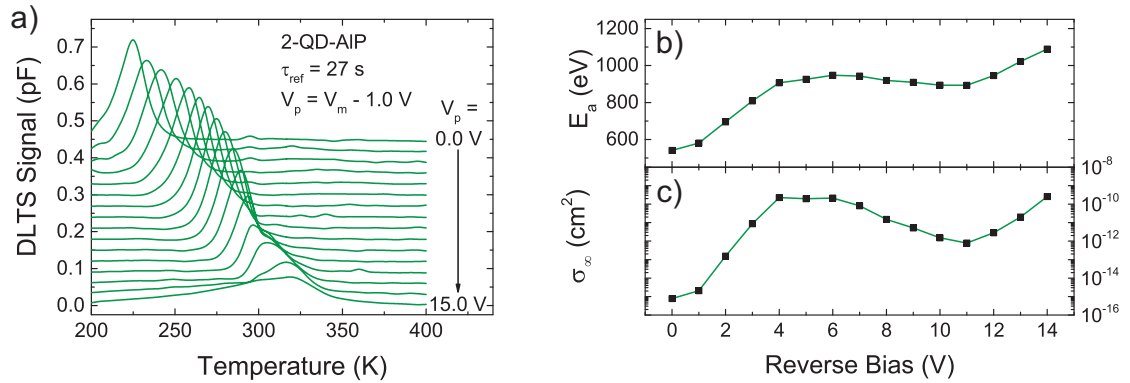


**Figure 7.10.:** Summary of the results of charge-selective DLTS on sample 2-QD-AIP. (a) DLTS signal for  $\tau_{ref} = 27$  s,  $V_m = 0.0$  V to  $V_m = 15.0$  V,  $V_p = V_m - 1.0$  V (offset for ease of reading). (b) Activation energies and (c) capture cross-sections extracted from the same measurement.

Charge-selective DLTS was performed on sample 2-QD-AIP with measurement voltages ranging from  $V_m = 0.0$  V to  $V_m = 15.0$  V in 1.0 V steps. Fig. 7.10a reports the DLTS spectra for  $\tau_{ref} = 27$  s. A single peak is visible around  $T \approx 225$  K for  $V_m = 0.0$  V and shifts smoothly towards higher temperatures with increasing biases, until it reaches  $T \approx 320$  K for  $V_m = 15.0$  V.

Correspondingly, the activation energy starts off at  $E_a = 541(\pm 7)$  meV, increasing gradually until  $V_m = 4.0$  V (see Fig. 7.10b). At this point the activation energy stabilises around  $E_a = 920(\pm 20)$  meV until  $V_m = 12.0$  V, where it starts rising again until  $E_a = 1170(\pm 40)$  meV for  $V_m = 15.0$  V. This rather peculiar behaviour can be interpreted by attributing all measurements for  $4.0$  V  $\leq V_m \leq 12.0$  V to a single (ensemble-broadened) bound state.

The apparent capture cross-section (Fig. 7.10c) follows a similar pattern, even though the variations in the  $V_m = 4.0$ – $12.0$  V range are much larger, spanning two orders of magnitude (between  $2 \times 10^{-12}$  cm<sup>2</sup> and  $2 \times 10^{-10}$  cm<sup>2</sup>). This could reflect the Gaussian distribution of capture probabilities generated by ensemble broadening (see Sc. 2.4.3).

The apparent capture cross-section for  $V_m = 0.0$  V is  $\sigma_\infty = 8 \times 10^{-16}$  cm<sup>2</sup> (with an uncertainty of 0.1 orders of magnitude), and for  $V_m = 15.0$  V it is  $\sigma_\infty = 1 \times 10^{-9}$  cm<sup>2</sup> (with an uncertainty of 0.6 orders of magnitude).

To sum up, the localisation energy of sample 2-QD-AIP is  $E_{\text{loc}} = 1170(\pm 40)$  meV, with an associated apparent capture cross-section  $\sigma_\infty = 1 \times 10^{-9}$  cm<sup>2</sup> (with an uncertainty of 0.6 orders of magnitude). Interestingly, sample 2-QD-AIP presents the largest localisation energy (together with sample 2-QD-D) and capture cross-section, but also by far the largest errors on the estimates. The range of variation of these quantities with the measurement voltage is also the widest among the samples characterised in this work.

## 7.5. Discussion

The characterisation of the GaSb/GaP QDs batch reveals some interesting trends and relations between growth conditions and properties of the QDs. The relations are highlighted in Tab. 7.3, which reports the major results alongside the growth conditions of each sample.

Samples 2-QD-A, 2-QD-B, 2-QD-C, and 2-QD-D all contain a 1.2-ML-thick QD layer. Samples 2-QD-A, 2-QD-B, and 2-QD-C represent a series with increasing QD growth temperature and fixed growth rate  $v_{\text{Ga}} = 0.2$  ML/s, whereas in sample 2-QD-D the temperature was kept at  $T = 470$  °C, but the growth rate was decreased to  $v_{\text{Ga}} = 0.1$  ML/s. The localisation energy increases by 200 meV when the temperature is raised from 430 °C to 450 °C, but remains the same (within the experimental error) when the temperature is increased further to 470 °C. However, the localisation energy does gain an additional 100 meV when the growth rate is reduced. It is known from simulations that larger QDs give rise to higher localisation energies (see Sc. 2.4.2). The pattern can then be explained by the fact that higher temperatures induce on the one hand higher surface mobilities, producing larger QDs; on the other hand lower defect densities, producing QDs of higher structural quality. Furthermore, the reduced growth rate corresponds to a longer growth time, giving the QDs more time to ripen, allowing them to grow even larger.

The estimates for the apparent capture cross-section are reported in Fig. 7.11 alongside their respective uncertainties for ease of comparison. No clear pattern can be evinced from the measurements. However, the AIP layer definitely increases the capture cross-section of several orders of magnitude (with respect to sample 2-QD-D, which is otherwise identical to sample 2-QD-AIP). This is probably due to a sizeable influx of the AIP layer on the geometrical shape of the quantum dots and strain distribution in their vicinity. Moreover, the capture cross-section decreases in the 2-QD-B, 2-QD-C, 2-QD-D series.

## 7. GaSb QDs in GaP

Extrapolating the trend, we would expect the capture cross-section of sample 2-QD-A to be the largest in the series, yet this is not the case. Albeit encouraging, these observations are not sufficient to determine the exact effect of the growth parameters on the capture cross-section. A more systematic study is needed to understand this complex parameter.

On the other hand, a very clear trend is to be seen in the storage time  $\tau$ , which increases from 30 s (with an uncertainty of 0.1 orders of magnitude) for sample 2-QD-A to a staggering 3.9 days (with an uncertainty of 0.04 orders of magnitude) for sample 2-QD-D. This value represents an absolute record for hole storage time at room temperature in QDs, marking an improvement of 3 orders of magnitude over the previous record of 260 s (with an uncertainty of 0.1 orders of magnitude) for In<sub>0.5</sub>Ga<sub>0.5</sub>As/GaAs/AIP/GaP QDs (Ch. 6).

Sample	QD growth			QD properties		
	$d$ (ML)	$T$ ( $^{\circ}$ C)	$v_{\text{Ga}}$ (ML/s)	$E_{\text{loc}}$ (eV)	$\sigma_{\infty}$ (cm <sup>2</sup> )	$\tau$ (at 300 K)
2-QD-A	1.2	430	0.2	0.90( $\pm$ 0.02)	$4 \times 10^{-13}$ (0.3)	30(0.1) s
2-QD-B	1.2	450	0.2	1.11( $\pm$ 0.03)	$4 \times 10^{-11}$ (0.5)	850(0.07) s
2-QD-C	1.2	470	0.2	1.07( $\pm$ 0.01)	$7 \times 10^{-12}$ (0.2)	1100(0.04) s
2-QD-D	1.2	470	0.1	1.18( $\pm$ 0.09)	$1 \times 10^{-12}$ (0.1)	3.9(0.04) d
2-QD-E	1.6	450	0.2	n/a	n/a	n/a
2-QD-AIP	1.2	470	0.1	1.17( $\pm$ 0.04)	$2 \times 10^{-9}$ (0.6)	270(0.08) s
2-Ref	n/a	n/a	0.2	n/a	n/a	n/a

**Table 7.3.:** Summary of all localisation energies  $E_{\text{loc}}$ , apparent capture cross-sections  $\sigma_{\infty}$ , and storage times at room temperature for holes  $\tau$  of the GaSb/GaP QDs batch, alongside the respective growth conditions (thickness of the QD layer  $d$ , growth temperature  $T$ , and growth rate expressed as Ga flux  $v_{\text{Ga}}$ ). The uncertainties on  $\sigma_{\infty}$  and  $\tau$  are reported in orders of magnitude in parentheses. Samples 2-QD-E and 2-Ref did not present any peaks in the charge-selective DLTS measurements.

Interestingly, sample 2-QD-E does not present any peaks either in conventional DLTS or in charge-selective DLTS, in spite of the fact that the growth conditions are very similar to sample 2-QD-B, the only difference being the thicker QD layer (1.6 ML instead of 1.2 ML). The lack of signal could be caused by plastic relaxation of the QDs at a thickness  $d = 1.6$  ML or to physical damage of the sample during the cooling process.<sup>3</sup> The experiments carried out in this work do not allow one hypothesis to be chosen over the other.

Sample 2-QD-AIP shows a very different behaviour than the other samples, being the only one where the QDs are capped with AIP. Since it is grown under the same conditions

<sup>3</sup>The sample appeared intact upon visual inspection. However, this does not rule out damage at the microscopic level.

as sample 2-QD-D and presents the same localisation energy, it is safe to assume that the QDs are identical in the two samples. The AIP cap, however, seems to modify the QDs, increasing their apparent capture cross-section by 3 orders of magnitude (2 orders of magnitude at the least, accounting for the uncertainty). Correspondingly, the storage time is reduced by 3 orders of magnitude with respect to sample 2-QD-D.

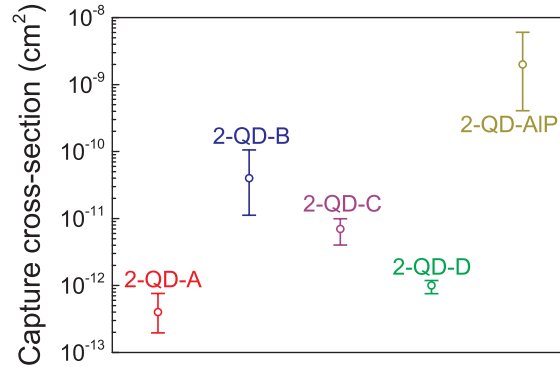


**Figure 7.11.:** Apparent capture cross-sections measured on the GaSb/GaP QDs samples with their respective uncertainties.

The AIP cap seems to have an effect also on the internal electronic structure of the QDs. Comparison of Fig. 7.9b and Fig. 7.10b shows that the activation energies in sample 2-QD-AIP vary over a much wider range (541–1170 meV, as opposed to 735–1180 meV for sample 2-QD-D), and that the QDs are detectable over a much wider interval of biases (0.0–15.0 V, as opposed to -1.5–3.0 V for sample 2-QD-D). This indicates that the QDs in sample 2-QD-AIP have more bound states. The exact quantification of the number of bound states is however prevented by ensemble broadening, which makes the observation of single levels impossible.

The highest localisation energy measured in the batch ( $1.18(\pm 0.09)$  eV) is still 0.22 eV lower than the projected localisation energy of 1.4 eV [56, 155, 156]. This discrepancy is due to intermixing of P and Sb in the dots, which is not accounted for in simulations (see Sc. 2.4.2). The degree of intermixing can be easily estimated using the ratio of mismatch to the expected result:  $0.22 \text{ eV} / 1.4 \text{ eV} = 16\%$ . This result is compatible with the HAADF-STEM measurement — and the corresponding EDX maps — reported in Sc. 7.1. Fig. 7.2d proves that P is present inside the QDs, and Fig. 7.2e indicates that Sb is concentrated on the edge of the QDs. Once averaged over the whole QD, the intermixing could well amount to 16%.

A more accurate estimate can be extracted from the strain map analysis of the HAADF-

## 7. GaSb QDs in GaP

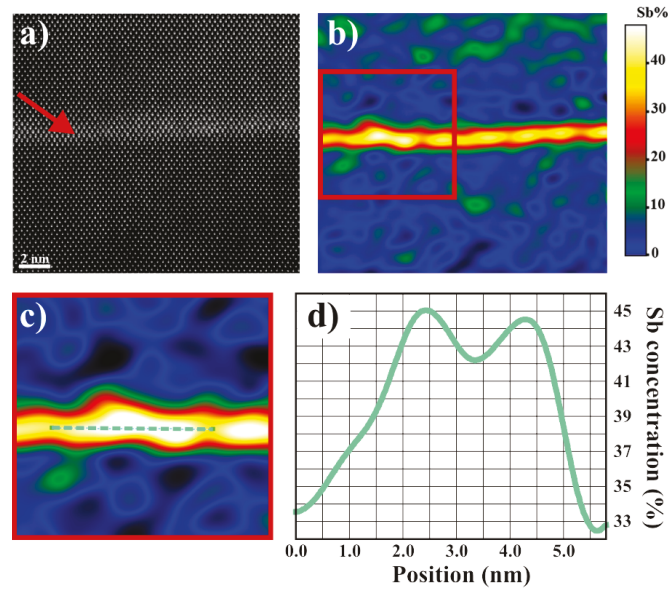


**Figure 7.12.:** (a) HAADF-STEM image of the QD layer of sample 2-QD-D. The QDs are visible as a stripe of lighter contrast, marked by the red arrow. (b) Strain map of the same area of the structure revealing concentrations of Sb up to  $\sim 45\%$  inside the QDs. (c) Strain map around a single QD corresponding to the red box in (b). (d) Sb concentration along the dashed turquoise line in (c), drawn across the QD in the plane of the QD layer. (Reprint from [153]).

STEM images [160]. Fig. 7.12a shows a HAADF-STEM micrograph of the region surrounding the QD layer, which is visible as a region of lighter contrast. The strain map of the same region is shown in Fig. 7.12b. It was generated by assuming that the maximum deformation along the growth axis corresponds to the 11.8% lattice mismatch between GaSb and GaP. The QDs are identifiable in the strain map as regions of higher strain. Fig. 7.12c provides a zoom-in around one such area, whereas Fig. 7.12d shows the Sb concentration on the turquoise path drawn across the QD in Fig. 7.12c. The Sb concentration ranges from 32.5% at the edge of the QD to 45% inside of it. Similar analyses were carried out on several QDs, revealing maximum Sb concentrations between 40% and 45%. This corresponds to an Sb deficit of 5%–10%, which translates to a degree of P/Sb intermixing of 10%–20%, in good agreement with the estimate derived from the localisation energy.

As a final remark, the measured localisation energy of 1.18 eV would be sufficient for non-volatility provided that the capture cross-section was  $\sigma_{\infty} \leq 2 \times 10^{-15} \text{ cm}^2$ , which is an unlikely figure for the capture cross-section of self-organised QDs, albeit not an

impossible one.<sup>4</sup> Conversely, the measured capture cross-section of  $1 \times 10^{-12} \text{ cm}^2$  would yield a storage time longer than 10 years for activation energies  $E_a \geq 1.34 \text{ eV}$ , which is lower than the estimate for the localisation of GaSb/GaP QDs without P/Sb intermixing. The GaSb/GaP QDs system might in other words be able to achieve non-volatility just by increasing the Sb content in the QDs. Alternatively, an AIP barrier embedded below the QD layer would increase the localisation energy by  $\sim 0.5 \text{ eV}$  (see Ch. 6), bringing the total localisation energy to ca.  $1.68 \text{ eV}$  (see Ch. 8 for further details).

---

<sup>4</sup>For example, Marent et al. measured a capture cross-section  $\sigma_\infty = 4 \times 10^{-15} \text{ cm}^2$  for InAs QDs in  $\text{Al}_{0.9}\text{Ga}_{0.1}\text{As}$  [14, 126].

## Summary

- IEMN Lille is one of the first laboratories able to achieve growth of GaSb QDs in GaP. The electronic properties of the novel QD system were characterised for the first time in this work.
- Seven GaSb/GaP QDs samples were characterised in this work. The samples can be divided in three groups:
  1. Samples 2-QD-A, 2-QD-B, 2-QD-C, 2-QD-D, and 2-QD-E all share the same epitaxial structure, namely GaSb QDs embedded in a GaP p-n<sup>+</sup> diode. The growth parameters used for the QD layer (i.e. growth temperature, layer thickness and growth rate) were slightly modified for each sample in order to study their effect on activation energy, apparent capture cross-section, and storage time.
  2. Sample 2-QD-AIP is identical to sample 2-QD-D, but a thin layer of AIP is grown atop the QD layer to study its effect on the underlying QDs.
  3. Sample 2-Ref, the reference sample, is a simple GaP p-n<sup>+</sup> diode.
- The localisation energy is lowest for the QDs grown at the lowest temperature ( $T = 430\text{ °C}$  in sample 2-QD-A). The localisation energies of all other samples are compatible within their uncertainties. We conclude that temperature is the only parameter among the ones tested that influences the localisation energy. In particular, the localisation energy is maximised for all temperatures greater than  $450\text{ °C}$ .
- The apparent capture cross-section does not show a clear trend. The AIP layer has the clear effect on the capture cross-section of increasing it by several orders of magnitude, probably by modifying the geometrical shape of the quantum dots and the strain distribution in their vicinity. Moreover, higher temperatures and smaller growth rates seem to be associated with smaller capture cross-sections. A more systematic study is required to achieve clear results on the relation between growth parameters and apparent capture cross-section.
- The storage time at room temperature shows a sharp increase across the 2-QD-A, 2-QD-B, 2-QD-C, 2-QD-D series from 30 s to 3.9 days. Sample 2-QD-AIP demonstrates a much shorter storage time than sample 2-QD-D (270 s).
- The longest hole storage time at room temperature of the sample set — and also the longest storage time at room temperature ever recorded for quantum dots — is 3.9 days (with an uncertainty of 0.04 orders of magnitude). The result was obtained for sample 2-QD-D, which has a hole localisation energy of  $1.18(\pm 0.09)\text{ eV}$  and an apparent capture cross-section of  $1 \times 10^{-12}\text{ cm}^2$  (with an uncertainty of 0.1 orders of magnitude). This storage time represents an improvement of 3 orders of magnitude over the results of Ch. 6, and of 5 orders of magnitude over the previous record value of 1.6 s (for InAs/Al<sub>0.9</sub>Ga<sub>0.1</sub>As QDs).
- The growth parameters for the QD layer which yield the longest storage time are: thickness  $d = 1.2\text{ ML}$ , temperature  $T = 470\text{ °C}$ , growth rate  $v_{\text{Ga}} = 0.1\text{ ML/s}$ . As far as this work is concerned, these are to be regarded as the optimal parameters for the growth of GaSb QDs in GaP.

## 8. Conclusions and Outlook

La miré sin comprender, aunque como un nadador solitario y exhausto la verdad poco a poco se fue abriendo paso en el mar negro de mi ignorancia.

---

*(Roberto Bolaño Ávalos)*

The aim of this work was to extend the storage time for holes in self-organised quantum dots, striving towards the long-term goal of developing a quantum-dot-based non-volatile memory. The localisation energy of the quantum dots was determined using both conventional and charge-selective DLTS measurements, after a pre-characterisation carried out through C–V profiling. The DLTS measurements provided estimates for the localisation energy and apparent capture cross-section of holes in the quantum dots. These two quantities were then used to extrapolate the storage time at room temperature.

Basing upon previous research, the most promising path towards non-volatility was found to be the implementation of different material systems for the fabrication of the quantum dots. The localisation energies and storage times at room temperature for holes in self-organised quantum dots of different materials are reported in Fig. 8.1 (and again in Fig. 8.2 alongside the references to the corresponding publications). The black dots in Fig. 8.1 represent data available in literature prior to the beginning of the present investigation. With the exception of Ge/Si QDs and  $\text{In}_{0.25}\text{Ga}_{0.75}\text{As}/\text{GaAs}/\text{GaP}$  QDs, all data refers to quantum dots grown in a GaAs or AlGaAs matrix. InAs or GaSb was used for the QDs, with GaSb QDs demonstrating the highest localisation energy (800 meV for GaSb/ $\text{Al}_{0.3}\text{Ga}_{0.7}\text{As}$  QDs), and InAs QDs demonstrating the longest storage time (1.6 s at room temperature for InAs/ $\text{Al}_{0.9}\text{Ga}_{0.1}\text{As}$  QDs). As far as arsenide-based heterostructures are concerned, the storage time at room temperature could be increased by 10 orders of magnitude: from the 0.5 ns of InAs/GaAs QDs to the 1.6 s of InAs/ $\text{Al}_{0.9}\text{Ga}_{0.1}\text{As}$  QDs.

In spite of the considerable technological difficulties connected with the epitaxial growth and doping of GaP, the decision was made to use it as a matrix material because

## 8. Conclusions and Outlook

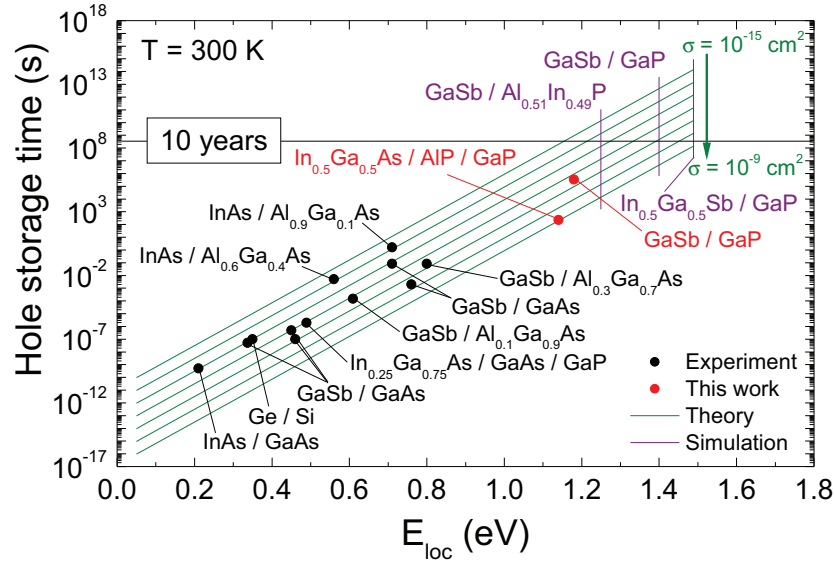


**Figure 8.1.:** Summary of all storage times for holes at room temperature measured as of yet in self-organised quantum dots, plotted against the respective localisation energies. Each point is marked with the material system on which it was measured.

of the high projected localisation energies: 1.1 eV for the  $\text{In}_{0.5}\text{Ga}_{0.5}\text{As}/\text{AIP}/\text{GaP}$  QDs system [56, 161] and 1.4 eV for the  $\text{GaSb}/\text{GaP}$  QDs system [56, 155, 156]. As a first step into this novel paradigm,  $\text{In}_{0.25}\text{Ga}_{0.75}\text{As}/\text{GaAs}/\text{GaP}$  QDs were grown by MOCVD at TU Berlin. The localisation energy of the QDs in that sample could not be determined because of the technological challenge of achieving a high p doping in GaP, but a lower bound could be placed at 489 meV (mean activation energy of the QDs determined by conventional DLTS). The promising results led to the growth of the first batch of samples characterised in this work.

The first batch was composed of three samples: one containing  $\text{In}_{0.5}\text{Ga}_{0.5}\text{As}$  QDs grown on top of a GaAs interlayer and an AIP barrier in GaP, one containing only the AIP barrier, and one reference sample (a simple p–n diode). The localisation energy of the QDs + barrier system was determined as  $1.15(\pm 0.03)$  eV, with an associated apparent capture cross-section of  $8 \times 10^{-10} \text{ cm}^2$  (with an uncertainty of 0.4 orders of magnitude). The corresponding storage time at room temperature was 260 s (with an uncertainty of 0.1 orders of magnitude). This figure constitutes the first breakthrough achieved in this work, marking an improvement of 2 orders of magnitude over the previous record value. This value corresponds to the lower red dot in Fig. 8.1.

The second batch of samples was grown by MBE at IEMN in Lille and was composed of seven samples: five of them containing GaSb QDs grown in a GaP matrix under different growth conditions, one sample with a thin AlP layer embedded on top of the QDs, and one reference sample (again a simple p–n diode). The sample series granted some insights into the relation between growth conditions, localisation energy, and storage time, allowing the identification of the optimal growth conditions as:

QD layer thickness: 1.2 ML  
 QD growth temperature: 470 °C  
 Growth rate:  $v_{\text{Ga}} = 0.1 \text{ ML/s}$

These growth conditions resulted in a localisation energy of  $1.18(\pm 0.09) \text{ eV}$ , with an associated apparent capture cross-section of  $1 \times 10^{-12} \text{ cm}^2$  (with an uncertainty of 0.1 orders of magnitude). The storage time at room temperature of 3.9 days (with an uncertainty of 0.04 orders of magnitude) represents a second breakthrough, extending the storage time of further 3 orders of magnitude (top red dot in Fig. 8.1).

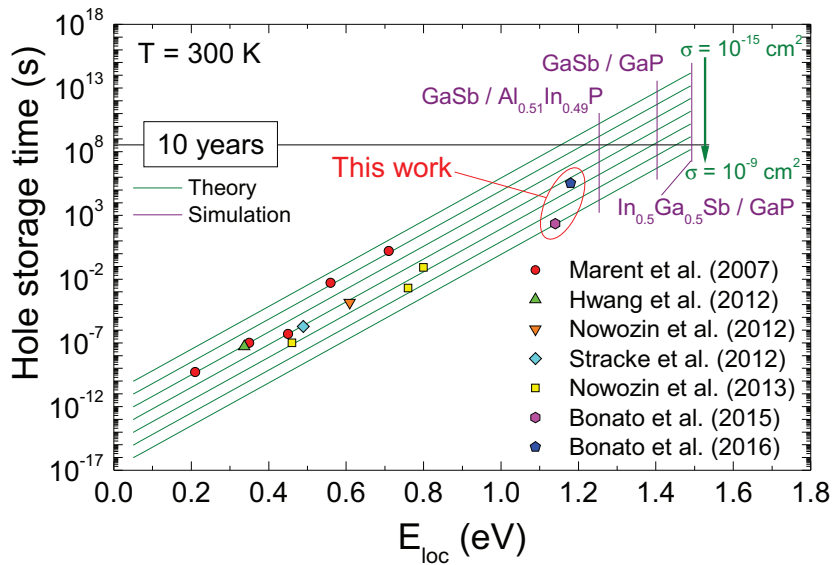


**Figure 8.2.:** Summary of all storage times for holes at room temperature measured as of yet in self-organised quantum dots, plotted against the respective localisation energies. The data was published in [14, 126–128, 145, 147, 153].

To sum up, over the course of this work we were able to prove that the hole storage time in self-organised quantum dots can be extended by several orders of magnitude by means

## 8. Conclusions and Outlook

of relatively simple changes in the material system employed to manufacture the heterostructure. In particular, two major steps forward were made: a first increase of 2 orders of magnitude with  $\text{In}_{0.5}\text{Ga}_{0.5}\text{As}/\text{AlP}/\text{GaP}$  QDs, and a second increase of 3 orders of magnitude with  $\text{GaSb}/\text{GaP}$  QDs. These are the longest hole storage times at room temperature ever demonstrated in self-organised quantum dots. The present thesis also represents — to the best of our knowledge — the first ever attempt at electrical characterisation of these material systems. The measured hole localisation energies ( $1.15(\pm 0.03)$  eV and  $1.18(\pm 0.09)$  eV, respectively) are also the highest hitherto demonstrated in self-organised quantum dots.

This work also highlights the crucial importance of the apparent capture cross-section for the storage time. The family of straight lines in Fig. 8.1 and Fig. 8.2 (plotted in green) depict the dependence of the storage time on the localisation energy, i.e. the following equation:

$$\tau = \frac{1}{\gamma_p T^2 \sigma_p^\infty} \exp\left(\frac{E_{\text{loc}}^p}{k_B T}\right), \quad (8.1)$$

where  $\sigma_p^\infty$  is varied as a parameter in the interval of usual apparent capture cross-section for self-organised QDs ( $\sim 10^{-15}$ – $10^{-9}$  cm<sup>2</sup>). Since the storage time is inversely proportional to the capture cross-section, variations over such a wide range reflect in variations over a similar range for the storage time. This is demonstrated very clearly by the fact that the storage times of the material systems characterised in this work differ by 3 orders of magnitude, even though the localisation energies differ by only 30 meV. The capture cross-section is a complex parameter which depends on several factors like geometrical size of the QDs, interaction of the QDs with the surrounding matrix, or Auger scattering and phonon coupling. Attempts at engineering the capture cross-section have yet to succeed, but the study carried out on the  $\text{GaSb}/\text{GaP}$  QDs series constitutes a promising first step towards a thorough understanding of the topic.

These considerations and results lead to the following recommendations for further extending the storage time in self-organised quantum dots:

- **Increased Sb content in GaSb/GaP QDs:** The projected localisation energy for  $\text{GaSb}/\text{GaP}$  QDs is 1.4 eV, 0.22 eV larger than the one measured in this work. The discrepancy is probably due to the high P content in the QDs. Achieving stoichiometrically pure  $\text{GaSb}$  QDs would increase the localisation energy and — assuming that the capture cross-section remains the same — yield a storage time at room temperature of 90 years.
- **New materials:** As illustrated by the purple vertical lines in Fig. 8.1 and Fig. 8.2,

other phosphide-based material systems also offer very large localisation energies. Specifically, GaSb QDs in  $\text{Al}_{0.51}\text{In}_{0.49}\text{P}$  should present a localisation energy of 1.25 eV, alongside the technologically interesting possibility of growing  $\text{Al}_{0.51}\text{In}_{0.49}\text{P}$  lattice-matched on GaAs. Alternatively,  $\text{In}_{0.5}\text{Ga}_{0.5}\text{Sb}/\text{GaP}$  QDs have an even higher projected localisation energy of 1.5 eV. Depending on the capture cross-section, both of these systems might be suitable for achieving non-volatility.

- **AIP barrier:** The characterisation of the  $\text{In}_{0.5}\text{Ga}_{0.5}\text{As}/\text{AIP}/\text{GaP}$  QDs batch demonstrated that an AIP barrier placed under the QDs can increase the localisation energy of the system by 0.5 eV. Such a barrier has a negligible effect on the crystalline structure,<sup>1</sup> which makes its implementation in other GaP-based structures straightforward. The GaSb/GaP QDs sample characterised in this work could easily be re-grown with the addition of the barrier, increasing the localisation energy to ca. 1.68 eV. In this case, non-volatility would be achieved for any  $\sigma_{\infty} \leq 5 \times 10^{-7} \text{ cm}^2$ .
- **Capture cross-section engineering:** The localisation energy achieved in the GaSb/GaP QDs would already be sufficient for non-volatility, provided that the capture cross-section be decreased to less than  $2 \times 10^{-15} \text{ cm}^2$ . Unfortunately, no method has yet been discovered to reliably predict the apparent capture cross-section based on the growth parameters. However, the present work represents the starting point for further research into this kind of technology, which could prove very beneficial for increasing the storage time.

The remaining gap of 3 orders of magnitude towards non-volatility in self-organised quantum dots pales in comparison to the 14 orders of magnitude already gained with respect to InAs/GaAs QDs. Considering the simplicity of the recommendations made above, a few further growth iterations should be sufficient to finally achieve our ambitious goal.

---

<sup>1</sup>The lattice mismatch of AIP to GaP is only 0.02% [56].



# Appendix A.

## Error analysis of DLTS measurements

This chapter discusses the experimental error associated with the determination of activation energy and capture cross-section via the double-boxcar method (see Sc. 5.3.3). The main ideas underlying this discussion are taken from [162].

The DLTS spectra are analysed graphically by identifying for each reference time  $\tau_{\text{ref}}$  the temperature  $T_{\text{peak}}$  at which the maximum of the respective spectrum occurs. The set of  $(T_{\text{peak}}^i, \tau_{\text{ref}}^i)$  pairs thus obtained is fitted to the linearised form of Eq. 3.16:

$$\ln(T_{\text{peak}}^2 \tau_{\text{ref}}) = \frac{E_a}{1000k_B} \cdot \frac{1000}{T_{\text{peak}}} - \ln(\gamma\sigma_\infty), \quad (\text{A.1})$$

where all quantities refer to holes (so  $E_a = E_a^h$ ,  $\gamma = \gamma_p^{\text{GaP}} = 2.57 \times 10^{25}$ , and  $\sigma_\infty = \sigma_p^\infty$ ). For Boltzmann's constant we use  $k_B = 8.62 \times 10^{-5}$  eV/K. The activation energy can then be calculated from the slope of the fit and the apparent capture cross-section from its intercept with the  $y$  axis.

The experimental error is attributed to  $E_a$  and  $\sigma_\infty$  using a statistical approach. The method is illustrated in the first section of this chapter by reporting in detail and commenting the error analysis for sample 1-QD (see Ch. 6). The other analyses were carried out in a similar fashion and are only summarised in the following sections.

### A.1. $\text{In}_{0.5}\text{Ga}_{0.5}\text{As}/\text{AlP}/\text{GaAs}/\text{GaSb}$ QDs

#### A.1.1. Sample 1-QD: Charge-selective DLTS — Ground state

In principle, the standard error derived from the linear fit represents the experimental error on  $E_a$  and  $\sigma_\infty$ . In the case of DLTS analysis, however, the main source of error is the uncertainty in the determination of the position of the maxima via graphical analysis. The uncertainty can be minimised by repeating the graphical analysis several times and averaging over the repetitions. If the set of results follows the Gaussian distribution,

the mean value resembles the best estimate and the standard deviation resembles the uncertainty [162].

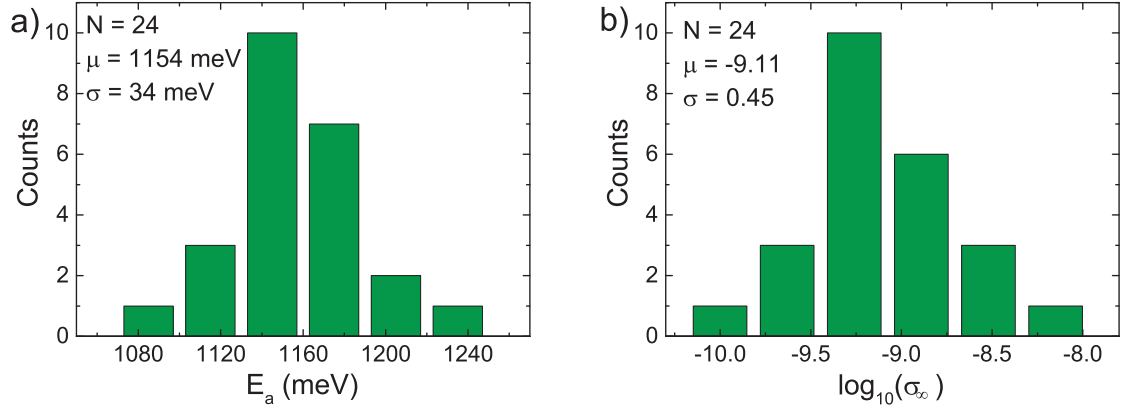


**Figure A.1.:** Histograms representing the results obtained for (a) the activation energy and (b) the apparent capture-cross section from  $N = 24$  evaluations of charge-selective DLTS on the ground state of sample 1-QD.  $\mu$  is the mean value of the set and  $\sigma$  its standard deviation. The histograms resemble the Gaussian distribution.

Let us look at the results of charge-selective DLTS performed on sample 1-QD using a measurement voltage  $V_m = 5.0$  V and a pulse voltage  $V_p = 4.5$  V (see Sc. 6.5). The graphical analysis was repeated  $N = 24$  times. Histograms of the activation energies  $E_a$  and logarithmised<sup>1</sup> capture cross-sections  $\log \sigma_{\infty}$  extracted from the analyses are reported in Fig. A.1a and Fig. A.1b, respectively. The histograms show clearly that the data set does indeed follow a Gaussian distribution, which justifies the use of this statistical approach for the assessment of the experimental uncertainty.

The results of the analysis (reported in Tab. A.1) translate to a localisation energy  $E_a = 1.15(\pm 0.03)$  eV and an apparent capture cross-section  $\sigma_{\infty} = 8 \times 10^{-10}$  cm<sup>2</sup> (with an uncertainty of 0.4 orders of magnitude).

The storage time is extrapolated from  $E_a$  and  $\sigma_{\infty}$  using Eq. 6.1:

$$\tau = \frac{1}{\gamma \cdot T^2 \cdot \sigma_{\infty}} \exp\left(\frac{E_a}{k_B T}\right). \quad (\text{A.2})$$

In principle, the experimental error could be propagated from  $E_a$  and  $\sigma_{\infty}$  to  $\tau$ . However, Fig. A.2a shows that  $E_a$  and  $\sigma_{\infty}$  are highly correlated ( $r = 0.9997$ , where  $r = 1$  indicates complete correlation). Since the errors  $\Delta E_a$  and  $\Delta \sigma_{\infty}$  are not independent, they partially

<sup>1</sup>The statistical analysis has to be carried out on the logarithm of  $\sigma_{\infty}$  because  $\sigma_{\infty}$  is calculated by exponentiation, which skews the Gaussian distribution.

Sample 1-QD — Ground state (I)				
Parameter	Mean value $\mu$	St. dev. $\sigma$	Min. value	Max. value
$E_a$	1154.4 meV	34.0 meV	1090.7 meV	1222.7 meV
$\log_{10} \sigma_\infty$	-9.111	0.445	-9.947	-8.209
$\log_{10} \tau$	2.441	0.126	2.208	2.687

**Table A.1.:** Mean value  $\mu$ , standard deviation  $\sigma$ , minimum value, and maximum value of:  $E_a$ ,  $\log_{10} \sigma_\infty$ , and  $\log_{10} \tau$ ; from  $N = 24$  evaluations of the charge-selective DLTS measurement performed on sample 1-QD with  $V_m = 5.0$  V,  $V_p = 4.5$  V.

cancel each other out when Eq. A.2 is used. Their direct propagation to  $\tau$  would therefore lead to a gross overestimate of the error  $\Delta\tau$ . This problem can be circumvented by noting that  $\log_{10} \tau$  also follows a Gaussian distribution (see Fig. A.2b). The statistical approach can then again be used to estimate the uncertainty on  $\tau$ . The storage time amounts then to  $\tau = 280$  s (with an uncertainty of 0.1 orders of magnitude).

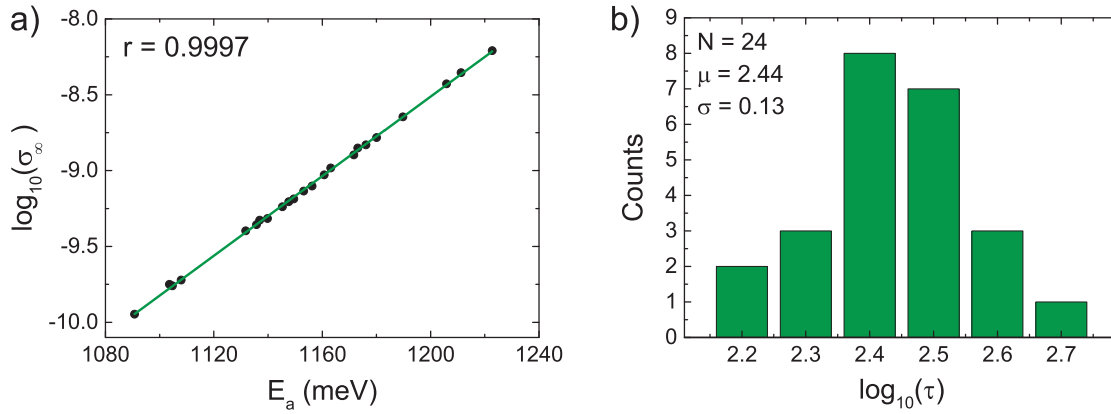


**Figure A.2.:** (a) Plot of  $\log_{10} \sigma_\infty$  against  $E_a$ . The quantities correlate almost perfectly ( $r = 0.9997$ ). (b) Histogram of the storage times obtained from  $N = 24$  evaluations of charge-selective DLTS on the ground state of sample 1-QD. The histogram resembles the Gaussian distribution.

As mentioned in Ch. 6, however, the results of the analysis of the charge-selective DLTS spectra acquired on sample 1-QD with  $V_m = 4.5$  V and  $V_p = 4.0$  V are almost identical to those acquired at the following bias step ( $V_m = 5.0$  V,  $V_p = 4.5$  V):  $E_a = 1.15(\pm 0.02)$  eV,  $\sigma_\infty = 9 \times 10^{-10}$  cm<sup>2</sup> (with an uncertainty of 0.3 orders of magnitude), and  $\tau = 230$  s (with an uncertainty of 0.08 orders of magnitude) (results of the statistical analysis in Tab. A.2). We conclude that the results actually come from the same (ensemble broadened) QD level and are therefore to be aggregated and analysed together.

The results of the aggregated analysis are reported in Tab. A.3 and yield an activation

Sample 1-QD — Ground state (II)				
Parameter	Mean value $\mu$	St. dev. $\sigma$	Min. value	Max. value
$E_a$	1154.9 meV	23.2 meV	1111.1 meV	1192.4 meV
$\log_{10} \sigma_\infty$	-9.027	0.306	-9.588	-8.157
$\log_{10} \tau$	2.367	0.085	2.192	2.487

**Table A.2.:** Mean value  $\mu$ , standard deviation  $\sigma$ , minimum value, and maximum value of:  $E_a$ ,  $\log_{10} \sigma_\infty$ , and  $\log_{10} \tau$ ; from  $N = 16$  evaluations of the charge-selective DLTS measurement performed on sample 1-QD with  $V_m = 4.5$  V,  $V_p = 4.0$  V.

energy  $E_a = 1.15(\pm 0.03)$  eV, a capture cross-section  $\sigma_\infty = 8 \times 10^{-10}$  cm<sup>2</sup> (with an uncertainty of 0.4 orders of magnitude), and  $\tau = 260$  s (with an uncertainty of 0.1 orders of magnitude). Considering that this is the highest activation energy obtained with charge-selective DLTS (with the exception of  $V_m = 5.5$  V,  $V_p = 5.0$  V, which is an artefact; see discussion in Ch. 6), it is attributed to the hole ground state of the QDs and is therefore the localisation energy for holes of In<sub>0.5</sub>Ga<sub>0.5</sub>As/AIP/GaAs/GaP QDs. The storage time at room temperature for holes in said dots is, within the uncertainty of 0.1 orders of magnitude, 260 s.

Sample 1-QD — Ground state (aggregated)				
Parameter	Mean value $\mu$	St. dev. $\sigma$	Min. value	Max. value
$E_a$	1154.6 meV	29.8 meV	1090.7 meV	1222.7 meV
$\log_{10} \sigma_\infty$	-9.077	0.393	-9.947	-8.209
$\log_{10} \tau$	2.411	0.116	2.192	2.687

**Table A.3.:** Mean value  $\mu$ , standard deviation  $\sigma$ , minimum value, and maximum value of:  $E_a$ ,  $\log_{10} \sigma_\infty$ , and  $\log_{10} \tau$ ; from the aggregated evaluation of the charge-selective DLTS measurements performed on sample 1-QD with  $V_m = 5.0$  V,  $V_p = 4.5$  V and  $V_m = 4.5$  V,  $V_p = 4.0$  V.

### A.1.2. Sample 1-QD: Charge-selective DLTS — Shallowest state

The charge-selective DLTS measurements performed on sample 1-QD with measurement biases ranging from  $V_m = 0.0$  V to  $V_m = 3.0$  V ( $V_p = V_m - 0.5$  V) all yield activation energies in a small interval around the mean value  $\mu = 902.3$  meV (see Tab. A.4). We therefore attribute all of them to the shallowest bound level of the QDs + barrier system and aggregate them for evaluation, which results in an activation energy  $E_a = 900(\pm 10)$  meV and an apparent capture cross-section  $\sigma_\infty = 4 \times 10^{-13}$  cm<sup>2</sup> (with an uncertainty of 0.1 orders of magnitude). The associated storage time at room temperature ( $\tau = 30$  s, with

an uncertainty of 0.06 orders of magnitude) has little physical significance.

Sample 1-QD — Shallowest state				
Parameter	Mean value $\mu$	St. dev. $\sigma$	Min. value	Max. value
$E_a$	902.3 meV	10.7 meV	877.7 meV	915.2 meV
$\log_{10} \sigma_\infty$	-12.386	0.148	-12.672	-12.173
$\log_{10} \tau$	1.482	0.060	1.353	1.554

**Table A.4.:** Mean value  $\mu$ , standard deviation  $\sigma$ , minimum value, and maximum value of:  $E_a$ ,  $\log_{10} \sigma_\infty$ , and  $\log_{10} \tau$ ; from  $N = 16$  evaluations of the charge-selective DLTS measurements performed on sample 1-QD with measurement biases ranging from  $V_m = 0.0$  V to  $V_m = 3.0$  V ( $V_p = V_m - 0.5$  V), aggregated.

### A.1.3. Sample 1-QD: Conventional DLTS

The conventional DLTS measurement on sample 1-QD yields an activation energy  $E_a = 580(\pm 10)$  meV, an apparent capture cross-section  $\sigma_\infty = 2 \times 10^{-17}$  cm<sup>2</sup> (with an uncertainty of 0.1 orders of magnitude), and a storage time at room temperature  $\tau = 3$  s (with an uncertainty of 0.2 orders of magnitude). These values represent the average over all bound states of the system. The ratio of the localisation energy to the average activation energy is  $E_{\text{loc}}/\overline{E_a} = 1.98$ .

Sample 1-QD — Conventional DLTS				
Parameter	Mean value $\mu$	St. dev. $\sigma$	Min. value	Max. value
$E_a$	582.3 meV	13.2 meV	548.2 meV	599.8 meV
$\log_{10} \sigma_\infty$	-16.731	0.127	-16.939	-16.527
$\log_{10} \tau$	0.450	0.156	-0.119	0.541

**Table A.5.:** Mean value  $\mu$ , standard deviation  $\sigma$ , minimum value, and maximum value of:  $E_a$ ,  $\log_{10} \sigma_\infty$ , and  $\log_{10} \tau$ ; from  $N = 16$  evaluations of the conventional DLTS measurement performed on sample 1-QD with  $V_m = 7.0$  V,  $V_p = -1.0$  V.

### A.1.4. Sample 1-Barr: Charge-selective DLTS

The charge-selective DLTS measurements performed on sample 1-Barr with measurement biases ranging from  $V_m = 0.0$  V to  $V_m = 7.0$  V ( $V_p = V_m - 1.0$  V) all yield activation energies in a small interval around the mean value  $\mu = 524.3$  meV (see Tab. A.6), as expected for a simple AIP barrier, which only gives rise to one bound state. The evaluation is carried out on the aggregated set of results, giving an activation energy  $E_a = 524(\pm 7)$  meV,

Appendix A. Error analysis of DLTS measurements

an apparent capture cross-section  $\sigma_\infty = 2 \times 10^{-16} \text{ cm}^2$  (with an uncertainty of 0.1 orders of magnitude), and a storage time at room temperature  $\tau = 0.03 \text{ s}$  (with an uncertainty of 0.03 orders of magnitude).

Parameter	Mean value $\mu$	St. dev. $\sigma$	Min. value	Max. value
$E_a$	524.3 meV	6.8 meV	513.0 meV	538.7 meV
$\log_{10} \sigma_\infty$	-15.654	0.127	-15.903	-15.420
$\log_{10} \tau$	-1.601	0.027	-1.628	-1.536

**Table A.6.:** Mean value  $\mu$ , standard deviation  $\sigma$ , minimum value, and maximum value of:  $E_a$ ,  $\log_{10} \sigma_\infty$ , and  $\log_{10} \tau$ ; from  $N = 16$  evaluations of the charge-selective DLTS measurements performed on sample 1-Barr with measurement biases ranging from  $V_m = 0.0 \text{ V}$  to  $V_m = 7.0 \text{ V}$  ( $V_p = V_m - 1.0 \text{ V}$ ), aggregated.

Sample	$E_{\text{loc}}$	$\sigma_\infty$	$\tau$ (at 300 K)
1-QD	1.15( $\pm 0.03$ ) eV	$8 \times 10^{-10}$ (0.4) $\text{cm}^2$	260(0.1) s
1-Barr	0.524( $\pm 0.007$ ) eV	$2 \times 10^{-16}$ (0.1) $\text{cm}^2$	0.03(0.03) s

**Table A.7.:** Summary of the localisation energies, apparent capture cross-sections, and storage times at room temperature of the samples of the  $\text{In}_{0.5}\text{Ga}_{0.5}\text{Sb}/\text{GaAs}/\text{AlP}/\text{GaP}$  QDs batch (Ch. 6). The errors on  $\sigma_\infty$  and  $\tau$  are given in orders of magnitude in parentheses.

## A.2. GaSb/GaP QDs

### A.2.1. Sample 2-Ref

Conventional DLTS was performed on sample 2-Ref using  $V_m = 4.0$  V and  $V_p = -1.0$  V. The results are reported in Tab. A.8 and yield a mean, ensemble activation energy  $E_a = 852(\pm 9)$  meV, an apparent capture cross-section  $\sigma_\infty = 9 \times 10^{-15}$  cm<sup>2</sup> (with an uncertainty of 0.1 orders of magnitude), and a storage time  $\tau = 200$  s (with an uncertainty of 0.03 orders of magnitude).

Charge-selective DLTS was performed on sample 2-Ref with measurement biases ranging from  $V_m = -0.5$  V to  $V_m = 4.0$  V ( $V_p = V_m - 0.5$  V), but presented no peaks.

Sample 2-Ref — Conventional DLTS				
Parameter	Mean value $\mu$	St. dev. $\sigma$	Min. value	Max. value
$E_a$	852.3 meV	9.3 meV	838.6 meV	864.0 meV
$\log_{10} \sigma_\infty$	-14.042	0.129	-14.223	-13.879
$\log_{10} \tau$	2.297	0.031	2.242	2.338

**Table A.8.:** Mean value  $\mu$ , standard deviation  $\sigma$ , minimum value, and maximum value of:  $E_a$ ,  $\log_{10} \sigma_\infty$ , and  $\log_{10} \tau$ ; from  $N = 10$  evaluations of the conventional DLTS measurement performed on sample 2-Ref.

### A.2.2. Sample 2-QD-A

Conventional DLTS was performed on sample 2-QD-A with  $V_m = 10.0$  V and  $V_p = -1.0$  V, whereas charge-selective DLTS was performed with measurement voltages ranging from  $V_m = 0.0$  V to  $V_m = 10.0$  V ( $V_p = V_m - 1.0$  V). Tab. A.9 summarises the results of the analysis performed on conventional DLTS and on the two most relevant steps of charge-selective DLTS: the ground state and the shallowest state of the QDs.

The mean, ensemble activation energy of the QDs is  $E_a = 790(\pm 10)$  meV, the apparent capture cross-section is  $\sigma_\infty = 6 \times 10^{-15}$  cm<sup>2</sup> (with an uncertainty of 0.2 orders of magnitude), and the storage time at room temperature  $\tau = 30$  s (with an uncertainty of 0.07 orders of magnitude).

The shallowest state has an activation energy  $E_a = 578(\pm 6)$  meV, an apparent capture cross-section  $\sigma_\infty = 9 \times 10^{-14}$  cm<sup>2</sup> (with an uncertainty of 0.1 orders of magnitude), and a storage time at room temperature  $\tau = 500$   $\mu$ s (with an uncertainty of 0.04 orders of magnitude).

The activation energy of the ground state represents the localisation energy of the

Appendix A. Error analysis of DLTS measurements

QDs. It amounts to  $E_{\text{loc}} = 900(\pm 20)$  meV, with an associated capture cross-section  $\sigma_{\infty} = 4 \times 10^{-13}$  cm<sup>2</sup> (with an uncertainty of 0.3 orders of magnitude) and a storage time at room temperature  $\tau = 30$  s (with an uncertainty of 0.1 orders of magnitude).

Sample 2-QD-A				
Conventional DLTS				
Parameter	Mean value $\mu$	St. dev. $\sigma$	Min. value	Max. value
$E_a$	790.7 meV	13.6 meV	774.4 meV	820.7 meV
$\log_{10} \sigma_{\infty}$	-14.208	0.218	-14.524	-13.764
$\log_{10} \tau$	1.429	0.072	1.259	1.497
Charge-selective DLTS — Shallowest state				
Parameter	Mean value $\mu$	St. dev. $\sigma$	Min. value	Max. value
$E_a$	578.2 meV	6.4 meV	568.6 meV	588.2 meV
$\log_{10} \sigma_{\infty}$	-13.027	0.135	-13.236	-12.839
$\log_{10} \tau$	-3.321	0.043	-3.406	-3.263
Charge-selective DLTS — Ground state				
Parameter	Mean value $\mu$	St. dev. $\sigma$	Min. value	Max. value
$E_a$	896.6 meV	17.2 meV	878.5 meV	922.8 meV
$\log_{10} \sigma_{\infty}$	-12.405	0.317	-12.804	-11.772
$\log_{10} \tau$	1.404	0.120	1.213	1.509

**Table A.9.:** Mean value  $\mu$ , standard deviation  $\sigma$ , minimum value, and maximum value of:  $E_a$ ,  $\log_{10} \sigma_{\infty}$ , and  $\log_{10} \tau$ ; from  $N = 10$  evaluations of the conventional DLTS measurement performed on sample 2-QD-A, alongside the results from the charge-selective DLTS measurements performed on the ground state and shallowest level of the QDs of the same sample.

### A.2.3. Sample 2-QD-B

Conventional DLTS was performed on sample 2-QD-B with  $V_m = 10.0$  V and  $V_p = -1.0$  V, whereas charge-selective DLTS was performed with measurement voltages ranging from  $V_m = 1.0$  V to  $V_m = 10.0$  V ( $V_p = V_m - 1.0$  V). Tab. A.10 summarises the results of the analysis performed on conventional DLTS and on the two most relevant steps of charge-selective DLTS: the ground state and the shallowest state of the QDs.

The mean, ensemble activation energy of the QDs is  $E_a = 850(\pm 10)$  meV, the apparent capture cross-section is  $\sigma_{\infty} = 6 \times 10^{-14}$  cm<sup>2</sup> (with an uncertainty of 0.2 orders of magnitude), and the storage time at room temperature  $\tau = 30$  s (with an uncertainty of 0.06 orders of magnitude).

The shallowest state has an activation energy  $E_a = 687(\pm 7)$  meV, an apparent capture cross-section  $\sigma_{\infty} = 5 \times 10^{-14}$  cm<sup>2</sup> (with an uncertainty of 0.2 orders of magnitude), and

a storage time at room temperature  $\tau = 0.06 \mu\text{s}$  (with an uncertainty of 0.1 orders of magnitude).

The activation energy of the ground state represents the localisation energy of the QDs. It amounts to  $E_{\text{loc}} = 1.11(\pm 0.03) \text{ eV}$ , with an associated capture cross-section  $\sigma_{\infty} = 4 \times 10^{-11} \text{ cm}^2$  (with an uncertainty of 0.5 orders of magnitude) and a storage time at room temperature  $\tau = 850 \text{ s}$  (with an uncertainty of 0.07 orders of magnitude).

Sample 2-QD-B				
Conventional DLTS				
Parameter	Mean value $\mu$	St. dev. $\sigma$	Min. value	Max. value
$E_a$	853.5 meV	11.0 meV	833.7 meV	869.0 meV
$\log_{10} \sigma_{\infty}$	-13.250	0.190	-13.577	-12.921
$\log_{10} \tau$	1.527	0.064	1.431	1.592
Charge-selective DLTS — Shallowest state				
Parameter	Mean value $\mu$	St. dev. $\sigma$	Min. value	Max. value
$E_a$	687.2 meV	7.3 meV	670.4 meV	695.3 meV
$\log_{10} \sigma_{\infty}$	-13.263	0.213	-13.607	-12.979
$\log_{10} \tau$	-1.256	0.144	-1.476	-1.146
Charge-selective DLTS — Ground state				
Parameter	Mean value $\mu$	St. dev. $\sigma$	Min. value	Max. value
$E_a$	1107.0 meV	34.7 meV	1025.8 meV	1152.8 meV
$\log_{10} \sigma_{\infty}$	-10.395	0.518	-11.623	-9.721
$\log_{10} \tau$	2.930	0.066	2.793	3.025

**Table A.10.:** Mean value  $\mu$ , standard deviation  $\sigma$ , minimum value, and maximum value of:  $E_a$ ,  $\log_{10} \sigma_{\infty}$ , and  $\log_{10} \tau$ ; from  $N = 10$  evaluations of the conventional DLTS measurement performed on sample 2-QD-B, alongside the results from the charge-selective DLTS measurements performed on the ground state and shallowest level of the QDs of the same sample.

#### A.2.4. Sample 2-QD-C

Conventional DLTS was performed on sample 2-QD-C with  $V_m = 6.0 \text{ V}$  and  $V_p = -1.0 \text{ V}$ , whereas charge-selective DLTS was performed with measurement voltages ranging from  $V_m = 2.0 \text{ V}$  to  $V_m = 5.0 \text{ V}$  ( $V_p = V_m - 1.0 \text{ V}$ ). Tab. A.11 summarises the results of the analysis performed on conventional DLTS and on the two most relevant steps of charge-selective DLTS: the ground state and the shallowest state of the QDs.

The mean, ensemble activation energy of the QDs is  $E_a = 860(\pm 20) \text{ meV}$ , the apparent capture cross-section is  $\sigma_{\infty} = 2 \times 10^{-14} \text{ cm}^2$  (with an uncertainty of 0.4 orders of magnitude), and the storage time at room temperature  $\tau = 150 \text{ s}$  (with an uncertainty of 0.03

orders of magnitude).

The shallowest state has an activation energy  $E_a = 959(\pm 6)$  meV, an apparent capture cross-section  $\sigma_\infty = 8 \times 10^{-13}$  cm<sup>2</sup> (with an uncertainty of 0.1 orders of magnitude), and a storage time at room temperature  $\tau = 140$   $\mu$ s (with an uncertainty of 0.03 orders of magnitude).

The activation energy of the ground state represents the localisation energy of the QDs. It amounts to  $E_{\text{loc}} = 1.07(\pm 0.01)$  eV, with an associated capture cross-section  $\sigma_\infty = 7 \times 10^{-12}$  cm<sup>2</sup> (with an uncertainty of 0.2 orders of magnitude) and a storage time at room temperature  $\tau = 1100$  s (with an uncertainty of 0.04 orders of magnitude).

Sample 2-QD-C				
Conventional DLTS				
Parameter	Mean value $\mu$	St. dev. $\sigma$	Min. value	Max. value
$E_a$	863.9 meV	22.9 meV	829.4 meV	910.5 meV
$\log_{10} \sigma_\infty$	-13.717	0.362	-14.281	-12.959
$\log_{10} \tau$	2.168	0.033	2.121	2.228
Charge-selective DLTS — Shallowest state				
Parameter	Mean value $\mu$	St. dev. $\sigma$	Min. value	Max. value
$E_a$	958.6 meV	6.3 meV	949.7 meV	970.4 meV
$\log_{10} \sigma_\infty$	-12.110	0.122	-12.267	-11.873
$\log_{10} \tau$	2.152	0.027	2.093	2.173
Charge-selective DLTS — Ground state				
Parameter	Mean value $\mu$	St. dev. $\sigma$	Min. value	Max. value
$E_a$	1070.2 meV	14.3 meV	1037.1 meV	1085.1 meV
$\log_{10} \sigma_\infty$	-11.142	0.202	-11.599	-10.928
$\log_{10} \tau$	3.058	0.039	2.959	3.095

**Table A.11.:** Mean value  $\mu$ , standard deviation  $\sigma$ , minimum value, and maximum value of:  $E_a$ ,  $\log_{10} \sigma_\infty$ , and  $\log_{10} \tau$ ; from  $N = 10$  evaluations of the conventional DLTS measurement performed on sample 2-QD-C, alongside the results from the charge-selective DLTS measurements performed on the ground state and shallowest level of the QDs of the same sample.

### A.2.5. Sample 2-QD-D

Conventional DLTS was performed on sample 2-QD-D with  $V_m = 4.0$  V and  $V_p = -2.0$  V, whereas charge-selective DLTS was performed with measurement voltages ranging from  $V_m = -1.5$  V to  $V_m = 4.0$  V ( $V_p = V_m - 0.5$  V). Tab. A.12 summarises the results of the analysis performed on conventional DTLS and on the two most relevant steps of charge-selective DLTS: the ground state and the shallowest state of the QDs.

The mean, ensemble activation energy of the QDs is  $E_a = 1.03(\pm 0.01)$  eV, the apparent capture cross-section is  $\sigma_\infty = 5 \times 10^{-14}$  cm<sup>2</sup> (with an uncertainty of 0.2 orders of magnitude), and the storage time at room temperature  $\tau = 36000$  s (0.4 days, with an uncertainty of 0.04 orders of magnitude).

The shallowest state has an activation energy  $E_a = 735(\pm 6)$  meV, an apparent capture cross-section  $\sigma_\infty = 2 \times 10^{-15}$  cm<sup>2</sup> (with an uncertainty of 0.1 orders of magnitude), and a storage time at room temperature  $\tau = 12$   $\mu$ s (with an uncertainty of 0.04 orders of magnitude).

The activation energy of the ground state represents the localisation energy of the QDs. It amounts to  $E_{\text{loc}} = 1.18(\pm 0.09)$  eV, with an associated capture cross-section  $\sigma_\infty = 1 \times 10^{-12}$  cm<sup>2</sup> (with an uncertainty of 0.1 orders of magnitude) and a storage time at room temperature  $\tau = 337000$  s (3.9 days, with an uncertainty of 0.04 orders of magnitude).

Sample 2-QD-D				
Conventional DLTS				
Parameter	Mean value $\mu$	St. dev. $\sigma$	Min. value	Max. value
$E_a$	1032.9 meV	12.7 meV	1019.0 meV	1054.5 meV
$\log_{10} \sigma_\infty$	-13.271	0.171	-13.460	-12.983
$\log_{10} \tau$	4.561	0.043	4.515	4.635
Charge-selective DLTS — Shallowest state				
Parameter	Mean value $\mu$	St. dev. $\sigma$	Min. value	Max. value
$E_a$	735.0 meV	6.2 meV	728.8 meV	746.9 meV
$\log_{10} \sigma_\infty$	-14.795	0.097	-14.903	-14.629
$\log_{10} \tau$	1.080	0.016	1.048	1.113
Charge-selective DLTS — Ground state				
Parameter	Mean value $\mu$	St. dev. $\sigma$	Min. value	Max. value
$E_a$	1175.1 meV	9.4 meV	1166.9 meV	1193.9 meV
$\log_{10} \sigma_\infty$	-11.849	0.122	-11.959	-11.604
$\log_{10} \tau$	5.528	0.036	5.497	5.598

**Table A.12.:** Mean value  $\mu$ , standard deviation  $\sigma$ , minimum value, and maximum value of:  $E_a$ ,  $\log_{10} \sigma_\infty$ , and  $\log_{10} \tau$ ; from  $N = 10$  evaluations of the conventional DLTS measurement performed on sample 2-QD-D, alongside the results from the charge-selective DLTS measurements performed on the ground state and shallowest level of the QDs of the same sample.

### **A.2.6. Sample 2-QD-AIP**

Conventional DLTS was performed on sample 2-QD-AIP with  $V_m = 15.0$  V and  $V_p = -1.0$  V, whereas charge-selective DLTS was performed with measurement voltages ranging from  $V_m = 0.0$  V to  $V_m = 15.0$  V ( $V_p = V_m - 1.0$  V). Tab. A.13 summarises the results of the analysis performed on conventional DLTS and on the two most relevant steps of charge-selective DLTS: the ground state and the shallowest state of the QDs.

The mean, ensemble activation energy of the QDs is  $E_a = 890(\pm 20)$  meV, the apparent capture cross-section is  $\sigma_\infty = 2 \times 10^{-14}$  cm<sup>2</sup> (with an uncertainty of 0.3 orders of magnitude), and the storage time at room temperature  $\tau = 500$  s (with an uncertainty of 0.09 orders of magnitude).

The shallowest state has an activation energy  $E_a = 541(\pm 7)$  meV, an apparent capture cross-section  $\sigma_\infty = 8 \times 10^{-16}$  cm<sup>2</sup> (with an uncertainty of 0.1 orders of magnitude), and a storage time at room temperature  $\tau = 14$  ms (with an uncertainty of 0.04 orders of magnitude).

The activation energy of the ground state represents the localisation energy of the QDs. It amounts to  $E_{\text{loc}} = 1.17(\pm 0.04)$  eV, with an associated capture cross-section  $\sigma_\infty = 2 \times 10^{-9}$  cm<sup>2</sup> (with an uncertainty of 0.6 orders of magnitude) and a storage time at room temperature  $\tau = 270$  s (with an uncertainty of 0.08 orders of magnitude).

Sample 2-QD-AIP				
Conventional DLTS				
Parameter	Mean value $\mu$	St. dev. $\sigma$	Min. value	Max. value
$E_a$	891.8 meV	18.9 meV	860.9 meV	927.9 meV
$\log_{10} \sigma_\infty$	-13.783	0.282	-14.292	-13.213
$\log_{10} \tau$	2.702	0.086	2.462	2.750
Charge-selective DLTS — Shallowest state				
Parameter	Mean value $\mu$	St. dev. $\sigma$	Min. value	Max. value
$E_a$	541.0 meV	7.0 meV	530.7 meV	551.6 meV
$\log_{10} \sigma_\infty$	-15.111	0.149	-15.360	-14.893
$\log_{10} \tau$	-1.863	0.036	-1.906	-1.788
Charge-selective DLTS — Ground state				
Parameter	Mean value $\mu$	St. dev. $\sigma$	Min. value	Max. value
$E_a$	1173.4 meV	37.9 meV	1076.4 meV	1223.7 meV
$\log_{10} \sigma_\infty$	-8.781	0.566	-10.231	-8.025
$\log_{10} \tau$	2.431	0.075	2.251	2.519

**Table A.13.:** Mean value  $\mu$ , standard deviation  $\sigma$ , minimum value, and maximum value of:  $E_a$ ,  $\log_{10} \sigma_\infty$ , and  $\log_{10} \tau$ ; from  $N = 10$  evaluations of the conventional DLTS measurement performed on sample 2-QD-AIP, alongside the results from the charge-selective DLTS measurements performed on the ground state and shallowest level of the QDs of the same sample.

Sample	$E_{\text{loc}}$	$\sigma_\infty$	$\tau$ (at 300 K)
2-QD-A	0.90( $\pm 0.02$ ) eV	$4 \times 10^{-13}$ (0.3) $\text{cm}^2$	30(0.1) s
2-QD-B	1.11( $\pm 0.03$ ) eV	$4 \times 10^{-11}$ (0.5) $\text{cm}^2$	850(0.07) s
2-QD-C	1.07( $\pm 0.01$ ) eV	$7 \times 10^{-12}$ (0.2) $\text{cm}^2$	1100(0.04) s
2-QD-D	1.18( $\pm 0.09$ ) eV	$1 \times 10^{-12}$ (0.1) $\text{cm}^2$	3.9(0.04) days
2-QD-AIP	1.17( $\pm 0.04$ ) eV	$2 \times 10^{-9}$ (0.6) $\text{cm}^2$	270(0.08) s

**Table A.14.:** Summary of the localisation energies, apparent capture cross-sections, and storage times at room temperature of the samples of the GaSb/GaP QDs batch (Ch. 7). Errors on  $\sigma_\infty$  and  $\tau$  are given in orders of magnitude in parentheses.



## Appendix B.

### Samples

This appendix reports the real names of the samples characterised, alongside some details on their growth and structural characterization.

#### B.1. $\text{In}_{0.5}\text{Ga}_{0.5}\text{As}/\text{GaAs}/\text{AlP}/\text{GaP}$ QDs

1-QD	1-TU10880-A
1-Barr	1-TU10881-B
1-Ref	1-TU10860-A

**Growth:** G. Stracke and E. Sala; D. Bimberg's group; Institute for Solid State Physics, Technical University of Berlin.

**AFM characterisation:** G. Stracke and E. Sala; *ibidem*.

#### B.2. $\text{GaSb}/\text{GaP}$ QDs

2-Ref	1-G150606-A
2-QD-A	1-G150607-A
2-QD-B	1-G150608-A
2-QD-C	1-G150612-A
2-QD-D	1-G150613-A
2-QD-E	1-G150615-A
2-QD-AIP	1-G150614-A

**Growth:** L. Desplanque, C. Coinon, X. Wallart; Intitute for Electronics, Microelectronics and Nanotechnology, Lille, France.

**AFM characterisation:** L. Desplanque, C. Coinon, X. Wallart; IEMN, CNRS Lille, France.

*Appendix B. Samples*

**HAADF-STEM and strain maps:** Y. Wang and P. Ruterana; Centre of Research on Ions, Materials and Photonics (CIMAP), CNRS-ENSICAEN-CEA-UCBN Caen, France.

**EDX maps:** G. Patriarche; Centre for Nanosciences and Nanotechnology (C2N), Marcoussis, France.

## Appendix C.

### Experimental details

This appendix provides details on the experimental setup used for C–V profiling and for DLTS. Moreover, it contains the recipes used for the clean-room processing of the samples.

#### C.1. C–V profiling setup

The schematic layout of the setup for C–V profiling is shown in Fig. C.1. The sample (purple) is cooled inside a cryostat. Two configurations are available: A helium flow cryostat (CryoVac) controlled by an Oxford Instruments ITC503S temperature controller, or a closed-cycle cryostat (Brooks) controlled by a Lakeshore LS325 temperature controller. Both configurations allow for temperatures from  $\sim 20$  K to  $\sim 425$  K. The sample contacts are connected to an HP4284A LCR meter. The LCR meter has an internal voltage source, providing measurement frequencies from 22 Hz to 1 MHz and AC amplitudes from 5 mV to 1 V. The temperature controller and the LCR meter are controlled by a computer via custom LabView software.

#### C.2. DLTS setup

The schematic layout of the setup for DLTS measurements is shown in Fig. C.2. As for the C–V measurement, both the helium flow cryostat and the closed-cycle cryostat can be used for temperature regulation. In this case the sample is connected to a Boonton 7200 capacitance meter. The meter operates at a frequency of 1 MHz and an AC amplitude of 100 mV. A (static) capacitance correction is implemented in order to operate the meter in its range of highest sensitivity. The correction is controlled by a variable capacitor (range: 3–240 pF) connected to a stepper motor, which is in turn controlled by the computer. The voltage is regulated by a pulse generator (either HP-8115A or HP-8116A). The

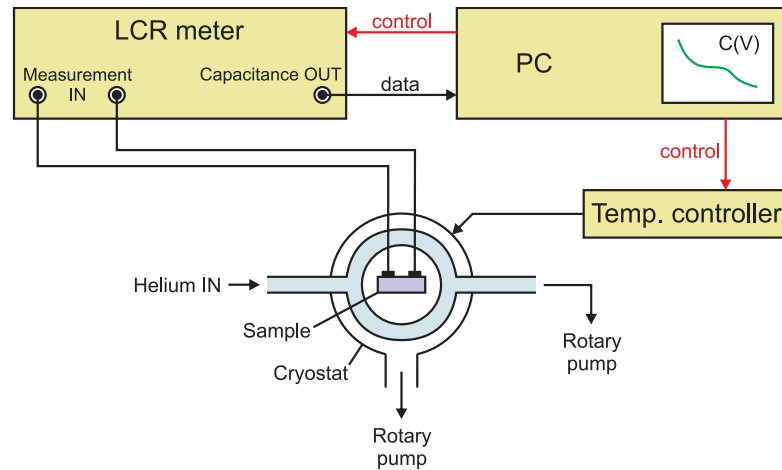


Figure C.1.: CV setup

measurement is controlled by the computer via LabView software. For each temperature step, the measurement cycle starts with the pulse generator applying the measurement voltage to the sample. The capacitance is then offset using the variable capacitor. The digital-to-analog converter (NI-DAQ) sends a trigger signal to the pulse generator and starts sampling, acquiring the capacitance transient and transferring it to the computer. After the computer has collected all transients, it generates the DLTS spectra.

### C.3. Processing

As mentioned in Sc. 5.3.1, two processing methods have been used in this work: “standard” processing and “simplified” processing.

Standard processing is a three-step procedure. Every step begins with the definition of the relevant structures via ultraviolet (UV) optical lithography. After lithography, in the first step the top contacts (n-type contacts: Ni/AuGe/Au) are thermally evaporated and deposited on the sample; in the second step mesas are etched (diameter: 400  $\mu\text{m}$  and 800  $\mu\text{m}$ ) via inductively coupled plasma reactive-ion etching (ICP-RIE); and in the third step the back contacts (p-type contacts: Ni/Zn/Au) are thermally evaporated and deposited from the top of the sample on the highly p-doped contact layer (exposed through the previous etching). The contacts are then thermally annealed at 400  $^{\circ}\text{C}$  for 3 minutes in nitrogen atmosphere, after which the samples are fixed to a ceramic chip carrier using conductive epoxy glue (Epo-Tek H20E). Finally, the devices are contacted using gold wire and a manual ball-wedge bonder (FEK Delvotec 5410).

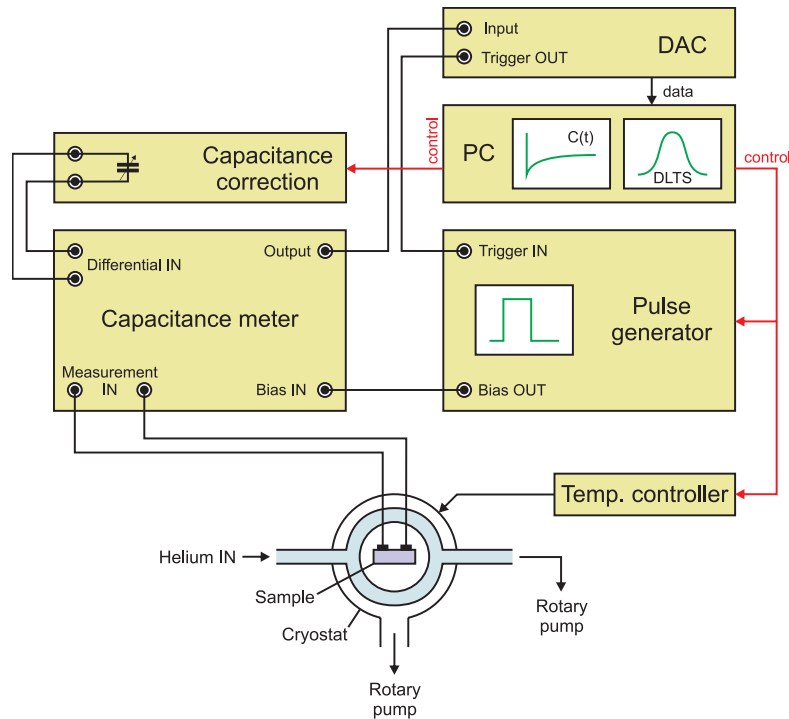


Figure C.2.: DLTS setup

Simplified processing dispenses of step 2 and of optical lithography in step 3 by placing the back contact directly on the bottom side of the sample. Etching becomes unnecessary because the size of the devices is defined by the size of the top contacts, which have in this case the same size as the mesas obtained with the standard processing method (diameter: 400  $\mu\text{m}$  and 800  $\mu\text{m}$ ). The annealing and bonding steps remain unchanged. Simplified processing can only be performed on samples grown on a  $p^+$ -doped substrate because lower doping densities would hinder the formation of an Ohmic contact, whereas an  $n^+$ -doped substrate would not match the polarity of the device.

All samples were processed at the Center of Nanophotonics (Nanophotonik-Zentrum, NPZ) of the Technische Universität Berlin.

### C.3.1. Lithography and metallisation of the Ohmic top contact

#### 1. Sample cleaning:

- 2x rinse in acetone (2 min per rinse).
- 2x rinse in isopropanol (2 min per rinse).

### *Appendix C. Experimental details*

- Dry with N<sub>2</sub>.
2. Lithography of top contact:
    - Heat on hotplate at 120 °C for 5 min.
    - Spin coat with photoresist MaN-440 (at 2500 rpm for 35 s).
    - Pre-bake on hotplate at 90 °C for 5 min.
    - Exposure with mask at 6 mW/cm<sup>2</sup> for 10 s.
    - Develop with MaD-532-S for ca. 90 s.
    - Stop development with 2x H<sub>2</sub>O dip and DI water cascade.
    - Remove excess photoresist with plasma oxidation (150 W, 50 Pa, 76 ml/min O<sub>2</sub>, 3 min).
  3. Metallisation of top contact:
    - Dip in 20:80 HCl/H<sub>2</sub>O solution.
    - Clean in DI water cascade.
    - Dry with N<sub>2</sub>.
    - Evaporate 8 nm Ni, 100 nm Au-Ge (88:12 mixture), 300 nm Au.
  4. Lift-off:
    - Lift off photoresist with N-Methyl-2-pyrrolidone (NMP) at 76 °C.
    - 2x rinse in acetone (2 min per rinse at 76 °C).
    - 2x rinse in isopropanol (2 min per rinse at 76 °C).
    - Dry with N<sub>2</sub>.

#### **C.3.2. Lithography and dry-etching of mesas**

(not used in simplified processing)

1. Sample cleaning:
  - 2x rinse in acetone (2 min per rinse).
  - 2x rinse in isopropanol (2 min per rinse).
  - Dry with N<sub>2</sub>.
2. Lithography of mesa structure:

- Heat on hotplate at 120 °C for 5 min.
- Spin coat with photoresist AZ-MIR701 (at 3000 rpm for 35 s).
- Pre-bake on hotplate at 100 °C for 2 min.
- Exposure with mask at 6 mW/cm<sup>2</sup> for 35 s.
- Develop with AZ351B for ca. 25 s.
- Stop development with 2x H<sub>2</sub>O dip and DI water cascade.
- Remove excess photoresist with plasma oxidation (150 W, 50 Pa, 76 ml/min O<sub>2</sub>, 3 min).

### 3. Dry-etching of mesas:

- Etch using the following recipe (written by M. Stubenrauch at TU Berlin for the Sentech Instruments GmbH ICP-RIE SI 500 reactor).

```
1 [Info]
2 Filetype=SENTECH Instruments SI Systems recipe file
3 Anlage=SI 500/D-2M TUB
4 Reaktor=2
5 [Lines]
6 0=DIM ZEIT AS INTEGER = 300
7 1=Druck Wafer R\"{u}cks.k\"{u}hlung 1000,0 Pa
8 2=Wartezeit 10
9 3=Temperatur Elektrode 20,0 \gradC
10 4=Wartezeit 10
11 5=Gas ein MFC 3 5,0 sccm ' Ar
12 6=Gas ein MFC 1 20,0 sccm ' BC13
13 7=Reaktordruck 1,000 Pa
14 8=Quellen-Matching manuell 55,9
15 9=HF-Matching manuell 74,0
16 10=Wartezeit 10
17 11=Quelle ein 300,0 W
18 12=Wartezeit 10
19 13=HF-Generator ein Bias -200,0 V
20 14=Quellen-Matching automatisch
21 15=HF-Matching automatisch
22 16=Wartezeit ZEIT
23 17=HF-Generator aus
24 18=Quelle aus
25 19=Gas aus MFC 3 ' Ar
```

### Appendix C. Experimental details

```
26 20=Gas aus MFC 1 ' BC13
27 21=Reaktordruck 0,000 Pa
28 22=Wartezeit 20
29 23=Wafer ausschl. ohne Bel\ "{u}ftung
30 [Internal Lines]
31 0=Dim ZEIT As Integer = 300
32 1=OutAA AA_HED 1000.0 Pa
33 2=WZeit 10
34 3=OutAA AA_TEL 20.0 \gradC
35 4=WZeit 10
36 5=GasEin MFC 3 5.0 sccm ' Ar
37 6=GasEin MFC 1 20.0 sccm ' BC13
38 7=RxDruck 1.000 Pa
39 8=QMBMan 55.9
40 9=HFMBMan 74.0
41 10=WZeit 10
42 11=Qein 300.0 W
43 12=WZeit 10
44 13=HFein Bia -200.0 V
45 14=QMBAuto
46 15=HFMAuto
47 16=WZeit ZEIT
48 17=HFaus
49 18=Qaus
50 19=GasAus MFC 3 ' Ar
51 20=GasAus MFC 1 ' BC13
52 21=RxDruck 0.000 Pa
53 22=WZeit 20
54 23=WafAusOB}
```

- Determine etch rate using a dummy sample and adjust etch time accordingly.

#### 4. Lift-off:

- Lift off photoresist with N-Methyl-2-pyrrolidone (NMP) at 76 °C.
- 2x rinse in acetone (2 min per rinse at 76 °C).
- 2x rinse in isopropanol (2 min per rinse at 76 °C).
- Dry with N<sub>2</sub>.

### C.3.3. Lithography and metallisation of the Ohmic back contact

(no lithography necessary for simplified processing)

1. Sample cleaning:

- 2x rinse in acetone (2 min per rinse).
- 2x rinse in isopropanol (2 min per rinse).
- Dry with N<sub>2</sub>.

2. Lithography of back contact:

- Heat on hotplate at 120 °C for 5 min.
- Spin coat with photoresist MaN-440 (at 2500 rpm for 35 s).
- Pre-bake on hotplate at 90 °C for 5 min.
- Exposure with mask at 6 mW/cm<sup>2</sup> for 10 s.
- Develop with MaD-532-S for ca. 90 s.
- Stop development with 2x H<sub>2</sub>O dip and DI water cascade.
- Remove excess photoresist with plasma oxidation (150 W, 50 Pa, 76 ml/min O<sub>2</sub>, 3 min).

3. Metallisation of back contact:

- Dip in 20:80 HCl/H<sub>2</sub>O solution.
- Clean in DI water cascade.
- Dry with N<sub>2</sub>.
- Evaporate 8 nm Ni, 100 nm Zn, 300 nm Au.

4. Lift-off:

- Lift off photoresist with N-Methyl-2-pyrrolidone (NMP) at 76 °C.
- 2x rinse in acetone (2 min per rinse at 76 °C).
- 2x rinse in isopropanol (2 min per rinse at 76 °C).
- Dry with N<sub>2</sub>.



## Bibliography

- [1] J. Gantz and D. Reinsel. "Extracting Value from Chaos". In: *IDC iView* (2011).
- [2] J. Gantz and D. Reinsel. "The Digital Universe Decade — Are You Ready?" In: *IDC iView* (2010).
- [3] G. Moore. "Cramming more components onto integrated circuits". In: *Electronics* 8 (1965), p. 114.
- [4] *International Technology Roadmap for Semiconductors 2.0*. Tech. rep. 2015.
- [5] *International Technology Roadmap for Semiconductors*. Tech. rep. 2013.
- [6] S. Sze and K. K. Ng. *Physics of Semiconductor Devices*. Wiley-Blackwell, Apr. 2006. DOI: 10.1002/0470068329.
- [7] D. Bimberg, M. Grundmann, and N. N. Ledentsov. *Quantum Dot Heterostructures*. John Wiley and Sons, Inc., 1998.
- [8] T. Müller, F. F. Schrey, G. Strasser, and K. Unterrainer. "Ultrafast intraband spectroscopy of electron capture and relaxation in InAs/GaAs quantum dots". In: *Appl. Phys. Lett.* 83.17 (2003), p. 3572. DOI: 10.1063/1.1622432.
- [9] M. Geller, A. Marent, E. Stock, D. Bimberg, V. I. Zubkov, I. S. Shulgunova, and A. V. Solomonov. "Hole capture into self-organized InGaAs quantum dots". In: *Appl. Phys. Lett.* 89.23 (2006), p. 232105. DOI: 10.1063/1.2400059.
- [10] A. Marent and D. Bimberg. *Speicherzelle*. German Patent N. 10 2011 006 782.5. Oct. 2012.
- [11] D. Bimberg, M. Geller, A. Marent, and T. Nowozin. *Memory*. U.S. Patent N. 8331142 B2. Dec. 2012.
- [12] A. Marent, T. Nowozin, M. Geller, and D. Bimberg. "The QD-Flash: a quantum-dot based memory device". In: *Semicond. Sci. Technol.* 26 (2011), p. 014026. DOI: 10.1088/0268-1242/26/1/014026.

## Bibliography

- [13] A. Marent, T. Nowozin, J. Gelze, F. Luckert, and D. Bimberg. "Hole-based memory operation in an InAs/GaAs quantum dot heterostructure". In: *Appl. Phys. Lett.* 95 (2009), p. 242114. doi: 10.1063/1.3275758.
- [14] A. Marent, M. Geller, A. Schliwa, D. Feise, K. Pötschke, D. Bimberg, N. Akçay, and N. Öncan. "10<sup>6</sup> years extrapolated hole storage time in GaSb/AlAs quantum dots". In: *Appl. Phys. Lett.* 91 (2007), p. 242109. doi: 10.1063/1.2824884.
- [15] M. Geller, A. Marent, T. Nowozin, D. Bimberg, N. Akçay, and N. Öncan. "A write time of 6 ns for quantum-dot-based memory structures". In: *Appl. Phys. Lett.* 92 (2008), p. 092108. doi: 10.1063/1.2890731.
- [16] T. Nowozin, A. Beckel, D. Bimberg, A. Lorke, and M. Geller. "3 ns single-shot read-out in quantum dot-based memory structure". In: *Appl. Phys. Lett.* 104 (2014), p. 053111. doi: 10.1063/1.4864281.
- [17] R. Waser. *Nanoelectronics and Information Technology*. Wiley-VCH, Berlin, 2003.
- [18] P. Cottrell, R. Troutman, and T. Ning. "Hot-electron emission in n-channel IGFETs". In: *IEEE J. Solid-State Circuits* 14.2 (Apr. 1979), pp. 442–455. doi: 10.1109/jssc.1979.1051196.
- [19] M. Lenzlinger. "Fowler-Nordheim Tunneling into Thermally Grown SiO<sub>2</sub>". In: *J. Appl. Phys.* 40.1 (1969), p. 278. doi: 10.1063/1.1657043.
- [20] S. Yamaguchi, E. Ichinohe, and J. Katsura. "Static random access memory". 4712194. 1987.
- [21] V. A. Pedroni. *Digital Electronics and Design with VHDL*. Morgan Kaufmann, 2008.
- [22] S. Skorobogatov. "Low temperature data remanence in static RAM". In: *University of Cambridge Computer Laboratory Technical Report* 536 (2002), p. 11.
- [23] J. T. Clemens, J. D. Cuthbert, F. J. Procyk, and G. M. Trout. "Dynamic random access memory". 4240195. 1980.
- [24] F. Masuoka, M. Asano, H. Iwahashi, T. Komuro, and S. Tanaka. "A new flash EEPROM cell using triple polysilicon technology". In: *1984 International Electron Devices Meeting*. Institute of Electrical & Electronics Engineers (IEEE), 1984. doi: 10.1109/iedm.1984.190752.
- [25] P. Pavan, R. Bez, P. Olivo, and E. Zanoni. "Flash memory cells-an overview". In: *Proceedings of the IEEE* 85.8 (1997), pp. 1248–1271. doi: 10.1109/5.622505.

- [26] R. Bez, E. Camerlenghi, A. Modelli, and A. Visconti. "Introduction to flash memory". In: *Proceedings of the IEEE* 91.4 (Apr. 2003), pp. 489–502. doi: 10.1109/jproc.2003.811702.
- [27] B. Marquardt, M. Geller, A. Lorke, D. Reuter, and A. D. Wieck. "Using a two-dimensional electron gas to study nonequilibrium tunneling dynamics and charge storage in self-assembled quantum dots". In: *Applied Physics Letters* 95.2 (2009), p. 022113. doi: 10.1063/1.3175724.
- [28] G. W. Burr, B. N. Kurdi, J. C. Scott, C. H. Lam, K. Gopalakrishnan, and R. S. Shenoy. "Overview of candidate device technologies for storage-class memory". In: *IBM J. Res. & Dev.* 52.4.5 (July 2008), pp. 449–464. doi: 10.1147/rd.524.0449.
- [29] A. Sheikholeslami and P. Gulak. "A survey of circuit innovations in ferroelectric random-access memories". In: *Proceedings of the IEEE* 88.5 (May 2000), pp. 667–689. doi: 10.1109/5.849164.
- [30] N. Setter, D. Damjanovic, L. Eng, G. Fox, S. Gevorgian, S. Hong, A. Kingon, H. Kohlstedt, N. Y. Park, G. B. Stephenson, and et al. "Ferroelectric thin films: Review of materials, properties, and applications". In: *Journal of Applied Physics* 100.5 (2006), p. 051606. doi: 10.1063/1.2336999.
- [31] S. Parkin, X. Jiang, C. Kaiser, A. Panchula, K. Roche, and M. Samant. "Magnetically engineered spintronic sensors and memory". In: *Proc. IEEE* 91.5 (May 2003), pp. 661–680. doi: 10.1109/jproc.2003.811807.
- [32] M. Julliere. "Tunneling between ferromagnetic films". In: *Physics Letters A* 54.3 (Sept. 1975), pp. 225–226. doi: 10.1016/0375-9601(75)90174-7.
- [33] S. S. P. Parkin, M. Hayashi, and L. Thomas. "Magnetic Domain-Wall Racetrack Memory". In: *Science* 320.5873 (Apr. 2008), pp. 190–194. doi: 10.1126/science.1145799.
- [34] S. Raoux, G. W. Burr, M. J. Breitwisch, C. T. Rettner, Y.-C. Chen, R. M. Shelby, M. Salinga, D. Krebs, S.-H. Chen, H.-L. Lung, and et al. "Phase-change random access memory: A scalable technology". In: *IBM J. Res. & Dev.* 52.4.5 (July 2008), pp. 465–479. doi: 10.1147/rd.524.0465.
- [35] *International Technology Roadmap for Semiconductors*. Tech. rep. 2005.
- [36] E. Le Sueur and G. Heiser. "Dynamic voltage and frequency scaling: The laws of diminishing returns". In: *Proceedings of the 2010 international conference on Power aware computing and systems*. 2010, pp. 1–8.

## Bibliography

- [37] A. Marent. "Entwicklung einer neuartigen Quantenpunkt-Speicherzelle". PhD thesis. Technische Universität Berlin, 2010.
- [38] G. B. Stringfellow. *Organometallic Vapor-Phase Epitaxy: Theory and Practice*. Academic Press, San Diego, 1998. 572 Seiten.
- [39] G. S. May and S. M. Sze. *Fundamentals of Semiconductor Fabrication*. John Wiley and Sons, Inc., 2007.
- [40] J. R. Arthur. "Molecular beam epitaxy". In: *Surface Science* 500.1-3 (Mar. 2002), pp. 189–217. DOI: 10.1016/s0039-6028(01)01525-4.
- [41] T. Mimura, K. Joshin, S. Hiyamizu, K. Hikosaka, and M. Abe. "High Electron Mobility Transistor Logic". In: *Japanese Journal of Applied Physics* 20.8 (Aug. 1981), pp. L598–L600. DOI: 10.1143/jjap.20.1598.
- [42] D. Delagebeaudeuf, P. Delescluse, P. Etienne, M. Laviron, J. Chapiart, and T. Nuyen. "Two-dimensional electron gas MESFET structure". In: *Electronics Letters* 16.17 (Aug. 1980), pp. 667–668. DOI: 10.1049/e1:19800473.
- [43] I. Hayashi. "Junction lasers which operate continuously at room temperature". In: *Applied Physics Letters* 17.3 (1970), p. 109. DOI: 10.1063/1.1653326.
- [44] F. K. Reinhart. "Mode Reflectivity and Waveguide Properties of Double-Heterostructure Injection Lasers". In: *J. Appl. Phys.* 42.11 (1971), p. 4466. DOI: 10.1063/1.1659796.
- [45] R. A. Milano, T. H. Windhorn, E. R. Anderson, G. E. Stillman, R. D. Dupuis, and P. D. Dapkus. "Al<sub>0.5</sub>Ga<sub>0.5</sub>As-GaAs heterojunction phototransistors grown by metalorganic chemical vapor deposition". In: *Applied Physics Letters* 34.9 (1979), p. 562. DOI: 10.1063/1.90867.
- [46] D. Schicketanz and G. Zeidler. "GaAs-double-heterostructure lasers as optical amplifiers". In: *IEEE Journal of Quantum Electronics* 11.2 (Feb. 1975), pp. 65–69. DOI: 10.1109/jqe.1975.1068560.
- [47] C. Y. Chen. "Ultrahigh speed modulation-doped heterostructure field-effect photodetectors". In: *Appl. Phys. Lett.* 42.12 (1983), p. 1040. DOI: 10.1063/1.93835.
- [48] N. Holonyak and S. F. Bevacqua. "Coherent (visible) light emission from Ga(As<sub>1-x</sub>P<sub>x</sub>) junctions". In: *Applied Physics Letters* 1.4 (1962), p. 82. DOI: 10.1063/1.1753706.
- [49] Z. I. Alferov and R. F. Kazarinov. *Semiconductor laser with electric pumping*. Inventor's Certificate No. 181737 [in Russian], Application No. 950840. 1963.
- [50] H. Kroemer. "Solid state radiation emitters". 3309553. 1963.

- [51] Z. I. Alferov. "The double heterostructure: concept and its applications in physics, electronics and technology". In: *Nobel Lecture* (2000).
- [52] H. Kroemer. "Quasi-electric fields and band offsets: teaching electrons new tricks". In: *Nobel lecture* (2000). DOI: 10.1142/s0217979202010245.
- [53] H. Soda, K.-I. Iga, C. Kitahara, and Y. Suematsu. "GaInAsP/InP Surface Emitting Injection Lasers". In: *Jpn. J. Appl. Phys.* 18.12 (Dec. 1979), pp. 2329–2330. DOI: 10.1143/jjap.18.2329.
- [54] M. Grabherr, H. Moench, and A. Pruijboom. "VCSELs for Optical Mice and Sensing". In: *Springer Series in Optical Sciences*. Springer Science + Business Media, Oct. 2012, pp. 521–538. DOI: 10.1007/978-3-642-24986-0\_17.
- [55] A. Alduino and M. Paniccia. "Interconnects: Wiring electronics with light". In: *Nature Photonics* 1.3 (Mar. 2007), pp. 153–155. DOI: 10.1038/nphoton.2007.17.
- [56] I. Vurgaftman and J. R. Meyer. "Band parameters for III-V compound semiconductors and their alloys". In: *J. Appl. Phys.* 89 (2001), pp. 5815–5863. DOI: 10.1063/1.1368156.
- [57] H. Kroemer. "Barrier control and measurements: Abrupt semiconductor heterojunctions". In: *Journal of Vacuum Science & Technology B: Microelectronics and Nanometer Structures* 2.3 (1984), p. 433. DOI: 10.1116/1.582890.
- [58] E. T. Yu, J. O. McCaldin, and T. C. McGill. "Band Offsets in Semiconductor Heterojunctions". In: *Solid State Physics* 46 (1992), pp. 1–146. DOI: 10.1016/s0081-1947(08)60397-5.
- [59] S. Campbell, F. Johnson, S. Karthikeyan, S.-H. Song, R. Liptak, and B. Benton. "Sputtered metal oxide broken gap junctions". In: *ECS Meeting Abstracts*. Vol. 1. 2014, p. 1385.
- [60] F. Johnson, S. H. Song, J. Abrahamson, R. Liptak, E. Aydil, and S. A. Campbell. "Sputtered metal oxide broken gap junctions for tandem solar cells". In: *Solar Energy Materials and Solar Cells* 132 (Jan. 2015), pp. 515–522. DOI: 10.1016/j.solmat.2014.09.042.
- [61] J. H. Davies. *The physics of low-dimensional semiconductors*. Cambridge University Press, 1998.
- [62] M. A. Kastner. "Artificial Atoms". In: *Physics Today* 46.1 (1993), p. 24. DOI: 10.1063/1.881393.

## Bibliography

- [63] E. Conwell and V. F. Weisskopf. "Theory of Impurity Scattering in Semiconductors". In: *Physical Review* 77.3 (Feb. 1950), pp. 388–390. doi: 10.1103/physrev.77.388.
- [64] R. Dingle, H. L. Störmer, A. C. Gossard, and W. Wiegmann. "Electron mobilities in modulation-doped semiconductor heterojunction superlattices". In: *Applied Physics Letters* 33.7 (1978), p. 665. doi: 10.1063/1.90457.
- [65] C. Foxon. "Three decades of molecular beam epitaxy". In: *Journal of Crystal Growth* 251.1-4 (Apr. 2003), pp. 1–8. doi: 10.1016/s0022-0248(02)02396-5.
- [66] K. v. Klitzing, G. Dorda, and M. Pepper. "New Method for High-Accuracy Determination of the Fine-Structure Constant Based on Quantized Hall Resistance". In: *Physical Review Letters* 45.6 (Aug. 1980), pp. 494–497. doi: 10.1103/physrevlett.45.494.
- [67] K. v. Klitzing. "The quantized Hall effect". In: *Nobel Lecture* (1985).
- [68] M. J. Manfra, L. N. Pfeiffer, K. W. West, R. de Picciotto, and K. W. Baldwin. "High mobility two-dimensional hole system in GaAs/AlGaAs quantum wells grown on (100) GaAs substrates". In: *Applied Physics Letters* 86.16 (2005), p. 162106. doi: 10.1063/1.1900949.
- [69] D. Bimberg, ed. *Semiconductor Nanostructures*. Springer Science + Business Media, 2008.
- [70] Y. Arakawa. "Multidimensional quantum well laser and temperature dependence of its threshold current". In: *Applied Physics Letters* 40.11 (1982), p. 939. doi: 10.1063/1.92959.
- [71] M. Grundmann. "The present status of quantum dot lasers". In: *Physica E: Low-dimensional Systems and Nanostructures* 5.3 (Dec. 1999), pp. 167–184. doi: 10.1016/s1386-9477(99)00041-7.
- [72] F. Heinrichsdorff, C. Ribbat, M. Grundmann, and D. Bimberg. "High-power quantum-dot lasers at 1100 nm". In: *Applied Physics Letters* 76.5 (2000), p. 556. doi: 10.1063/1.125816.
- [73] N. Kirstaedter, M. Grundmann, U. Richter, V. Ustinov, P. Kop'ev, D. Bimberg, P. Werner, S. Ruvimov, N. Ledentsov, U. Gösele, and et al. "Low threshold, large To injection laser emission from (InGa)As quantum dots". In: *Electronics Letters* 30.17 (Aug. 1994), pp. 1416–1417. doi: 10.1049/el:19940939.

- [74] M. Kuntz, G. Fiol, M. Lämmlin, D. Bimberg, M. G. Thompson, K. T. Tan, C. Marinelli, R. V. Penty, I. H. White, V. M. Ustinov, A. E. Zhukov, Y. M. Shernyakov, and A. R. Kovsh. "35 GHz mode-locking of 1.3  $\mu\text{m}$  quantum dot lasers". In: *Appl. Phys. Lett.* 85.5 (2004), p. 843. doi: 10.1063/1.1776340.
- [75] N. Ledentsov, M. Grundmann, F. Heinrichsdorff, D. Bimberg, V. Ustinov, A. Zhukov, M. Maximov, Z. Alferov, and J. Lott. "Quantum-dot heterostructure lasers". In: *IEEE J. Select. Topics Quantum Electron.* 6.3 (May 2000), pp. 439–451. doi: 10.1109/2944.865099.
- [76] F. Hopfer, A. Mutig, M. Kuntz, G. Fiol, D. Bimberg, N. N. Ledentsov, V. A. Shchukin, S. S. Mikhlin, D. L. Livshits, I. L. Krestnikov, A. R. Kovsh, N. D. Zakharov, and P. Werner. "Single-mode submonolayer quantum-dot vertical-cavity surface-emitting lasers with high modulation bandwidth". In: *Appl. Phys. Lett.* 89.14 (2006), p. 141106. doi: 10.1063/1.2358114.
- [77] X. Huang, A. Stintz, H. Li, L. F. Lester, J. Cheng, and K. J. Malloy. "Passive mode-locking in 1.3  $\mu\text{m}$  two-section InAs quantum dot lasers". In: *Appl. Phys. Lett.* 78.19 (2001), p. 2825. doi: 10.1063/1.1371244.
- [78] J. Campbell, D. Huffaker, H. Deng, and D. Deppe. "Quantum dot resonant cavity photodiode with operation near 1.3 [micro sign]m wavelength". In: *Electron. Lett.* 33.15 (1997), p. 1337. doi: 10.1049/el:19970906.
- [79] L. Chu, A. Zrenner, M. Bichler, and G. Abstreiter. "Quantum-dot infrared photodetector with lateral carrier transport". In: *Appl. Phys. Lett.* 79.14 (2001), p. 2249. doi: 10.1063/1.1408269.
- [80] M. Laemmlin, G. Fiol, C. Meuer, M. Kuntz, F. Hopfer, A. Kovsh, N. Ledentsov, and D. Bimberg. "Distortion-free optical amplification of 20–80 GHz modelocked laser pulses at 1.3 [micro sign]m using quantum dots". In: *Electronics Letters* 42.12 (2006), p. 697. doi: 10.1049/el:20061256.
- [81] A. Lochmann, E. Stock, O. Schulz, F. Hopfer, D. Bimberg, V. Haisler, A. Toropov, A. Bakarov, and A. Kalagin. "Electrically driven single quantum dot polarised single photon emitter". In: *Electronics Letters* 42.13 (2006), p. 774. doi: 10.1049/el:20061076.
- [82] P. Michler, A. Kiraz, C. Becher, W. Schoenfeld, P. M. Petroff, L. Zhang, E. Hu, and A. Imamoglu. "A Quantum Dot Single-Photon Turnstile Device". In: *Science* 290.5500 (Dec. 2000), pp. 2282–2285. doi: 10.1126/science.290.5500.2282.

## Bibliography

- [83] C. Santori, D. Fattal, J. Vučković, G. S. Solomon, and Y. Yamamoto. "Indistinguishable photons from a single-photon device". In: *Nature* 419.6907 (Oct. 2002), pp. 594–597. doi: 10.1038/nature01086.
- [84] E. Stock, T. Warming, I. Ostapenko, S. Rodt, A. Schliwa, J. A. Töflinger, A. Lochmann, A. I. Toropov, S. A. Moshchenko, D. V. Dmitriev, V. A. Haisler, and D. Bimberg. "Single-photon emission from InGaAs quantum dots grown on (111) GaAs". In: *Appl. Phys. Lett.* 96.9 (2010), p. 093112. doi: 10.1063/1.3337097.
- [85] W. Unrau, D. Quandt, J.-H. Schulze, T. Heindel, T. D. Germann, O. Hitzemann, A. Strittmatter, S. Reitzenstein, U. W. Pohl, and D. Bimberg. "Electrically driven single photon source based on a site-controlled quantum dot with self-aligned current injection". In: *Appl. Phys. Lett.* 101.21 (2012), p. 211119. doi: 10.1063/1.4767525.
- [86] S. Tiwari, F. Rana, H. Hanafi, A. Hartstein, E. F. Crabbe, and K. Chan. "A silicon nanocrystals based memory". In: *Appl. Phys. Lett.* 68.10 (1996), p. 1377. doi: 10.1063/1.116085.
- [87] H. Kim, T. Noda, T. Kawazu, and H. Sakaki. "Control of Current Hysteresis Effects in a GaAs/n-AlGaAs Quantum Trap Field Effect Transistor with Embedded InAs Quantum Dots". In: *Jpn. J. Appl. Phys.* 39.Part 1, No. 12B (Dec. 2000), pp. 7100–7102. doi: 10.1143/jjap.39.7100.
- [88] C. Balocco, A. M. Song, and M. Missous. "Room-temperature operations of memory devices based on self-assembled InAs quantum dot structures". In: *Appl. Phys. Lett.* 85 (2004), p. 5911. doi: 10.1063/1.1831558.
- [89] J.-E. Oh and J.-W. Kim. "Room-temperature memory operation of AlGaAs/GaAs high electron mobility transistors with InAs quantum dots embedded in the channel". In: *International Electron Devices Meeting 2000. Technical Digest. IEDM (Cat. No.00CH37138)*. Institute of Electrical & Electronics Engineers (IEEE), 2000, p. 106. doi: 10.1109/iedm.2000.904392.
- [90] K. Koike, K. Saitoh, S. Li, S. Sasa, M. Inoue, and M. Yano. "Room-temperature operation of a memory-effect AlGaAs/GaAs heterojunction field-effect transistor with self-assembled InAs nanodots". In: *Appl. Phys. Lett.* 76 (2000), p. 1464.
- [91] G. Yusa and H. Sakaki. "Trapping of photogenerated carriers by InAs quantum dots and persistent photoconductivity in novel GaAs/n-AlGaAs field-effect transistor structures". In: *Appl. Phys. Lett.* 70.3 (1997), p. 345. doi: 10.1063/1.119068.

- [92] M. Geller, C. Kapteyn, L. Müller-Kirsch, R. Heitz, and D. Bimberg. "Hole storage in GaSb/GaAs quantum dots for memory devices". In: *phys. stat. sol. (b)* 238 (2003), pp. 258–261. doi: 10.1002/pssb.200303023.
- [93] A. Marent, M. Geller, D. Bimberg, A. P. Vasi'ev, E. S. Semenova, A. E. Zhukov, and V. M. Ustinov. "Carrier storage time of milliseconds at room temperature in self-organized quantum dots". In: *Appl. Phys. Lett.* 89.7 (2006), p. 072103. doi: 10.1063/1.2337000.
- [94] G. L. Bir and G. E. Pikus. *Symmetry and Strain-induced Effects in Semiconductors*. John Wiley and Sons, New York, 1974.
- [95] J. H. Van Der Merwe. "Crystal Interfaces. Part II. Finite Overgrowths". In: *Journal of Applied Physics* 34.1 (1963), p. 123. doi: 10.1063/1.1729051.
- [96] V. A. Shchukin and D. Bimberg. "Spontaneous ordering of nanostructures on crystal surfaces". In: *Rev. Mod. Phys.* 71.4 (July 1999), pp. 1125–1171. doi: 10.1103/revmodphys.71.1125.
- [97] F. C. Frank and J. H. van der Merwe. "One-Dimensional Dislocations. I. Static Theory". In: *Proceedings of the Royal Society A: Mathematical, Physical and Engineering Sciences* 198.1053 (Aug. 1949), pp. 205–216. doi: 10.1098/rspa.1949.0095.
- [98] M. Volmer and A. Weber. "Keimbildung in übersättigten Gebilden". In: *Zeitschr. f. phys. Chem.* 119 (1926), p. 277.
- [99] I. N. Stranski and L. Krastanow. "Zur Theorie der orientierten Ausscheidung von Ionenkristallen aufeinander". In: *Monatshefte für Chemie* 71.1 (Dec. 1937), pp. 351–364. doi: 10.1007/bf01798103.
- [100] D. J. Mowbray and M. S. Skolnick. "New physics and devices based on self-assembled semiconductor quantum dots". In: *J. Phys. D: Appl. Phys.* 38.13 (June 2005), pp. 2059–2076. doi: 10.1088/0022-3727/38/13/002.
- [101] L. Müller-Kirsch, R. Heitz, U. W. Pohl, D. Bimberg, I. Häusler, H. Kirmse, and W. Neumann. "Temporal evolution of GaSb/GaAs quantum dot formation". In: *Applied Physics Letters* 79.7 (2001), p. 1027. doi: 10.1063/1.1394715.
- [102] K. Jacobi. "Atomic structure of InAs quantum dots on GaAs". In: *Progress in Surface Science* 71.5-8 (June 2003), pp. 185–215. doi: 10.1016/s0079-6816(03)00007-8.
- [103] J. Márquez, L. Geelhaar, and K. Jacobi. "Atomically resolved structure of InAs quantum dots". In: *Applied Physics Letters* 78.16 (2001), p. 2309. doi: 10.1063/1.1365101.

## Bibliography

- [104] M. Grundmann, O. Stier, and D. Bimberg. "InAs/GaAs pyramidal quantum dots: Strain distribution, optical phonons, and electronic structure". In: *Phys. Rev. B* 52.16 (Oct. 1995), pp. 11969–11981. DOI: 10.1103/physrevb.52.11969.
- [105] O. Stier, M. Grundmann, and D. Bimberg. "Electronic and optical properties of strained quantum dots modeled by 8-band k-p theory". In: *Phys. Rev. B* 59 (1999), p. 5688. DOI: 10.1103/PhysRevB.59.5688.
- [106] A. Schliwa, M. Winkelkemper, and D. Bimberg. "Impact of size, shape, and composition on piezoelectric effects and electronic properties of In(Ga)As/GaAs quantum dots". In: *Phys. Rev. B* 76 (2007), p. 205324. DOI: 10.1103/PhysRevB.76.205324.
- [107] M. Geller, E. Stock, C. Kapteyn, R. L. Sellin, and D. Bimberg. "Tunneling emission from self-organized In(Ga)As/GaAs quantum dots observed via time-resolved capacitance measurements". In: *Phys. Rev. B* 73 (2006), p. 205331. DOI: 10.1103/PhysRevB.73.205331.
- [108] R. J. Warburton, B. T. Miller, C. S. Dürr, C. Bödefeld, K. Karrai, J. P. Kotthaus, G. Medeiros-Ribeiro, P. M. Petroff, and S. Huant. "Coulomb interactions in small charge-tunable quantum dots: A simple model". In: *Physical Review B* 58.24 (Dec. 1998), pp. 16221–16231. DOI: 10.1103/physrevb.58.16221.
- [109] A. Schliwa, M. Winkelkemper, and D. Bimberg. "Few-particle energies versus geometry and composition of  $\text{In}_x\text{Ga}_{1-x}\text{As}/\text{GaAs}$  self-organized quantum dots". In: *Phys. Rev. B* 79.7 (Feb. 2009). DOI: 10.1103/physrevb.79.075443.
- [110] J. Frenkel. "On Pre-Breakdown Phenomena in Insulators and Electronic Semiconductors". In: *Physical Review* 54.8 (Oct. 1938), pp. 647–648. DOI: 10.1103/physrev.54.647.
- [111] P. Blood and J. W. Orton. *The Electrical Characterization of Semiconductors: Majority Carriers and Electron States*. Academic, London, 1992.
- [112] M. Lannoo and J. Bourgoin. "Point Defects in Semiconductors I - Theoretical Aspects". In: *Springer Series in Solid-State Sciences* 22 (1981).
- [113] M. Geller, C. Kapteyn, L. Müller-Kirsch, R. Heitz, and D. Bimberg. "450 meV localization in GaSb/GaAs quantum dots". In: *Appl. Phys. Lett.* 82 (2003), p. 2706. DOI: 10.1063/1.1569413.

- [114] C. Kapteyn, M. Lion, R. Heitz, D. Bimberg, P. Brunkov, B. Volovik, S. Konnikov, A. Kovsh, and V. Ustinov. "Time-Resolved Capacitance Spectroscopy of Hole and Electron Levels in InAs/GaAs Quantum Dots". In: *phys. stat. sol. (b)* 224.1 (Mar. 2001), pp. 57–60. doi: 10.1002/1521-3951(200103)224:1<57::aid-pssb57>3.0.co;2-r.
- [115] S. Schulz, S. Schnüll, C. Heyn, and W. Hansen. "Charge-state dependence of InAs quantum-dot emission energies". In: *Phys. Rev. B* 69 (2004), p. 195317. doi: 10.1103/PhysRevB.69.195317.
- [116] O. Engström, M. Malmkvist, Y. Fu, H. O. Olafsson, and E. O. Sveinbjörnsson. "Thermal emission of electrons from selected s-shell configurations in InAs/GaAs quantum dots". In: *Appl. Phys. Lett.* 83 (2003), p. 3578. doi: 10.1063/1.1622437.
- [117] U. Bockelmann and G. Bastard. "Phonon scattering and energy relaxation in two-, one-, and zero-dimensional electron gases". In: *Phys. Rev. B* 42.14 (Nov. 1990), pp. 8947–8951. doi: 10.1103/physrevb.42.8947.
- [118] R. Ferreira and G. Bastard. "Phonon-assisted capture and intradot Auger relaxation in quantum dots". In: *Appl. Phys. Lett.* 74.19 (1999), p. 2818. doi: 10.1063/1.124024.
- [119] J. Bourgoin and M. Lannoo. "Point Defects in Semiconductors II - Experimental Aspects". In: *Springer Series in Solid-State Sciences* 35 (1983).
- [120] M. Geller. "Investigation of Carrier Dynamics in Self-Organized Quantum Dots for Memory Devices". PhD thesis. Technische Universität Berlin, 2007.
- [121] W. Nolting. *Grundkurs Theoretische Physik 7: Viel-Teilchen-Theorie*. Springer Spektrum, 2009.
- [122] C. Kapteyn. "Carrier Emission and Electronic Properties of Self-Organized Semiconductor Quantum Dots". PhD thesis. Technische Universität Berlin, 2001.
- [123] G. Vincent, A. Chantre, and D. Bois. "Electric field effect on the thermal emission of traps in semiconductor junctions". In: *Journal of Applied Physics* 50.8 (1979), p. 5484. doi: 10.1063/1.326601.
- [124] J. Gelze. "Ladungsträgerdynamik in Quantenpunkt-basierten Speicherbausteinen". MA thesis. TU-Berlin, 2009.

## Bibliography

- [125] T. Nowozin, A. Marent, M. Geller, D. Bimberg, N. Akçay, and N. Öncan. "Temperature and electric field dependence of the carrier emission processes in a quantum dot-based memory structure". In: *Appl. Phys. Lett.* 94 (2009), p. 042108. DOI: 10.1063/1.3076126.
- [126] T. Nowozin, A. Marent, L. Bonato, A. Schliwa, D. Bimberg, E. P. Smakman, J. K. Garleff, P. M. Koenraad, R. J. Young, and M. Hayne. "Linking structural and electronic properties of high-purity self-assembled GaSb/GaAs quantum dots". In: *Phys. Rev. B* 86 (2012), p. 035305. DOI: 10.1103/PhysRevB.86.035305.
- [127] J. Hwang, A. J. Martin, J. M. Millunchick, and J. D. Phillips. "Thermal emission in type-II GaSb/GaAs quantum dots and prospects for intermediate band solar energy conversion". In: *J. Appl. Phys.* 111 (2012), p. 074514. DOI: 10.1063/1.3703467.
- [128] G. Stracke, A. Glacki, T. Nowozin, L. Bonato, S. Rodt, C. Prohl, A. Lenz, H. Eisele, A. Schliwa, A. Strittmatter, U. W. Pohl, and D. Bimberg. "Growth of  $\text{In}_{0.25}\text{Ga}_{0.75}\text{As}$  quantum dots on GaP utilizing a GaAs interlayer". In: *Appl. Phys. Lett.* 101 (2012), p. 223110. DOI: 10.1063/1.4768294.
- [129] O. Madelung, U. Rössler, and M. Schulz. "gallium arsenide (GaAs), hole traps (directly measured cross sections)". In: *Landolt-Börnstein - Group III Condensed Matter*. Vol. 41A2ß. SpringerMaterials, 2016. DOI: 10.1007/10860305\\_98.
- [130] O. Madelung, U. Rössler, and M. Schulz. "gallium phosphide (GaP), energies and capture cross sections of hole traps". In: *Landolt-Börnstein - Group III Condensed Matter*. Vol. 41A2ß. SpringerMaterials, 2016. DOI: 10.1007/10860305\\_52.
- [131] M. Russ, C. Meier, B. Marquardt, A. Lorke, D. Reuter, and A. D. Wieck. "Quantum dot electrons as controllable scattering centers in the vicinity of a two-dimensional electron gas". In: *Phase Transitions* 79.9 (Sept. 2006), pp. 765–770. DOI: 10.1080/01411590600960893.
- [132] M. Russ, C. Meier, A. Lorke, D. Reuter, and A. Wieck. "Role of quantum capacitance in coupled low-dimensional electron systems". In: *Phys. Rev. B* 73.11 (Mar. 2006). DOI: 10.1103/physrevb.73.115334.
- [133] A. Rack, R. Wetzler, A. Wacker, and E. Schöll. "Dynamical bistability in quantum-dot structures: Role of Auger processes". In: *Physical Review B* 66.16 (Oct. 2002). DOI: 10.1103/physrevb.66.165429.
- [134] D. V. Lang. "Deeplevel transient spectroscopy: A new method to characterize traps in semiconductors". In: *J. Appl. Phys.* 45 (1974), p. 3023. DOI: 10.1063/1.1663719.

- [135] D. K. Schroder. *Semiconductor material and device characterization*. John Wiley Sons, Hoboken, New Jersey, 2006.
- [136] G. L. Miller, D. V. Lang, and L. C. Kimerling. "Capacitance Transient Spectroscopy". In: *Annual Review of Materials Science* 7.1 (Aug. 1977), pp. 377–448. DOI: 10.1146/annurev.ms.07.080177.002113.
- [137] H. G. Grimmeiss and C. Ovren. "Fundamentals of junction measurements in the study of deep energy levels in semiconductors". In: *Journal of Physics E: Scientific Instruments* 14.9 (Sept. 1981), pp. 1032–1042. DOI: 10.1088/0022-3735/14/9/002.
- [138] S. Anand, N. Carlsson, M.-E. Pistol, L. Samuelson, and W. Seifert. "Deep level transient spectroscopy of InP quantum dots". In: *Applied Physics Letters* 67.20 (1995), p. 3016. DOI: 10.1063/1.114937.
- [139] S. Anand, N. Carlsson, M.-E. Pistol, L. Samuelson, and W. Seifert. "Electrical characterization of InP/GaInP quantum dots by space charge spectroscopy". In: *Journal of Applied Physics* 84.7 (1998), p. 3747. DOI: 10.1063/1.368553.
- [140] C. Kapteyn, F. Heinrichsdorff, O. Stier, R. Heitz, M. Grundmann, N. Zakharov, D. Bimberg, and P. Werner. "Electron escape from InAs quantum dots". In: *Physical Review B* 60.20 (1999), p. 14265. DOI: 10.1103/PhysRevB.60.14265.
- [141] C. M. A. Kapteyn, M. Lion, R. Heitz, D. Bimberg, P. N. Brunkov, B. V. Volovik, S. G. Konnikov, A. R. Kovsh, and V. M. Ustinov. "Hole and electron emission from InAs quantum dots". In: *Appl. Phys. Lett.* 76.12 (2000), p. 1573. DOI: 10.1063/1.126099.
- [142] C. M. A. Kapteyn, M. Lion, R. Heitz, D. Bimberg, C. Miesner, T. Asperger, K. Brunner, and G. Abstreiter. "Many-particle effects in Ge quantum dots investigated by time-resolved capacitance spectroscopy". In: *Appl. Phys. Lett.* 77.25 (2000), p. 4169. DOI: 10.1063/1.1334651.
- [143] P. Omling, L. Samuelson, and H. G. Grimmeiss. "Deep level transient spectroscopy evaluation of nonexponential transients in semiconductor alloys". In: *Journal of Applied Physics* 54.9 (1983), p. 5117. DOI: 10.1063/1.332733.
- [144] D. S. Day, M. Y. Tsai, B. G. Streetman, and D. V. Lang. "Deep-level-transient spectroscopy: System effects and data analysis". In: *Journal of Applied Physics* 50.8 (1979), p. 5093. DOI: 10.1063/1.326665.
- [145] T. Nowozin, L. Bonato, A. Högner, A. Wiengarten, D. Bimberg, W.-H. Lin, S.-Y. Lin, C. J. Reyner, B. L. Liang, and D. L. Huffaker. "800 meV localization energy in GaSb/GaAs/Al<sub>0.3</sub>Ga<sub>0.7</sub>As quantum dots". In: *Appl. Phys. Lett.* 102 (2013), p. 052115. DOI: 10.1063/1.4791678.

## Bibliography

- [146] G. Stracke, E. M. Sala, S. Selve, T. Niermann, A. Schliwa, A. Strittmatter, and D. Bimberg. "Indirect and direct optical transitions in  $\text{In}_{0.5}\text{Ga}_{0.5}\text{As}/\text{GaP}$  quantum dots". In: *Appl. Phys. Lett.* 104 (2014), p. 123107. doi: 10.1063/1.4870087.
- [147] L. Bonato, E. M. Sala, G. Stracke, T. Nowozin, A. Strittmatter, M. N. Ajour, K. Daqrouq, and D. Bimberg. "230 s room-temperature storage time and 1.14 eV hole localization energy in  $\text{In}_{0.5}\text{Ga}_{0.5}\text{As}$  quantum dots on a GaAs interlayer in GaP with an ALP barrier". In: *Appl. Phys. Lett.* 106.4 (Jan. 2015), p. 042102. doi: 10.1063/1.4906994.
- [148] D. Bimberg, N. Kirstaedter, N. Ledentsov, Z. Alferov, P. Kop'ev, and V. Ustinov. "InGaAs-GaAs quantum-dot lasers". In: *IEEE Journal of Selected Topics in Quantum Electronics* 3.2 (Apr. 1997), pp. 196–205. doi: 10.1109/2944.605656.
- [149] D. L. Huffaker and D. G. Deppe. "Electroluminescence efficiency of 1.3  $\mu\text{m}$  wavelength InGaAs/GaAs quantum dots". In: *Applied Physics Letters* 73.4 (July 1998), pp. 520–522. doi: 10.1063/1.121920.
- [150] L. Pedesseau, J. Even, A. Bondi, W. Guo, S. Richard, H. Folliot, C. Labbe, C. Cornet, O. Dehaese, A. L. Corre, O. Durand, and S. Loualiche. "Theoretical study of highly strained InAs material from first-principles modelling: application to an ideal QD". In: *Journal of Physics D: Applied Physics* 41.16 (July 2008), p. 165505. doi: 10.1088/0022-3727/41/16/165505.
- [151] J. Cahn and R. Hanneman. "(111) Surface tensions of III-V compounds and their relationship to spontaneous bending of thin crystals". In: *Surface Science* 1.4 (Oct. 1964), pp. 387–398. doi: 10.1016/0039-6028(64)90006-8.
- [152] C. Messmer and J. C. Bilello. "The surface energy of Si, GaAs, and GaP". In: *Journal of Applied Physics* 52.7 (July 1981), pp. 4623–4629. doi: 10.1063/1.329342.
- [153] L. Bonato, I. F. Arikan, L. Desplanque, C. Coinon, X. Wallart, Y. Wang, P. Ruterana, and D. Bimberg. "Hole localization energy of 1.18 eV in GaSb quantum dots embedded in GaP". In: *physica status solidi (b)* 10 (Oct. 2016), pp. 1877–1881. doi: 10.1002/pssb.201600274.
- [154] T. Nowozin. "Electronic Properties of and Carrier Dynamics in self-organized Quantum Dots for Memories". PhD thesis. Technische Universität Berlin, 2013.
- [155] S.-H. Wei and A. Zunger. "Calculated natural band offsets of all II-VI and III-V semiconductors: Chemical trends and the role of cation d orbitals". In: *Applied Physics Letters* 72.16 (1998), p. 2011. doi: 10.1063/1.121249.

- [156] T. Nowozin, D. Bimberg, K. Daqrouq, M. N. Ajour, and M. Awedh. "Materials for future quantum dot-based memories". In: *J. Nanomater.* 2013 (2013), p. 215613. DOI: 10.1155/2013/215613.
- [157] S. El Kazzi, L. Desplanque, X. Wallart, Y. Wang, and P. Ruterana. "Interplay between Sb flux and growth temperature during the formation of GaSb islands on GaP". In: *Journal of Applied Physics* 111.12 (2012), p. 123506. DOI: 10.1063/1.4729548.
- [158] D. S. Abramkin, E. A. Emelyanov, M. A. Putyato, A. K. Gutakovskii, A. S. Kozhukhov, B. R. Semyagin, V. V. Preobrazhenskii, and T. S. Shamirzaev. "Formation and crystal structure of GaSb/GaP quantum dots". In: *Bull. Russ. Acad. Sci. Phys.* 80.1 (Jan. 2016), pp. 17–22. DOI: 10.3103/s1062873816010032.
- [159] S. Pennycook and D. Jesson. "High-resolution Z-contrast imaging of crystals". In: *Ultramicroscopy* 37.1-4 (Aug. 1991), pp. 14–38. DOI: 10.1016/0304-3991(91)90004-p.
- [160] Y. Wang and P. Ruterana. "The strain models of misfit dislocations at cubic semiconductors hetero-interfaces". In: *Applied Physics Letters* 103.10 (2013), p. 102105. DOI: 10.1063/1.4820385.
- [161] C. Robert, C. Cornet, P. Turban, T. Nguyen Thanh, M. O. Nestokoln, J. Even, J. M. Jancu, M. Perrin, H. Folliot, T. Rohel, S. Tricot, A. Balocchi, D. Lagarde, X. Marie, N. Bertru, O. Durand, and A. Le Corre. "Electronic, optical, and structural properties (In,Ga)As/GaP quantum dots". In: *Phys. Rev. B* 86 (2012), p. 205316. DOI: 10.1103/PhysRevB.86.205316.
- [162] J. R. Taylor. *An Introduction to Error Analysis*. University Science Books, 1997.



# Acknowledgements

I would like to thank here all those who helped me over the course of my PhD, but I am afraid that the list would be longer than the dissertation itself. I will thank some, and hope that the rest forgive me.

First and foremost I would like to express my sincere gratitude to my advisor Prof. Dieter Bimberg for giving me the opportunity to work in his group and for always believing in the QD-Flash project. I would have never been able to succeed without his academic guidance, unwavering trust, and financial support.

I would also like to thank the other members of my thesis committee: Prof. Thomas Mikolajick for reviewing the dissertation and Prof. Sabine Klapp for heading the committee.

I would not have been able to begin my research without the guidance of my predecessors in the QD-Flash project Dr. Andreas Marent and Dr. Tobias Nowozin. Together with Dr. Paul Geller they patiently answered my questions and helped me structure my work. In particular I thank Tobias for the many years of productive collaboration and for the relaxed work environment.

This dissertation owes much to Kevin Tribowski, whose Bachelor thesis I had the privilege of supervising, and especially to Firat Arikan. I would like to thank Firat for the pleasant atmosphere in the office as well, and wish him the best with the rest of his thesis.

No measurements could have been performed without the samples skilfully grown by Dr. Gernot Stracke, Elisa Sala and Prof. Xavier Wallart. A special thank you goes to Elisa for the close collaboration and much needed coffee breaks.

I am grateful to all my colleagues and members of the group for always being helpful and for keeping the morale high. Among them I would like to mention Jan-Hindrik Schulze, Gunther Larisch, Dr. Luca Sulmoni, Dr. Ricardo Rosales and Prof. André Strittmatter. I am especially grateful to Ricardo for agreeing to proofread my dissertation.

I feel deeply indebted to our secretaries Ulrike Grupe, Doreen Nitzsche and especially Rowsitha Koskinas for their competence in navigating the jungle of bureaucracy and for their seemingly endless patience in the face of my struggle with the German language.

All my friends deserve a huge thank you for supporting me during the past years, but I will limit myself to those who listened to me complain the most: Rafa, Giovanna, Seti, Maria and Javier. I truly do not know where you find the patience.

Finally, I thank my family for being there from the beginning.